**The Dissertation Committee for Edward Wayne Marshall IV certifies that this is the approved version of the following dissertation:**

# Navajo Volcanic Field xenoliths of the Colorado Plateau: a window into subduction processes from the Proterozoic to the present

**Committee:**

Jaime Barnes, Co-supervisor

John Lassiter, Co-supervisor

Douglas Smith

Whitney Behr

Cin-Ty Lee

# Navajo Volcanic Field xenoliths of the Colorado Plateau: a window into subduction processes from the Proterozoic to the present

by

**Edward Wayne Marshall IV**

**Dissertation**

Presented to the Faculty of the Graduate School of
The University of Texas at Austin
in Partial Fulfillment
of the Requirements
for the Degree of

**Doctor of Philosophy**

**The University of Texas at Austin**
**May 2018**

# Dedication

To my family: Edward W. Marshall III, Joanna M. Bassert, and William C. Marshall.

# Acknowledgements

The contents of this dissertation represent not only the hard work of myself, but also of my advisors, Jaime Barnes and John Lassiter. Without their support, guidance, criticism, and efficiency this project would never have taken shape. Jaime was always available for advice and support when I was struggling with writing or interpretations. Even when she was very busy, her door was always open. John pushed me through some of my hardest writing blocks and fiercely challenged me to do my best. His straight shooting advising style made clear the shortcomings of my work. He was able to achieve the near-Sisyphean challenge of teaching someone who hated writing to write. I am so grateful to have you both as my advisors and scientific role models.

Three people were critical in teaching me the skills I needed to collect and evaluate the data in this project. Staci Lowry who taught me everything I know about clean lab techniques. Toti Larson who taught me about the “black box” that is the oxygen line. Finally, Nate Miller who helped me collect my laser ICP-MS data, and was always pleased to use the maximum laser spot size. As I neared the end, there were two talented new lab technicians that gave me a new perspective on techniques I thought I had fully understood. James Maner, who taught me that the UT probe can make data so good I wanted to collect my data all over again. Aaron Satkoski who continues to teach me about the wider world of the clean lab.

I’d like to thank undergraduates who helped me pick cpx because I am too colorblind to tell cpx from opx. Although not a crippling affliction, colorblindness is a handicap that I cannot overcome on my own. I sincerely appreciate your help, Chris Cacciatore, Rebecca deGraffenried, Natalie Raia, and Danny Anderson.

Many of my fellow graduate students (past and present) supported me along the way, both directly and indirectly. I'd like to thank my fellow Barnes group students: Michelle Gevedon, Jeff Cullen, Miguel Cisneros, Evan Ramos, Grace Beaudoin, and my fellow Lassiter group students: Ben Byerly, Rudra Chatterjee, Ruohan Gao, and Leslie Bruce. In addition, I'd like to specifically thank Ben Byerly (again), Kenny Befus, Kim Myers, Peter Carlson, Mackenzie Day, Stephanie Frelinger, Michelle Gevedon (again), Jake Jordan, and Rachel Barnard, for helping with analyses, field work, classes, or just being supportive.

I would also like to thank Doug Smith, who is always excited to talk more about the Colorado Plateau. I really appreciated our conversations that delved into the details of the SUM diatremes. When in town, Dan Schulze was also an excellent source of ideas and knowledge about the diatremes. Hopefully the work in this dissertation will be helpful to both of you in the further study of the SUM diatremes.

My thanks go out to the Jumbo Family at Green Knobs. They very kindly let us collect all the rocks we could carry, when they could have not permitted us access. More broadly, I thank the Navajo Nation for allowing me to collect xenoliths on their land.

# Navajo Volcanic Field xenoliths of the Colorado Plateau: a window into subduction processes from the Proterozoic to the present

Edward Wayne Marshall IV, PhD
The University of Texas at Austin, 2018

Co-Supervisors: John Lassiter and Jaime Barnes

Mantle xenoliths from the central Colorado Plateau record geochemical evidence of both ancient and modern subduction. These xenoliths are sampled from unusual serpentinized ultramafic microbreccia diatremes, and are both modally hydrated and metasomatized. The hydration and metasomatism of the xenoliths is related to Farallon flat-slab subduction beneath the Colorado Plateau. In Chapter 1, Sm-Nd and Re-Os isotopes systematics are used to see through Farallon hydration and metasomatism and learn more about pre-Farallon magmatic events. From Re-Os systematics, the lithospheric mantle beneath the Colorado Plateau has been retained since it formed between 2.0 to 1.6 Ga. Unmetasomatized xenoliths lie on a Sm-Nd isochron that is 1.45 Ga in age, suggesting a major isotopic resetting event at this time. Combining these two observations with those of previous studies suggests that subduction triggered the ~1.4 Ga granite magmatism event in Laurentia. In Chapter 2, oxygen isotope compositions of olivine and hydrogen isotope compositions of hydrous minerals were collected to investigate the sources and effects of Farallon flat-slab fluids on the Colorado Plateau lithospheric mantle. Hydrogen isotope compositions of hydrous minerals are consistent with equilibration with slab-derived fluids. Oxygen isotope compositions of olivines correlate with indices of metasomatism from the same xenoliths. From this correlation,

metasomatism in the lithospheric mantle is related to fluids derived from the serpentinized lithosphere of the Farallon slab. In Chapter 3, hydrogen concentrations in nominally anhydrous minerals (NAMs; e.g. pyroxene) are measured and evaluated for connections between metasomatism, melt extraction, and hydrous mineral growth. There is no convincing clear connection between metasomatism, melt extraction, or hydrous mineral growth and NAM water content either in the Colorado Plateau xenoliths or in studies of NAM water contents from other localities. A key observation is that NAM water content has significantly less variability than similarly incompatible species, such as Ce. This can be explained if water diffuses rapidly through the mantle, smoothing out variability in concentration and decoupling it from indices of melt extraction, metasomatism, or hydrous mineral growth.

# Table of Contents

# List of Tables

# List of Figures

# Chapter 1: Introduction

Unusual diatremes occurring in the Navajo Nation region of the Colorado Plateau have puzzled geologists for over a century. Initially, the Navajo diatremes were characterized as "glacial deposits", an intuitive interpretation of the poorly sorted and rounded appearance of breccia clasts and the moraine-like diatreme outcrops. However, this interpretation was rejected as geologists realized that the central Colorado Plateau was not glaciated and observed that "the deposits" intersected and penetrated the surrounding strata. Instead, the Navajo diatremes were considered igneous in origin and the rounded breccia clasts were thought to have been mobilized from a conglomerate deep below the diatreme or xenoliths somehow rounded by igneous processes (Gregory, 1915). By the 1950's, the Navajo diatremes were identified as "kimberlites" based on the similarity of their green lapilli tuffs with those observed in kimberlites (Allen et al., 1954). However, McGetchin and Silver (1970) observed that these "kimberlites" were entirely different in mineralogy and chemistry. The Navajo diatremes had much lower bulk $K_2O$ and $TiO_2$ than typical kimberlites, reflecting significantly lower abundances of phlogopite and perovskite in the diatremes than is typically found in kimberlites. Instead, these diatremes were rich in fine-grained serpentine that formed the matrix of the "kimberlite" breccia with clasts of widely ranging size and lithology. Additionally, McGetchin and Silver (1970) noticed that there was no glass or melt in the diatreme matrix, therefore calling the matrix "serpentine microbreccia" and later "serpentinized ultramafic microbreccia" (McGetchin and Silver, 1972). They proposed that the Navajo diatremes were fluidized eruptions of granular material driven by a gas or fluid, rather than melt. This emplacement hypothesis and lithology name “serpentinized ultramafic microbreccia” is still in use today.

The early studies of xenoliths within the Navajo diatremes focused primarily on the Navajo diatremes in the northern portion of the volcanic field. However, the xenolith assemblage in northern Navajo diatremes contained far fewer peridotite xenoliths than the southern diatremes. Consequently, these early studies did not describe the peridotite xenolith population in detail (e.g. Watson, 1960; O’Hara and Mercy, 1966).

Smith and Levy (1976) performed the first detailed study of the petrography and petrology of peridotite xenoliths from a Navajo diatreme. The chosen diatreme was Green Knobs, a Navajo diatreme in the southern portion of the volcanic field. This study found that the peridotite xenoliths were variably hydrated, and displayed a wide range of deformation types and severities (ranging between undeformed, cataclastic, and ultramylonitic peridotites). Importantly, the study found that equilibration temperature in a given xenolith strongly depended on the thermometer used, and that equilibrations temperatures extended to very low temperature (<700 °C). This wide range of equilibration temperatures was interpreted to reflect cooling of the lithospheric mantle before eruption. Following Smith and Levy (1976), Smith (1979) detailed the petrography and mineralogy of the hydration assemblage. This study was able to show that the hydration assemblage was a primary mantle assemblage and that growth of the hydration assemblage occurred relatively shortly before xenolith eruption.

The first trace element and isotopic characterizations of peridotites from the Navajo diatremes were performed a decade later by Roden et al. (1990) and Roden and Shimizu (1993). Trace element compositions of clinopyroxene in the peridotites suggested that the peridotites had been melt depleted and variably metasomatized. The Nd-isotopes from the peridotites had radiogenic compositions (εNd ~30), suggesting that the peridotites were derived from ancient lithosphere (likely Proterozoic).

The mounting evidence for Farallon flat slab subduction in the mid and late 1990's dramatically changed the geologic context of the peridotite xenoliths (Humphreys, 1995; Humphreys et al., 2003). Studies concerning the effect of Farallon subduction on the North American subcontinental lithospheric mantle (SCLM) were able to connect some of the oddities of the Navajo diatreme xenoliths with explanations. Thermal modeling of the Farallon flat slab and overlying SCLM revealed that the slab would cool the overlying SCLM (English et al., 2003), explaining the cooling detected by mineral thermometry. The deformation in the peridotite xenoliths, particularly mylonitization, could be explained by intense shearing at the slab-SCLM interface (Behr and Smith, 2016). Fluids from the Farallon flat slab are key in explaining several observations, such as: the formation of garnetites (Smith and Griffin, 2005), the enrichment of fluid-mobile elements in Cordilleran peridotite xenoliths (Alibert, 1994; Lee, 2005), growth of Al-depleted orthopyroxene porphryblasts in some Colorado Plateau xenoliths (Smith and Riter, 1997; Smith et al., 1999), and growth of hydrous minerals abundant in the SUM diatremes' xenoliths (Smith, 1979; Smith, 2010).

This dissertation builds on the observations and interpretations of these earlier studies. This study represents a detailed investigation of the SUM peridotite xenoliths using modern geochemical techniques. The contents of Chapter 2 investigate the Proterozoic history of the Colorado Plateau SCLM recorded by radiogenic isotopes and trace elements that are unaffected by Farallon fluids and metasomatism. Chapter 3 examines oxygen and hydrogen stable isotope compositions in the peridotite xenoliths to better understand the sources and geochemical effects of hydration and metasomatism in the peridotite xenoliths. Lastly, Chapter 4 uses the Colorado Plateau SCLM as an example of SCLM endmember hydration and metasomatism to investigate the relationship among modal hydration, metasomatism, and water content in nominally anhydrous minerals (NAMs). The chapter compares NAM water contents of peridotite xenoliths from the Navajo diatremes with xenoliths from other localities to try to better understand the behavior of water in the mantle.

# Chapter 2: Mantle melt production during the 1.4 Ga Laurentian magmatic event: Isotopic constraints from Colorado Plateau mantle xenoliths[1]

## 2.1 INTRODUCTION

Granites are a major component of Precambrian basement in crustal provinces. In the southwestern U.S., voluminous granite plutons represent the southwestern extreme of a 1.4 Ga magmatic belt extending >4000 km through Greenland into Fennoscandia (e.g., Anderson and Morrison 2005), with 1.4 Ga plutons intruding the Yavapai (2.0–1.8 Ga) and Mazatzal (1.8–1.6 Ga) provinces (Fig. 2.1). These provinces represent the earliest known arc material accreted on the southeastern margin of Laurentia (Bennett and DePaolo, 1987).

Granitic plutons of 1.4 Ga age compose ~35% of exposed Proterozoic bedrock in the southwestern United States (Anderson and Cullers, 1999). The predominance of A-type granites (low Mg# potassic granites enriched in incompatible elements; see Whalen et al. 1987; Anderson and Bender 1989) and few surrounding deformational structures have been used to argue that the 1.4 Ga magmatic event was anorogenic (Anderson and Cullers, 1999). However, Nyman and Karlstrom (1997) identify deformational structures within and surrounding the 1.4 Ga granites suggesting shortening in a NW-SE direction, most easily explained by an orogeny along the NE-SW margin of Laurentia. Recently, structures previously associated with the 1.8–1.6 Ga Mazatzal Orogeny have been re-assessed as belonging to the 1.47–1.3 Ga Picuris Orogeny, further implicating orogeny during the 1.4 Ga magmatic event (Jones et al., 2010; Daniel et al., 2013; Mako et al.,

---

[1] The content of this chapter was published in 2017 in *Geology*: 45, no. 6, 519-522

2015). The dominant models proposed for the 1.4 Ga magmatic event fall into three groups: 1) heating in orogenically thickened crust by radioactive heat buildup or mantle heat conduction (e.g., Goodge and Vervoort, 2006); 2) anorogenic magmatism caused by lithospheric thinning and/or rifting (e.g., Corrigan and Hanmer, 1997, Anderson and Morrison, 2005); and 3) orogenic magmatism accompanied by metamorphism and deformation in a continental arc setting (e.g., Nyman et al., 1994; Nyman and Karlstrom, 1997; Whitmeyer and Karlstrom, 2007).

Proterozoic granite and mantle peridotite are present in the Colorado Plateau (CP) as xenoliths carried by diatremes that intrude the Phanerozoic cover. Previous U-Pb zircon and Sm-Nd mineral geochronology show granite xenoliths from serpentinized ultramafic microbreccia (SUM) diatremes of the Navajo Volcanic Field (NVF) have ages and chemistries matching 1.4 Ga granitoids, suggesting the CP middle and lower crust record evidence of the 1.4 Ga magmatic event (Silver and McGetchin, 1994; Condie et al., 1999; Crowley et al., 2006). We place new constraints on the tectonic regime of the 1.4 Ga magmatic event by focusing on mantle xenoliths. Here we present new Sm-Nd and Re-Os isotope data from NVF peridotite xenoliths that suggest the original Yavapai-Mazatzal SCLM has not been delaminated and was isotopically reset by percolating fluids or melts at 1.4 Ga.

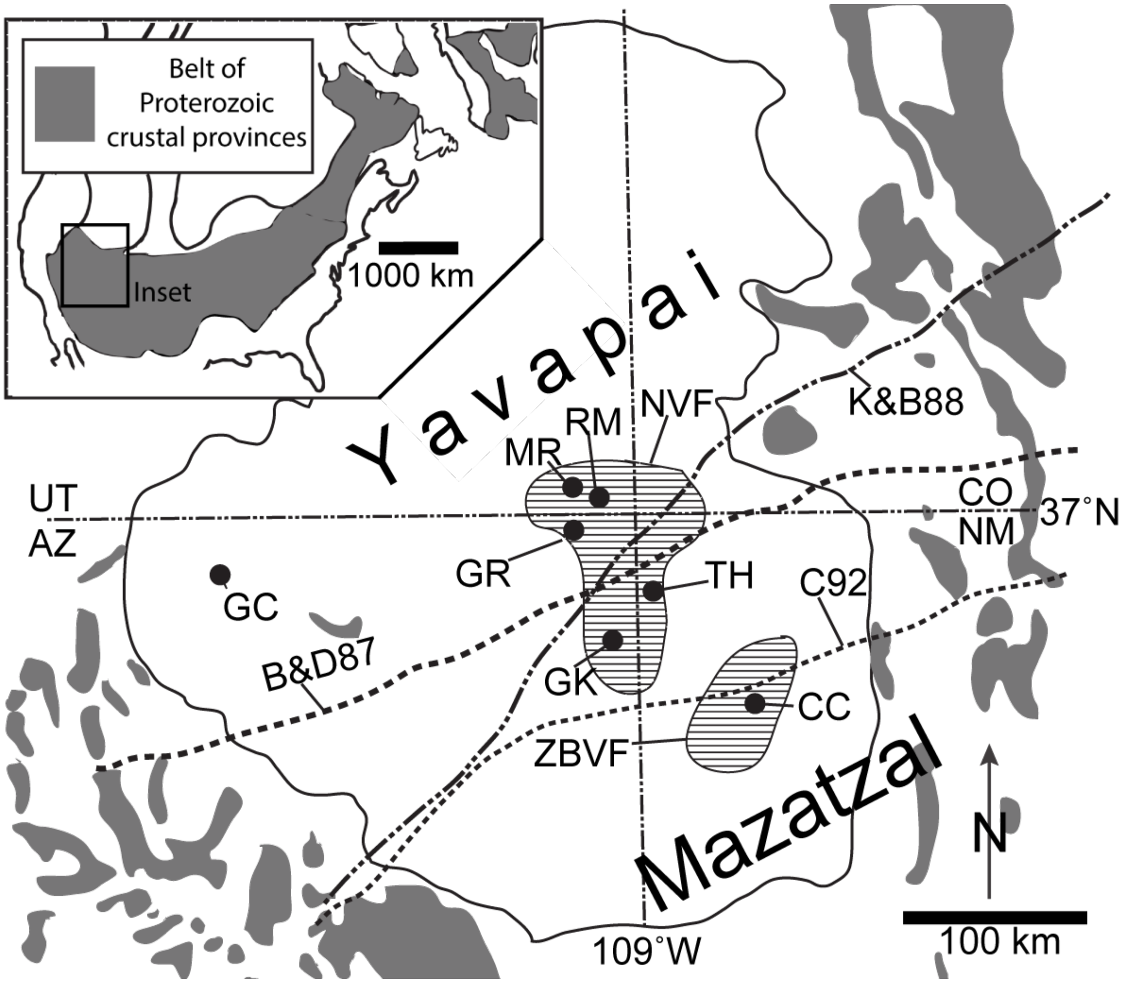

Figure 2.1: Map of the Colorado Plateau (modified from Selverstone er al., 1999), inset map shows the area where Mesoproterozoic plutons occur (modified from Anderson and Morrison, 2005). Shaded gray areas are exposures of Proterozoic rocks; the solid black line encloses the Colorado Plateau. Dashed lines mark different estimates of the Yavapai-Mazatzal boundary: K&B88 (Karlstrom and Bowring, 1988), B&D87 (Bennett and DePaolo, 1987), and C92 (Condie, 1992). Striped areas are pertinent volcanic fields: NVF = Navajo Volcanic Field; ZBVF = Zuni-Bandera Volcanic Field. Black dots are xenolith localities mentioned in the text: GC = Grand Canyon Volcanic Field, MR = Moses Rock, GK = Green Knobs, GR = Garnet Ridge, RM = Red Mesa, TH = Thumb, and CC = Cerro Chato.

## 2.2 SAMPLES AND METHODS

The NVF covers >30,000 km$^2$ and contains ~50 Oligocene-age minettes and SUM diatremes, some of which contain mantle xenoliths (McGetchin and Silver, 1970). These xenoliths are commonly hydrated and metasomatized (Smith, 1979; Smith, 2010; see Appendix 1.2 for sample descriptions). By utilizing isotopic systems that are difficult to disrupt (Re-Os, and to a lesser extent Sm-Nd) we are able to "see through" the geochemical overprint of more recent hydration and metasomatism in order to study Proterozoic events. We selected a suite of peridotites from Green Knobs and Moses Rock diatremes that span the full range of observed cpx major element chemistry in SUM mantle xenoliths (Appendix 1.1). All xenoliths are spinel peridotites with the exception of five samples that either currently contain garnet, or are interpreted to have contained garnet in their pre-hydrated assemblage (see Appendix 1.2). Whole rocks were analyzed for major and trace elements (Appendix 1.3) and Os isotope compositions (Appendix 1.4). Cpx was analyzed for major elements, trace elements (Appendix 1.1) and Nd isotope compositions (Appendix 1.5). See Appendix 1.6 for method details.

## 2.3 RESULTS AND DISCUSSION

### 2.3.1 Sample Grouping

Peridotitic xenoliths from the NVF range from fertile lherzolites to refractory harzburgites ($Al_2O_3$ = 4.45–0.41 wt.%). Fertile lherzolites typically have concave-down, LREE depleted cpx patterns, whereas refractory harzburgites typically have concave-up, LREE enriched cpx patterns. Samples are divided into three groups defined by the slope of the REE pattern around Nd (Fig. A1.7.1). Group D (depleted) samples have depleted

LREE patterns (normalized to primitive mantle of McDonough and Sun, 1995), defined by $(Ce/Nd)_n < 1$ and $(Nd/Sm)_n < 1$, Fig. A1.7.2. Group E (enriched) samples have enriched LREE patterns, defined by $(Ce/Nd)_n > 1$ and $(Nd/Sm)_n > 1$, Fig. A 1.7.4. Group T (transitional) samples have spoon shaped LREE patterns (i.e., transitional between groups D and E) with $(Ce/Nd)_n > 1$ and $(Nd/Sm)_n < 1$, Fig. 1.7.3.

### 2.3.2 $^{187}$Re- $^{187}$Os and $^{147}$Sm- $^{143}$Nd Age Constraints

Previous work on generation of the 1.4 Ga granites proposed that melts might be generated following lithospheric thinning or delamination (Corrigan and Hanmer, 1997). Because lithospheric thinning or delamination replaces old lithosphere with young lithosphere, this process can be tested using the Re-Os system, which is often used to date melt depletion associated with SCLM stabilization (Lee et al., 2001; Rudnick and Walker, 2009). Mantle melting decreases the Re/Os ratio in residual peridotites. Over time, melt-depleted peridotites will evolve less radiogenic $^{187}Os/^{188}Os$ than fertile peridotites, resulting in correlations between indices of melt depletion and $^{187}Os/^{188}Os$. Because peridotites have much higher Os concentrations than most metasomatic agents, the Os isotope system is typically more difficult to overprint than most other radiogenic systems (e.g., Sm-Nd). However, late metasomatic processes can disturb Re/Os ratios and hence correlations between Re/Os and $^{187}Os/^{188}Os$. Two dating methods are often used to circumvent these problems: the rhenium depletion age ($T_{RD}$) and aluminachron age ($T_{Al2O3}$). $T_{RD}$ assumes peridotites evolve with a Re/Os ratio of zero, and calculate the time at which the primitive mantle evolution curve matches the measured peridotite composition (Rudnick and Walker, 2009). Alternatively, one can regress correlations between $^{187}Os/^{188}Os$ and whole rock $Al_2O_3$ in suites of samples to estimate the initial $^{187}Os/^{188}Os$ for highly refractory peridotites, which likely evolve with Re/Os »0 (Reisberg and Lorand, 1995; Handler et al., 1997). This inferred $^{187}Os/^{188}Os$ value is then used to infer a mantle depletion age in the same fashion as $T_{RD}$. Uncertainty in $T_{Rd}$ and $T_{Al2O3}$ ages is primarily due to the assumption that Re/Os = 0, and therefore these model ages are likely younger than the actual melt depletion age.

Measured $^{187}Os/^{188}Os$ values of NVF xenoliths are sub-chondritic, ranging from 0.1140 to 0.1287 (Fig. 2.2; Appendix 1.4). Os isotope ratios correlate with indices of melt depletion such as $Al_2O_3$. Both $T_{Al2O3}$ ages and $T_{RD}$ ages of the three most refractory samples yield Paleoproterozoic ages [$T_{RD}$ = 2.1–1.7 Ga; Figure 2.2; $T_{Al2O3}$ = 2.1–1.7 Ga, for $Al_2O_3$ = 0.0 or 0.7 wt.% (c.f Handler et al., 1997)], consistent with the age of the overlying Yavapai and Mazatzal crust, and similar to ages reported from other CP xenolith localities (e.g., Cerro Chato »1.9 Ga; The Thumb »1.7 Ga) (Lee et al., 2001; Byerly and Lassiter, 2012). The presence of xenoliths with 2.1–1.7 Ga $T_{RD}$ ages suggest that the SCLM stabilized during Yavapai-Mazatzal time and survived up to the time of diatreme eruption. Group D and Group E populations appear to form the fertile and refractory ends of a single aluminachron (Fig. 2.2). It is not clear whether the $Al_2O_3$-$^{187}Os/^{188}Os$ trend represents melt depletion or refertilization. Regardless, this relationship suggests that the Groups D and E xenoliths are genetically related.

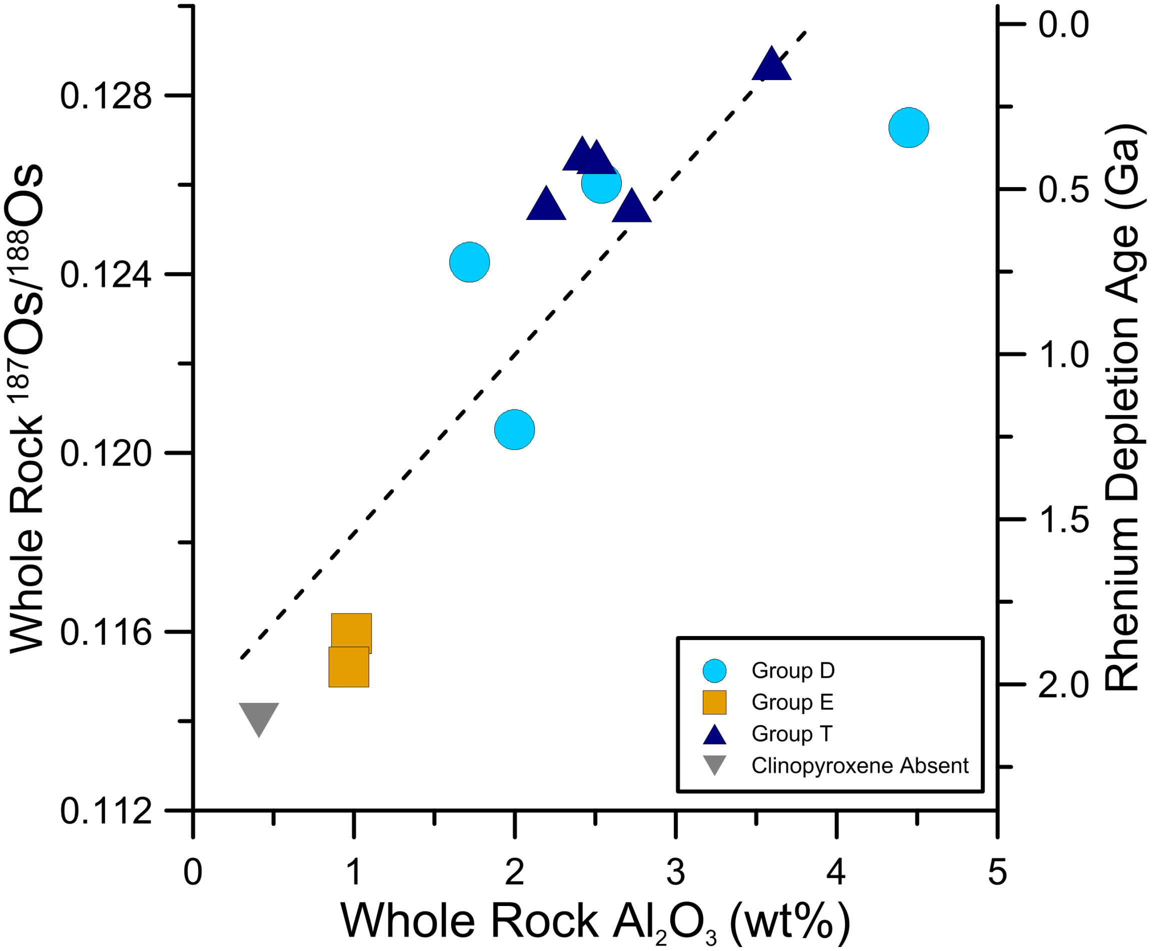

Figure 2.2: Plot of whole rock $Al_2O_3$ vs $^{187}Os/^{188}Os$. Aluminachron regression (dashed line) mentioned in the text. Lithosphere produced in a single melt depletion event should trend along a single aluminachron line. The most $Al_2O_3$-poor sample does not contain cpx, and cannot be categorized into a geochemical group.

The Sm-Nd system is more easily disturbed by metasomatism or melt-rock interaction than the Re-Os system. Green Knobs and Moses Rock peridotites have eNd values ranging from -2.6 to +405. Group E samples have eNd values ranging between -2.6 and 12.4 and have subchondritic Sm/Nd values that do not correlate with Nd-isotopes. The combination of suprachondritic Nd isotopes and subchondritic Sm/Nd in most Group E samples suggests recent (i.e., Phanerozoic) LREE enrichment. Previous studies have suggested Farallon slab-derived melts or fluids metasomatized portions of the southwestern U.S. SCLM during flat slab subduction (Alibert, 1994; Smith et al., 1999; Lee, 2005).

In contrast, the Group D samples display a strong correlation between Sm/Nd and $^{143}$Nd/$^{144}$Nd (Fig. 2.3, $R^2 = 0.9997$, MSWD = 7.1, n = 7) with eNd values ranging from 9.6 to 405. In principle, this correlation could be due to recent metasomatism by the same isotopically enriched melt or fluid that affected the Group E samples. If this were the case we would expect a mixing trend that intersects with the Group E samples. Instead, Group E samples are systematically more radiogenic at a given Sm/Nd than the trend defined by Group D samples. Given this and the LREE-depleted patterns of the Group D samples (which suggests minimal metasomatic overprinting), this Sm-Nd trend most likely represents an isochron.

The slope of the Group D isochron regression yields an age of 1439 ± 55 Ma. The DMM model age (1500 ± 150 Ma) of the isochron y-intercept is consistent with the isochron slope age. Similarity between the DMM extraction age and the slope age supports interpretation of the Group D correlation as an isochron rather than a mixing trend, because there is no a priori requirement for mixing to generate consistent slope and model extraction ages. Melt extraction coupled with melt and/or fluid percolation through the lithosphere at 1.4 Ga could generate depleted REE patterns, similar to melting/percolation processes that produce depleted REE patterns in abyssal peridotites, while simultaneously rehomogenizing Nd-isotopes in the SCLM. The isochron age recorded by the Group D xenoliths is consistent with the range of zircon crystallization ages (1475–1339 Ma) reported for A-type granites associated with the 1.4 Ga magmatic event (Anderson and Bender, 1989; Goodge and Vervoort, 2006). Overlap of the mantle isochron and granite crystallization ages supports models for granite formation that involve contemporaneous melt production in the mantle.

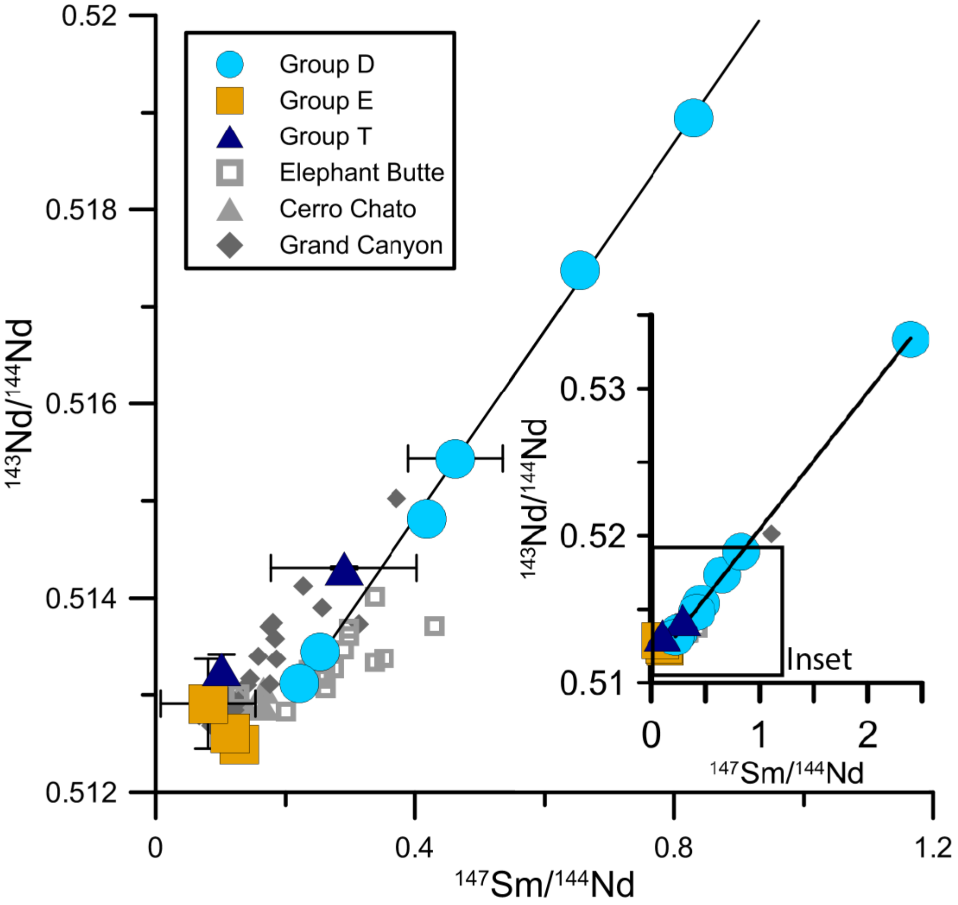

Figure 2.3: Sm-Nd isochron plot of clinopyroxene compositions. The solid regression line is plotted through the Group D clinopyroxenes. The Group E clinopyroxenes plot at lower Sm/Nd compositions than the Group D clinopyroxenes, and do not fall on the Group D regression. Error bars (2s) are calculated from instrument error or sample replication error, whichever was larger. Error bars are smaller than the symbols for most samples. Data from Elephant Butte and Cerro Chato are from (Byerly and Lassiter, 2012), data from the Grand Canyon are from Alibert (1994) and Riter (1999).

### 2.3.3 Tectonic Setting of the 1.4 Ga Magmatic Event

Os-isotopes suggest the original 2.1–1.7 Ga SCLM was at least partially preserved until the eruption of the SUM diatremes at ca. 25 Ma. However, Sm-Nd systematics suggest that the CP SCLM was isotopically reset by percolating fluids or melts at ~1.45 Ga, corresponding to the crystallization age of the A-type granites. These observations place new constraints on tectonic models for the production of granites at ~1.4 Ga.

Anatexis due to radioactive heat buildup in orogenically thickened continental crust (e.g., Goodge and Vervoort, 2006) does not predict concurrent melt or fluid generation or migration in the SCLM. Evidence for mantle resetting at 1.4 Ga therefore is inconsistent with the anorogenic anatexis model because anatexis alone would not generate the mantle melts or fluids necessary for mantle isotopic resetting.

Extension and/or lithospheric mantle thinning have also been proposed for generation of the 1.4 Ga granites (e.g., Anderson and Morrison, 2005; Corrigan and Hanmer, 1997). Thinning or removal of the SCLM would increase heat flow from the mantle, elevating the crustal geotherm and potentially triggering anatexis. Generation of mantle melts could account for the observed Sm-Nd isotope resetting at this time. However, 2.1–1.7 Ga Re-Os ages in the most refractory xenoliths indicate portions of original Yavapai-Mazatzal lithosphere survived the 1.4 Ga event, suggesting the lithosphere was not completely removed at 1.4 Ga, though partial thinning or removal cannot be ruled out. As discussed above, the analyzed xenoliths yield a single whole-rock $Al_2O_3$-$^{187}Os/^{188}Os$ correlation consistent with a single period of SCLM formation. Partial replacement of older SCLM at 1.4 Ga would be expected to produce two distinct Al-Os correlations reflecting different ages of melt depletion. However, this is not observed. Furthermore, recent studies present evidence for a period of compressional deformation and metamorphism beginning at 1490–1450 Ma and extending to ~1440–1350 Ma (Picuris Orogeny; Jones et al., 2010; Daniel et al., 2013; Mako et al., 2015); such results are inconsistent with a rifting model for generation of the 1.4 Ga granites.

Tectonic reconstructions of the Columbia supercontinent at 2.1–1.8 Ga position the Yavapai and Mazatzal crustal provinces of Laurentia at the supercontinent margin (Rogers and Santosh, 2002; Whitmeyer and Karlstrom, 2007; Evans and Mitchell, 2011). Several tectonic models propose subduction along the Laurentian margin during the 1.6–1.3 Ga breakup of Columbia (e.g., Rogers and Santosh, 2002; Zhao et al., 2002; Whitmeyer and Karlstrom, 2007). We propose that the 1.4 Ga Sm-Nd isochron reflects subduction-related melt production and melt/lithosphere interaction. Subduction-derived basaltic melts ponded at the Moho, which heated the lower crust and triggered anatexis (see Anderson and Bender, 1989; Karlstrom et al., 1997; Crowley et al., 2006). This subduction model accounts for the >4,000 km long distribution of ~1.4 Ga granites along the Laurentian margin, supports proposed compressional deformation, explains Nd isotopic resetting in the SCLM, and is consistent with Re-Os mantle extraction ages that suggest preservation of the original Yavapai-Mazatzal SCLM. Unlike in modern subduction environments, calc-alkaline granites are not abundant in the 1.4 Ga magmatic event. Instead, A-type granite magmatism in the southwestern part of the magmatic belt, and Anorthosite-Mangerite-Charnockite-Granite (AMCG) magmatism in the northeastern part of the magmatic belt are typical (Anderson and Morrison, 2005). As suggested in Bybee et al. (2014), AMCG suites may result from subduction of dry slabs, possibly due to elevated Proterozoic geotherms or rapid seafloor spreading resulting in subduction of young, hot and dry oceanic lithosphere.

## 2.4 CONCLUSIONS

Several different tectonic models have been proposed for the generation of the 1.4 Ga magmatic belt that extends from the southwestern U.S. to Fennoscandia. These models make different predictions regarding the role of SCLM in the generation of the 1.4 Ga granites. Refractory mantle xenoliths from the CP record 2.1–1.7 Ga Re-Os mantle extraction model ages, suggesting that the original Yavapai-Mazatzal SCLM remains intact beneath the CP, precluding complete lithosphere removal at 1.4 Ga. However, a subset of weakly-metasomatized CP xenoliths record a 1.45 Ga Sm-Nd isochron, which suggests the SCLM was isotopically reset at this time, most likely in response to mantle melting or melt/fluid migration through the SCLM. Granite production by anatexis due to radiogenic heat buildup in orogenically thickened crust would not generate melts or fluids in the SCLM. This model is therefore inconsistent with evidence for concurrent SCLM isotopic resetting. Similarly, anatexis triggered by SCLM removal or by rifting and resultant increased mantle-crust heat flow is inconsistent with evidence for preservation of the original Yavapai-Mazatzal SCLM.

In contrast, generation of mantle melts in a subduction environment could account for the observed Sm-Nd isotopic resetting at 1.4 Ga and the preservation of the original SCLM. Mantle-derived melts likely ponded at the crustal Moho, triggering lower crustal anatexis and emplacement of the 1.4 Ga granitic belt. Combined with previous suggestions that the Yavapai-Mazatzal crustal provinces themselves likely represent accreted arcs, and that recent subduction of the Farallon slab resulted in hydration and metasomatism of the SCLM beneath southwestern North America, this model further highlights the important role subduction has played in shaping the chemical and physical evolution of North America over the past 2 Ga.

# Chapter 3: The role of serpentinite-derived fluids in metasomatism of the Colorado Plateau (USA) lithospheric mantle[1]

## 3.1 INTRODUCTION

During subduction, dehydration reactions within the down-going slab generate fluids that percolate into the overlying mantle wedge. The oxygen and hydrogen isotope composition of slab-derived fluid differs from ambient mantle and can alter the composition of the mantle wedge. Although numerous studies have used trace element and radiogenic isotope tracers to discern slab signatures in arc magmas and xenoliths (e.g., Leeman et al., 1994; Elliott et al., 1997), fewer studies have examined traditional (O, H) stable isotope variations in arc settings (e.g., Eiler et al., 2000; Eiler et al., 2005). In particular, very few studies have examined coupled stable isotope and trace element data in mantle xenoliths, particularly for subduction-related settings.

Olivine from mantle peridotites worldwide has an average $\delta^{18}O$ value of +5.18 ± 0.14‰ (Mattey et al., 1994). At magmatic temperatures, oxygen isotope fractionation between mantle minerals and silicate melt or magmatic fluids is small. However, the addition of subducted components has the potential to alter the composition of mantle wedge olivine. Chazot et al. (1997) reported limited variations in $\delta^{18}O_{olv}$ values (+5.1 to +5.4‰) in hydrous and anhydrous peridotites, and suggested that subduction minimally affects the oxygen isotope composition of the mantle. In contrast, Perkins et al. (2006) documented $\delta^{18}O_{olv}$ values up to +6.1‰ in metasomatized peridotite xenoliths from the Zuni-Bandera volcanic field, eastern Colorado Plateau (CP). They suggested that oxygen

---

[1] The content of this chapter was published in 2017 in *Geology*: 45, no. 12, 1-4

isotope disequilibria between coexisting mantle phases resulted from recent infiltration of slab-derived fluids or melts. Overall, the stable isotope data set for mantle minerals is limited and few suites have complementary trace element data on the same samples. Here we show that, although the absolute $\delta^{18}O$ variations in mantle peridotites are small, correlations between $\delta^{18}O$ values and other geochemical tracers allow us to constrain the origin and effects of slab-derived fluids in mantle metasomatism. This work has important implications for the identification of subduction signatures in Archean mantle in order to constrain the onset of plate tectonics.

### 3.2 GEOLOGIC BACKGROUND AND PETROLOGY

Beginning at ~80 Ma, subduction of the Farallon plate beneath western North America decreased in subduction angle until the slab flattened out below the sub-continental lithospheric mantle (SCLM). The slab extended eastward from the trench by >700 km (Humphreys et al., 2003), cooling the SCLM and stabilizing hydrous minerals such as serpentine and chlorite (English et al., 2003; Smith, 2010). Slab rollback and removal beneath the CP began at ~30 Ma, exposing the SCLM to warm asthenosphere and potentially triggering the ignimbrite flare-up (Humphreys, 1995; Lee, 2005).

Between 30 and 20 Ma, the CP was host to a series of igneous intrusions, known as the Navajo volcanic field (NVF) (Fig. 3.1). The NVF is a >30,000 $km^2$ volcanic field located in the central portion of the CP and is composed of ~50 minette necks and serpentinized ultramafic microbreccia (SUM) diatremes (Smith, 2010). Here, we present oxygen and hydrogen stable isotope data for peridotite xenoliths from the Green Knobs (n = 27) and Moses Rock (n = 4) diatremes. Major element, trace element, Nd-isotope, and Os-isotope data for these same samples are either reported in Appendix 2.1 and Appendix 2.2 or were previously reported in the appendices of Chapter 1.

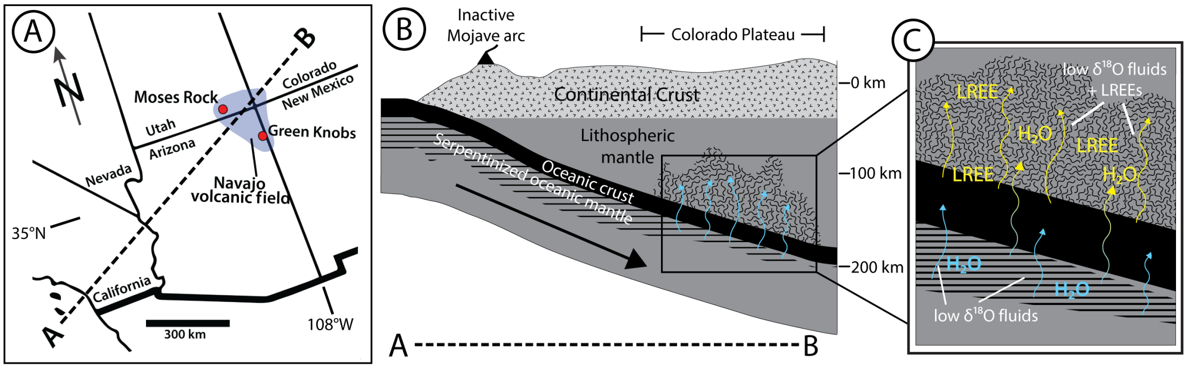

Figure 3.1. Regional map and schematic cartoon of fluid infiltration A) Regional map of the southwestern U.S. showing the cross-section (A to B) of Fig. 3.1B. B) Cross section of the Farallon flat-slab subduction zone during the Eocene based on Humphreys et al. (2003). As the slab exceeds the thermal stability of serpentine, it will begin to dehydrate. The fluids percolate upwards to hydrate and metasomatise the CP SCLM. C) Fluids percolating upwards from the dehydrating serpentinite must pass through the altered oceanic crust of the slab. The fluids exchange with the recycled crust, becoming enriched in LREEs without significant change to their oxygen isotope composition (See text).

Most xenoliths from the SUM diatremes are spinel lherzolites or harzburgites. Two samples (N23-GN and N71-GN) are interpreted to contain chlorite pseudomorphs of garnet (see Roden et al., 1990). In addition to relict anhydrous minerals such as olivine and pyroxene, peridotite assemblages contain up to 65 modal % hydrous minerals (antigorite, chlorite, amphibole, titanoclinohumite; see Appendix 2.3). The hydrous mineral assemblage formed at mantle depths prior to SUM diatreme eruption (e.g. Smith, 2010). For a detailed description of peridotite xenolith textures and petrology, see Behr and Smith (2016) and references therein, and Appendix 1.2.

## 3.3 METHODS

$\delta^{18}O_{olv}$ values were measured via laser fluorination (Sharp, 1990). Each analysis used ~2.0 mg of hand-picked, optically clear olivine grains. Each sample was analyzed one to four times; most were analyzed more than once. Garnet standard UWG-2 ($\delta^{18}O$ = +5.8‰; Valley et al., 1995), olivine standard San Carlos ($\delta^{18}O$ = +5.25‰), and quartz standard Lausanne-1 ($\delta^{18}O$ = +18.1‰) were analyzed. All $\delta^{18}O$ values are reported relative to SMOW, where NBS-28 = +9.65‰. Precision is ± 0.04‰ (1s) based on repeated analysis of the San Carlos standard, or ± 0.05‰ (1s) based on reproducibility of duplicated samples.

δD values of hydrous minerals were determined using the methods of Sharp et al. (2001). Approximately 2 mg of hydrous minerals were loaded into silver capsules, which were pyrolized in a ThermoElectron MAT TC-EA. Analyses of IAEA-C3, IAEA-CH7, and NBS-22 were used to construct a δD calibration curve. Error on each δD analysis is ± 2‰. All δD values are reported relative to SMOW, where NBS-30 δD = –65‰. All stable isotope analyses were completed at the University of Texas at Austin using a ThermoElectron MAT 253 mass spectrometer.

## 3.4 RESULTS

$\delta^{18}O_{olv}$ values range from 5.04‰ to 5.35‰, with an average value of 5.16 ± 0.09‰ (1sd; Figure 3.2a; Appendix 2.4). This range is within error of previously reported average mantle olivine (5.18‰ ± 0.14‰ 1sd; Mattey et al., 1994). For comparison, peridotite xenoliths from a minette neck in the NVF (The Thumb) have $\delta^{18}O_{olv}$ values ranging from 5.05‰ to 5.50‰ (Mattey et al., 1994).

δD values of hydrous minerals range between -79‰ and -33‰ with the majority (64%) of analyses between -55‰ and -40‰ (Fig. 3.2b; Appendix 2.5). These δD values are similar to or higher than estimates of MORB source mantle (-80 ± 5‰; Kyser and O'Neil, 1984), and similar to olivine-hosted melt inclusions in arc basalts (-55‰ to -12‰; Shaw et al., 2008).

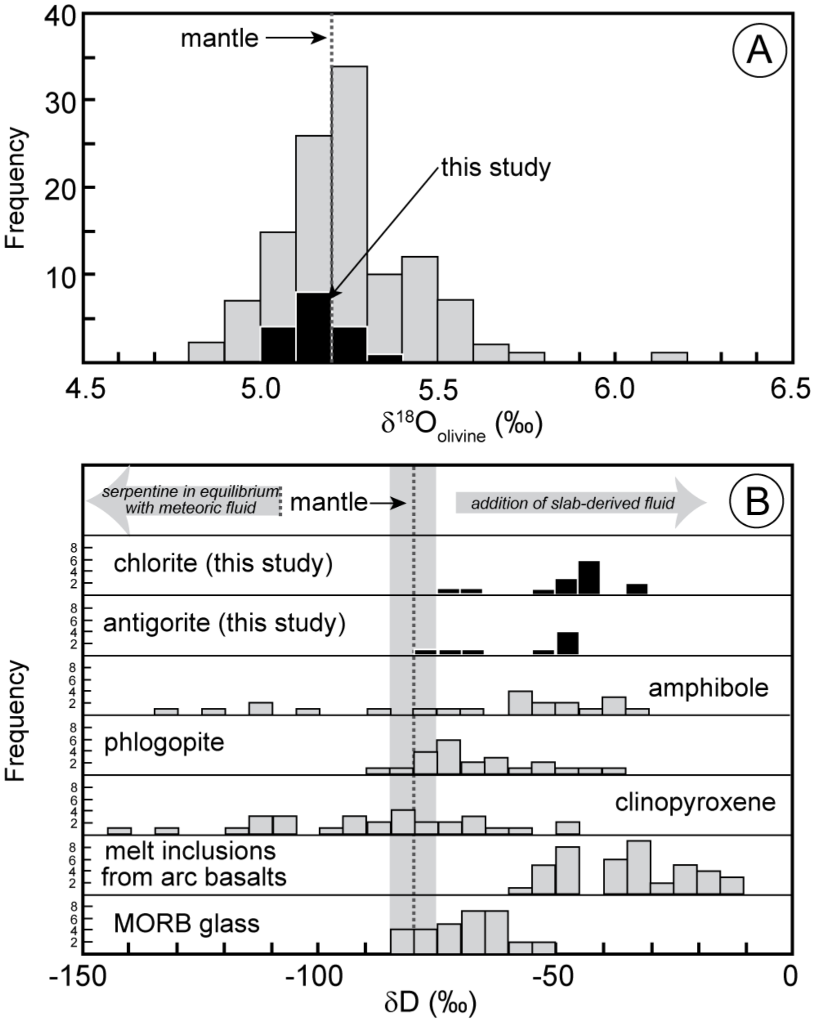

Figure 3.2. A) Histogram of the range of $d^{18}O_{olv}$ values from mantle peridotites; black = analyses from this study, gray = analyses from the literature (Mattey et al., 1994; Chazot et al., 1997; Lowry et al., 1999; Perkins et al., 2006). The dashed line is the average mantle $d^{18}O_{olv}$ value (Mattey et al., 1994). B) Histograms of the range of dD values of hydrous and nominally anhydrous minerals; black = analyses from this publication; gray = analyses from the literature (amphibole and phlogopite data from Kuroda et al., 1975; Boettcher and O'Neil, 1980; Kempton et al., 1988; cpx data from Bell and Ihinger, 2000; Kovács et al., 2016; MORB glass data from Kyser and O'Neil, 1984; arc melt inclusion data from Shaw et al. (2008). Dashed line and gray field = dD value of the mantle and area of uncertainty, respectively (Kyser and O'Neil, 1984).

## 3.5 DISCUSSION

### 3.5.1 Timing of Hydration and Metasomatism

Lherzolitic spinel peridotites from the NVF are depleted in LREE; whereas, harzburgitic peridotites are enriched in LREE (Roden et al., 1990; Marshall et al., 2017). These geochemical trends have been interpreted as reflecting Precambrian melt extraction followed by subsequent metasomatism (e.g., Roden et al., 1990; Alibert, 1994; Marshall et al., 2017). Both the Farallon slab (e.g., Alibert, 1994; Lee, 2005) and Proterozoic oceanic crust have been proposed as possible fluid sources (e.g., Selverstone et al., 1999). In order to place rough timing constraints on the timing of metasomatism, DMM model ages can be used because potential subduction-related metasomatic agents have low Sm/Nd ratios and $^{143}$Nd/$^{144}$Nd less than or equal to the DMM. Recent or future DMM model ages in the most strongly metasomatized NVF xenoliths are consistent with metasomatism during Farallon subduction (Figure A2.6.1). In addition, Farallon metasomatism is also consistent with many <300 Ma DMM ages in metasomatized xenoliths from the Grand Canyon Volcanic Field and Zuni-Bandera Volcanic Field (Alibert, 1994; Byerly and Lassiter, 2015). These model ages suggest that metasomatism of the CP SCLM is at least Phanerozoic, and most likely related to Farallon subduction.

### 3.5.2 Interaction with Slab-Derived Fluids

In the NVF peridotite xenoliths, hydrous minerals formed from reactions between fluids and the anhydrous peridotite. The δD value of a given hydrous mineral is a function of the isotopic composition of the fluid and the temperature-dependent mineral-fluid isotopic fractionation. These xenoliths contain antigorite-bearing assemblages that are only stable above 300 °C (Evans, 2010). Furthermore, magnetite is not found texturally related to antigorite growth. Because magnetite does not form during serpentinization to antigorite above 400 °C (Evans, 2010), hydration temperatures are interpreted be >400 °C (Smith, 2010). The temperature of hydrous mineral growth is therefore constrained between 400 °C and the temperature of antigorite breakdown (~650 °C).

Given measured hydrous mineral δD values from -79‰ to -33‰ and antigorite stability between 400 °C and 650 °C, calculated equilibrium fluid δD values range from -57‰ to -11‰ and -67‰ to -21 ‰, respectively (Saccocia et al., 2009). Either range is similar to the range recorded in Marianas arc melt inclusions (-55‰ to -12‰; Shaw et al., 2008). Shaw et al. (2008) interpreted the high δD values of the Marianas melt inclusions to reflect input of slab-derived fluids into the arc melting region. High δD values (-78 to -39‰) of phlogopite and amphibole in peridotites xenoliths from the Eifel are also interpreted as reflecting input of slab-derived fluids, with an estimated composition of ~-40 to -30‰ (Kempton et al., 1988). The high δD values of the NVF hydrous minerals are inconsistent with equilibration with low-δD meteoric or with non-subduction-related mantle fluids (Fig. 3.2b). Therefore, the hydrous minerals likely formed via reaction with fluids derived from the subducting Farallon slab.

### 3.5.3 Serpentinite-Derived Fluids Drive Metasomatism

Although hydration of the CP SCLM is most likely related to Farallon subduction, the source within the slab remains unclear. Lee (2005) suggested that fluids involved in CP hydration derived from the colder serpentinized core of the Farallon slab.

Alternatively, an eclogite-derived silicate melt component has been proposed (Lee, 2005; Perkins et al., 2006), as well as carbonatitic melt derived from subducted ophicarbonates (Perkins et al., 2006).

Previous work by Marshall et al. (2017) categorized NVF peridotites into three groups (depleted, enriched, and transitional) based on their clinopyroxene (cpx) LREE ratios. $\delta^{18}O_{olv}$ values are correlated with cpx Ce/Sm ratios (Fig. 3.3). This negative correlation suggests that progressive metasomatism lowered the $\delta^{18}O_{olv}$ value of the peridotite as LREEs were enriched. $\delta^{18}O_{olv}$ values do not correlate with either indices of melt depletion or abundance of hydrous minerals (See Fig. A2.6.2, A2.6.3, and A2.6.4).

Fluids derived from the dehydration of low $\delta^{18}O$ and high $\delta D$ serpentinites or lower oceanic crust gabbros could explain the isotopic compositions recorded within the CP SCLM peridotites. Both of these reservoirs have $\delta^{18}O$ values between ~0 and +6‰ due to high temperature hydrothermal exchange with seawater (e.g., Wenner and Taylor, 1973; Gregory and Taylor, 1981). In addition, these sources have higher $\delta D$ values than DMM (~-65 to -35‰; e.g., Alt and Bach, 2006; Wenner and Taylor, 1973).

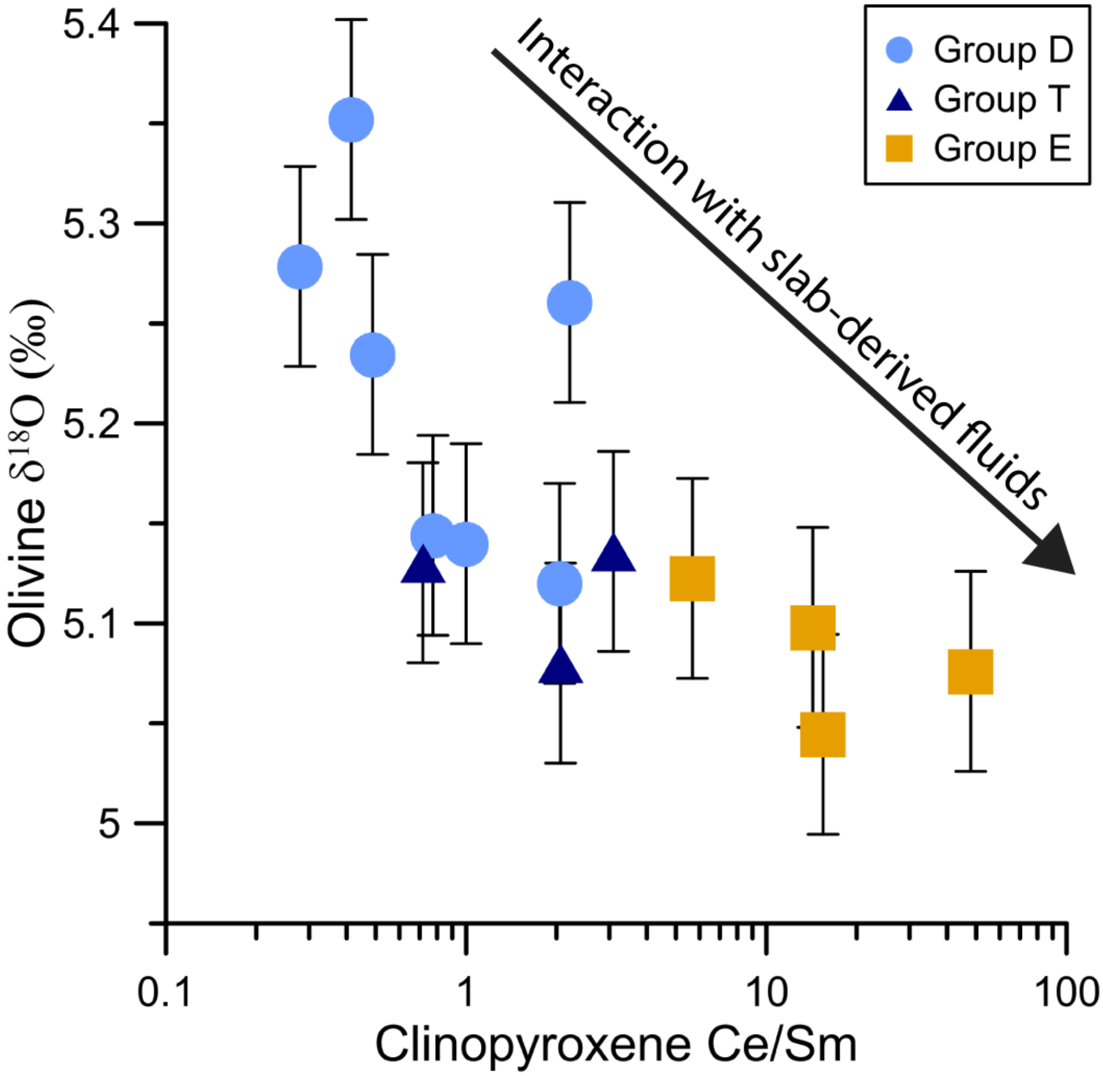

Figure 3.3. Ce/Sm in cpx versus d$^{18}$O$_{olv}$ values. Geochemical groups are based on each sample's REE pattern slope around Nd (see Marshall et al., 2017). Group D (depleted) samples have depleted LREE patterns (normalized to primitive mantle of McDonough and Sun, 1995). Group E (enriched) samples have enriched LREE patterns. Group T (transitional) samples have spoon shaped LREE patterns.

Serpentinites may be a more likely fluid source given their greater carrying capacity for water and stability at depth (e.g., Hacker, 2008). Thermal modeling of Farallon subduction suggests that as the slab was transported eastward, the serpentinite core would have been the last part of the slab to dehydrate (English et al., 2003). Additionally, seismic imaging of the lithosphere-asthenosphere boundary and depth constraints from NVF xenoliths suggest that the Farallon slab would have been at depths >130km beneath the CP (West et al., 2004; Smith, 2013). This is below the depth of the amphibole-out reaction (~100 km; Schmidt and Poli, 1998). Slab gabbros therefore would likely have dehydrated before reaching the CP, leaving serpentinites as the most likely fluid source for metasomatism and hydration.

Although low $\delta^{18}O$ and high $\delta D$ fluids suggest serpentinite dehydration, serpentinites have low concentrations of REE and therefore cannot account for the observed LREE enrichment in many NVF xenoliths. This paradox can be resolved if serpentinite-derived fluids percolated through subducted altered crust, mobilizing LREE, before percolating though the overlying CP lithosphere. Interaction of serpentinite-derived fluid with altered crust would generate an $^{18}O$-depleted, LREE-enriched fluid (similar to Eiler et al., 2005; Lee, 2005). As this fluid percolated through the CP SCLM, it increased the Ce/Sm and lowered the $\delta^{18}O$ of the peridotite, generating the correlation shown in Figure 3.3. The large variation observed in Ce/Sm and relatively small variation in $\delta^{18}O_{olv}$ reflects the greater sensitivity of incompatible trace elements in mantle peridotites to resetting from fluid/rock reaction due to low Ce/O ratios in depleted mantle peridotites.

These results indicate that correlations between $\delta^{18}O$ values and indices of metasomatism or melt depletion may be useful for constraining the effects of subduction on lithospheric mantle. In particular, integration of stable isotope variations with radiogenic isotope constraints on the timing of melt depletion or metasomatic enrichment, particularly in Archaean xenolith suites, may help constrain the role that subduction processes played in initial stabilization and subsequent modification of Earth's oldest cratons, and thus may be fundamental to understanding the rise of modern plate tectonics on Earth.

### 3.6 CONCLUSIONS

Hydrogen and oxygen isotope compositions of minerals within NVF peridotite xenoliths suggest that fluids derived from low-$\delta^{18}O$ serpentinite in the Farallon slab played a central role in both the metasomatism and hydration of the CP lithospheric mantle. Although $\delta^{18}O$ variations in the NVF xenoliths are small, correlations between trace elements and $\delta^{18}O$ values reveal a pattern of subduction-related metasomatic enrichment that affected the oxygen isotope composition of the mantle at the sub per-mil level and allows new constraints on the nature and origin of metasomatic agents. Previous high-precision studies of oxygen isotope variations in mantle peridotite xenoliths have not examined potential correlations with other geochemical tracers. Therefore, the modest $\delta^{18}O$ variations reported in mantle peridotites may contain an overlooked signal of subduction processes over geologic time and may be fundamental to unraveling the history of plate tectonics on Earth.

# Chapter 4: On the (mis)behavior of water in the mantle: controls on nominally anhydrous mineral water contents in mantle peridotites

## 4.1 INTRODUCTION

Mantle water concentration has a fundamental influence on mantle processes. For example, the viscosity of mantle minerals decreases dramatically as water content increases (e.g., Hirth and Kohlstedt, 1996; Mei and Kohlstedt, 2000). Addition of water to subcontinental lithospheric mantle (SCLM) via metasomatism from subduction-related melts or fluids can decrease lithosphere viscosity, which may significantly affect intracontinental deformation, rheology, strain localization, and lowering of the solidus (e.g., Hirth and Kohlstedt, 1996; Humphreys et al., 2003; Dixon et al., 2004; Li et al., 2008; Behr and Smith, 2016). Over geologic time these physical changes and rheologic weakening of the SCLM may result in lithospheric deformation and possibly delamination (Lee et al., 2011; Levander et al., 2011). Delaminated SCLM may be incorporated into the convecting mantle and contribute to the "zoo" of mantle geochemical variability (McKenzie and O'Nions, 1983).

Water in the mantle may be stored either in the structures of hydrous minerals (e.g. amphibole) or as defects within the crystal lattices of nominally anhydrous minerals (NAMs: e.g., olivine, pyroxene). In NAMs, H enters the crystal lattice as protons attached to structural oxygens at atomic point defects (Rossman, 1996). The concentration of the structural H is calculated in its oxide form, as parts per million H2O, and referred to broadly as water content. Water in the mantle is thought to behave as an incompatible species, with similar incompatibility to La and Ce (Michael, 1995);

therefore, mantle minerals are expected to lose water during melting. In contrast, interaction of the lithospheric mantle with water-rich slab-derived fluids and/or melts can result in metasomatism (here defined as cryptic chemical alteration commonly characterized by LREE and LILE enrichment) and/or modal hydration (here defined as the growth of new hydrous mineral phases, such as amphibole, chlorite, and antigorite). Mantle metasomatism and modal hydration result in compositional changes (e.g., increase in La/Sm or in modal hydrous minerals) that are expected to correlate with water enrichment in NAM mantle minerals.

In reality, correlations between mantle NAM water content and indices of either melt extraction or metasomatism are weak or absent in many suites of mantle xenoliths. A few studies have reported correlations between indices of melt depletion and NAM water content in mantle peridotites (e.g., Hao et al., 2014; Warren and Hauri, 2014). For example, NAM water content correlates with whole rock Yb concentrations (an indicator of melt depletion) in variably metasomatized and melt depleted xenoliths from the Chinese Cathaysia block (Hao et al., 2014). Other peridotite xenolith studies note relationships between NAM water content and atypical indices of metasomatism (e.g., Ti in cpx, bulk Na content, Fe3+ in garnet), but not with more emblematic indicators of mantle metasomatism (e.g., La/Sm in cpx, whole rock La/Yb, growth of K-bearing or OH-bearing minerals) (e.g. Peslier et al., 2012; Doucet et al., 2014). In contrast, other studies do not find any correlations between water contents in NAMs and indices of melting or metasomatism (e.g. Xia et al., 2010; Sundvall and Stalder, 2011; Denis et al., 2015). For example, Denis et al. (2015) studied variably melt depleted and metasomatized xenoliths from Massif Central (France) and found no relationships between cpx, opx, or calculated whole rock NAM water content and indices of metasomatism, melt depletion, or modal hydration (some samples contained amphibole). These conflicting observations raise fundamental questions as to the behavior of hydrogen in the mantle and the controls on water content in NAMs. In this study, we examine a set of unique modally hydrated and metasomatized peridotite xenoliths from the Colorado Plateau (CP).

Farallon flat slab subduction beneath the North American Cordillera lasted from ~80 to 25 Ma, releasing fluids and/or melts that hydrated and metasomatized the SCLM (Humphreys et al., 2003). Dixon et al (2004) predicted that Farallon derived fluids should have increased NAM water contents in the CP mantle lithosphere. Previous NAM water content studies of NVF peridotite xenoliths report some of the highest water contents observed in mantle peridotites, with water contents ranging up to 402 ppm in opx and 957 ppm in cpx (the highest ever measured in natural peridotite samples) (Aines and Rossman, 1984; Skogby et al., 1990; Li et al., 2008). Despite the CP, and in particular the NVF, being long recognized as an extreme endmember of mantle hydration and metasomatism, no previous study has examined the relationship between NAM water content, metasomatism, and modal hydration in the NVF xenoliths. The variable modal hydration and metasomatism observed in xenoliths from the NVF provides a natural laboratory to study the co-variance of these two processes and NAM water content in the supra-subduction zone mantle. Here, we show that: (1) correlations between bulk water content and indices of melt extraction are related to changes in cpx modal abundance rather than changes in NAM water content; (2) NAM water content and indices of metasomatism do not display convincing consistent relationships; and (3) rapid diffusion of water in the mantle equilibrates water activity in peridotites with different melt extraction and metasomatic histories, and decouples NAM water content from indices of metasomatism or melt extraction.

## 4.2 GEOLOGICAL SETTING:

The Colorado Plateau (CP) is a physiographic region in the southwestern United States composed of two crustal provinces: the Yavapai province (2.0-1.8 Ga) and the Mazatzal province (1.8-1.6 Ga). These two provinces represent juvenile arcs that were accreted onto the Laurentian margin (Bennett and DePaolo, 1987). Re-Os $t_{RD}$ model ages of peridotite xenoliths from localities within the CP show that the CP SCLM is similar in age to the overlying crust, suggesting simultaneous formation of crust and lithospheric mantle (Lee et al., 2001; Byerly and Lassiter, 2012; Marshall et al., 2017b).

Beginning at ~80 Ma, Farallon plate subduction on the west coast of North America decreased in subduction angle until the slab flattened beneath the SCLM, beginning a period of so called “flat-slab” subduction (Bird, 1988; Humphreys et al., 2003; Humphreys, 2009). This flat slab extended eastward from the west coast by more than 700 km into the interior of North America, resulting in compressional deformation in the Cordilleran crust (Laramide orogeny) and hydration of the CP SCLM. Previous work has documented enrichments in fluid-mobile elements (e.g., Cs, Pb, U, Li, Ba, Rb, Sr), high Sr/Nd ratios, and LREE enrichments in peridotite xenoliths from the southwest United States (e.g., Alibert, 1994; Lee, 2005; Marshall et al., 2017a, Marshall et al., 2017b). In the NVF xenoliths, these trace element enrichments are correlated with depletion in $^{18}O$ resulting from metasomatism by an $^{18}O$-depleted aqueous fluid and/or melt likely derived from the subducting Farallon slab (Marshall et al., 2017a). Slab rollback occurred ~40 Ma exposing the lithospheric mantle to warm asthenosphere, possibly triggering post-Laramide magmatism (Humphreys, 1995; Lee, 2005).

The formation of the NVF (~30 to 20 Ma) in the central CP coincided with the removal of the Farallon slab from beneath the CP SCLM. The NVF is a >30,000 km$^2$ volcanic field located in the central part of the CP composed mostly (~50) of minette necks and a few (~8) unusual diatreme-forming intrusions called serpentinized ultramafic microbreccia (SUM) diatremes (McGetchin and Silver, 1972; Roden, 1981). The two sample localities of this study, Moses Rock and Green Knobs, are two SUM diatremes located in the northern and southern portions of the NVF, respectively (Fig. 2.1).

### 4.3 PETROLOGICAL AND GEOCHEMICAL BACKGROUND:

Peridotite xenoliths from the CP SUM diatremes are dominantly spinel lherzolites and harzburgites, with some uncommon garnet peridotites or peridotites with garnet rims around spinel. Many NVF peridotite xenoliths contain primary hydrous minerals (up to 63% hydrous minerals by mode), which replace the anhydrous peridotitic mineralogy (see Smith and Levy, 1976; Smith, 1979; Smith, 2010; Smith, 2013). Although some garnet remains in samples with garnet rims around spinel, garnet in the garnet peridotites has been fully replaced by chlorite. The prior presence of garnet has been inferred in some samples by identification of chlorite pseudomorphs after garnet and HREE depletion in cpx (Roden et al., 1990). Modal hydration varies widely in mineralogy, texture, and modal abundance likely reflecting differences in P, T, and water availability (Smith, 1979).

This study divides NVF xenoliths into two groups based on thin section observations: anhydrous peridotites and hydrous-mineral-bearing peridotites. Anhydrous peridotites have no perceptible growth of primary hydrous phases. Hydrous-mineral-bearing peridotites have some perceptible amount of primary hydrous mineral growth. In almost all samples, fine-grained serpentine grows along cracks and grain boundaries and is associated with late, low-T serpentinization within the diatreme following eruption (Smith, 1979). This secondary, fine-grained, grain-boundary serpentine is texturally distinct from the primary, grain-penetrating, coarse-grained antigorite that is mantle-derived. Presence or absence of secondary serpentine does not affect peridotite classification.

The SUM diatreme peridotite xenoliths also have variable trace element compositions, ranging from incompatible-depleted lherzolites to incompatible-enriched harzburgites. Chapter 2 categorized peridotite samples into three different groups based on their REE pattern: Group D (Depleted) samples have LREE-depleted patterns ($Ce_n/Nd_n$ <1, $Nd_n/Sm_n$ <1); Group E (Enriched) samples have LREE-enriched patterns ($Ce_n/Nd_n$ >1, $Nd_n/Sm_n$ >1); and Group T (Transitional) samples have spoon shaped patterns ($Ce_n/Nd_n$ >1, $Nd_n/Sm_n$ <1). LREE enrichment in the refractory Group E samples is interpreted to be a product of metasomatism of harzburgites by a LREE-rich, HREE-poor fluid or melt (Roden and Shimizu, 1993). Group E samples have suprachondritic Nd isotope compositions despite subchondritic Sm/Nd ratios, indicating that metasomatism occurred relatively recently, at least within the Phanerozoic (Marshall et al., 2017b). Indices of metasomatism (e.g., La/Sm) also negatively correlate with oxygen isotope compositions in olivine, which suggests that the peridotite suite was metasomatized by an $^{18}$O-depleted fluid sourced from the dehydrating Farallon slab (Marshall et al., 2017a).

For this study, we selected a suite of samples that span the known variability of modal hydration (peridotites of varying hydrous mineral abundance) and metasomatism (D, E, and T groups). Many of the samples have been previously geochemically characterized (Smith, 1979; Roden et al., 1990; Roden and Shimizu, 1993; Smith, 2010; Smith, 2013; Marshall et al., 2017a; Marshall et al., 2017b). The resulting xenolith suite spans the known NVF xenolith range of LREE-enrichment and contains xenoliths with hydrous mineral abundances of up to ~30% by mode (Table 1).

## 4.4 METHODS:

Clinopyroxene major element compositions were determined by electron probe microanalyzer (EPMA), and trace elements were analyzed by laser inductively coupled plasma mass spectrometry (LA-ICP-MS) using an Agilent 7500ce mass spectrometer and coupled New Wave UP193-FX excimer laser. Detailed analytical methods for these analyses can be found in the appendix of Marshall et al. (2017b) or Appendix 1.6. Averaged EPMA analyses of NMNH Cr Augite were within 5% of the accepted standard composition, except for Mn (within 12%) (Jarosewich et al., 1987). EPMA reproducibility was better than 5% for analytes with concentrations greater than 1 wt%, and better than 12% for analytes with concentrations less than 1 wt%. LA-ICP-MS replicate analyses of the BCR-2G secondary standard are reproducible within 5% of the published composition, except for Pb, Hf, Gd, and Y which were reproduced within 8% of the published composition (Strnad et al., 2005).

Clinopyroxene and orthopyroxene hydrogen contents were measured using the Cameca 6f Secondary Ion Mass Spectometer (SIMS) at Arizona State University. The SIMS analytical methods and sample preparation followed the procedures of Aubaud et al. (2007) except that instead of baking the analysis chamber for 24 hours prior to analysis, a Ti-sublimation pump was used overnight prior to analysis to save time and still reach the target ultra-high vacuum of ~$3 \times 10^{-10}$ torr. Each analysis consisted of measuring counts on $^{16}O^{1}H$, $^{18}O$, $^{19}F$, $^{28}Si$, and $^{35}Cl$, and normalizing each mass to $^{28}Si$ to account for signal fluctuation. Standards (62047-70B, CIT17210, PMR-53, JLM77, GRR1017, GRR2334A, JLM50) used to generate calibration curves during data reduction are characterized in Mosenfelder et al. (2011), Mosenfelder and Rossman (2013a), Mosenfelder and Rossman (2013b) and references therein. Additionally, a San Carlos olivine was used as a blank, as it is below the detection limit of many oriented FTIR analyses (< 3ppm; see Appendix Methods). To build calibration curves, 2-3 standards and a blank were loaded into each indium sample mount. Due to limitations in standard availability only PMR-53 and the San Carlos olivine blank could be loaded onto every mount, the other standards were divided between the mounts so that 2-3 standards were in each mount. $^{16}O^{1}H$ background ranged from 10 to 42 ppm. Reproducibility of the $^{16}O^{1}H/^{28}Si$ intensity for the PMR-53 secondary standard was 19.6% (2SD, n=18). The error for PMR-53 represents the maximum expected error, as the different PMR-53 analyses were made on separate analytical sessions, grains of PMR-53, and utilized different calibrating standards. Replicate analyses made sequentially on the same grain show much better reproducibility, within 5% of one another. Expanded SIMS methods can be found in Appendix 3.1.

Because the analyzed samples contained hydrous minerals, special analysis and data filtering procedures were used to ensure only reliable analyses were considered. Prior to every spot analysis, the $^{16}O^{1}H$ ion image was first monitored to detect the presence of cracks, hydrous mineral inclusions, or other defects that could contaminate the analysis. During analysis the analyte intensities were carefully monitored. If a crack or hydrous phase were encountered during analysis this typically resulted in a large (orders of magnitude) spike in $^{16}O^{1}H$ and $^{35}Cl$ and the analysis would be rejected. Sample analyses rejected this way typically measured water contents >10,000 ppm.

Following analysis, the sample analyses were further filtered to ensure that only uncontaminated, representative analyses were included. Only one other SIMS NAM water content study of substantially hydrated peridotites has been attempted (Warren and Hauri, 2014). Strict data filtering was also applied in Warren and Hauri (2014), filtering out 28% of analyses. Here, the filtering approach attempted to remove as few analyses as possible, yet successfully remove analyses that are outliers or have indications of contamination. Because hydrous minerals that form from pyroxene-water reactions (e.g., amphibole, chlorite) can contain high concentrations of Cl relative to NAMs, Cl was used to screen for the presence of these potentially contaminating phases. The distribution of $^{35}Cl/^{28}Si$ in our data set is a strongly skewed population that ranges in $^{35}Cl/^{28}Si$ from $3\times10^{-6}$ to $5\times10^{-3}$, with a median $^{35}Cl/^{28}Si$ of $\sim3\times10^{-5}$. Samples with $^{35}Cl/^{28}Si$ higher than

$1\text{x}10^{-4}$ were removed from the population, removing 12.5% of total analyses (see Fig. A3.2.1).

Finally, sample analyses were then organized into groups by sample and mineral phase. Outliers were screened from within each group. For each mineral phase (opx, cpx) from each sample, outliers were eliminated by removing analyses furthest from the mean until one of three conditions was met: (1) removing any analysis would increase rather than decrease the standard error, (2) only two analyses remained, or (3) the standard error was less than 10% of the average (similar to the 2σ sequential replication error). This filtering method removed less than 5% of analyses, and many samples did not require any filtering. After filtering, the analyses were averaged to represent water contents from each sample and mineral phase. In total, the filtering process removed 17% of all analyses.

### 4.5 RESULTS:

Average water contents in clinopyroxene (cpx) and/or orthopyroxene (opx) from seventeen peridotite xenoliths are presented in Table 4.1. Water contents in cpx and opx range from 38 to 1744 ppm and from 50 to 587 ppm, respectively. As a group, the measured NAM water contents span a wide range similar to full global compilation of NAM water contents (Figs. 4.1 and 4.2), with cpx from two samples extending to extremely high water content. The lowest concentration cpx and opx in this study have concentrations of 48 ppm and 50 ppm, respectively, and are comparable to pyroxenes measured from dry cratonic lithosphere (e.g., North China Craton; Yang et al., 2008). However, the highest cpx and opx water content measured in this study (1744 and 587 ppm, respectively) are the highest so far measured (the previous highest cpx and opx analyses are 957 and 402 ppm respectively, both samples from the Colorado Plateau; Li et al., 2008).

Table 4.1: Clinopyroxene and orthopyroxene water contents

| | Peridotite type | Temperature (C) (BKN°) | Cpx [H2O] ppm (n) | Cpx [H2O] 1sd ppm | Opx [H20] ppm (n) | Opx [H20] 1sd ppm | Cpx Cr# | Cpx Yb ppm | Cpx Ce/Sm | Cpx Ce ppm | Hydrous mineral abundance* |
|---|---|---|---|---|---|---|---|---|---|---|---|
| **EMGN14** | Hydrous-Mineral-Bearing Spinel Peridotite | | | | 297 (5) | 44 | | | | | |
| **EMGN17** | Hydrous-Mineral-Bearing Spinel Peridotite | 627 | 315 (2) | 64 | 67 (1) | | 22.6 | 0.20 | 21.25 | 13.32 | |
| **EMGN19** | Hydrous-Mineral-Bearing Spinel Peridotite | | | | 186 (2) | 83 | | 0.54 | 8.96 | 9.95 | |
| **EMGN2** | Anhydrous Spinel Peridotite | 772 | 581 (5) | 96 | 366 (4) | 51 | 8.4 | 1.49 | 3.10 | 1.47 | |
| **EMGN21** | Hydrous-Mineral-Bearing Spinel Peridotite | | 379 (2) | 42 | | | 15.9 | 0.36 | 48.00 | 4.80 | |
| **EMGN24** | Hydrous-Mineral-Bearing Spinel | 691 | 482 (4) | 52 | 588 (5) | 78 | 11.2 | 0.34 | 2.05 | 2.69 | |
| **EMGN26** | Anhydrous Spinel Peridotite | 856 | 38 (7) | 10 | 50 (3) | 7 | 14.2 | | | | |
| **EMGN29** | Hydrous-Mineral-Bearing Spinel Peridotite | 853 | 1745• (2) | 342• | 438 (5) | 96 | 12.7 | 0.64 | 5.18 | 0.13 | |
| **EMGN7** | Hydrous-Mineral-Bearing Spinel Peridotite | | 297 (5) | 34 | 278 (5) | 35 | 19.0 | 0.29 | 5.67 | 0.08 | |
| **MR-ATG-13** | Anhydrous Spinel Peridotite | 911 | 127 (7) | 7 | 92 (2) | 3 | 12.0 | 1.25 | 0.28 | 0.07 | 0.0 |
| **N106-GN** | Hydrous-Mineral-Bearing Peridotite Garnet rims spinel | | 971• (2) | 1245• | 417 (10) | 96 | 8.7 | 1.33 | 0.49 | 0.33 | 10.8 |
| **N126-GN** | Anhydrous Spinel Peridotite | 872 | 115 (2) | 9 | 122 (2) | 6 | 9.2 | 1.23 | bd | bd | 0.0 |
| **N17-GN** | Hydrous-Mineral-Bearing Spinel Peridotite | 620 | | | 386 (4) | 37 | 12.3 | 0.71 | 2.06 | 0.03 | 4.3 |
| **N178-GN** | Hydrous-Mineral-Bearing Spinel Peridotite | 632 | 260 (2) | 67 | 241 (2) | 53 | 30.2 | 0.44 | 15.56 | 9.36 | 4.2 |
| **N53-GN** | Hydrous-Mineral-Bearing Spinel Peridotite | 1027 | 361 (8) | 74 | 388 (2) | 49 | 9.0 | 1.40 | 0.07 | 0.03 | 1.3 |
| **N55-GN** | Hydrous-Mineral-Bearing Peridotite Garnet rims spinel | | | | 395 (2) | 53 | 12.9 | 0.36 | 15.46 | 2.02 | 4.5 |
| **N61-GN** | Anhydrous Spinel Peridotite | 712 | 301 (4) | 25 | 327 (3) | 34 | 9.0 | 1.00 | 1.00 | 1.30 | 0.0 |

Mineral water contents are averages of several filtered analyses. The number of analyses (n) in each average in in parentheses next to the water content.

*: Point count data of D. Smith (personal communication) •: The cpx water content of these samples are listed here, but not used in plots or discussion. See Methods.

bd: below detection limit

°: Two-pyroxene thermometer of Brey and Kohler (1990)

Two samples contain cpx with very high water contents, EMGN29 and N106-GN. During SIMS measurement of cpx from NVF xenoliths, occasional analyses >1000 ppm H2O with low $^{35}Cl/^{28}Si$ do occur in some samples and usually represent an outlier analysis for that sample. These analyses are typically filtered out by the $^{35}Cl/^{28}Si$ limit or standard error filtering method described in the methods. However, samples EMGN29 and N106 contained enough >1000 ppm H2O analyses with low $^{35}Cl/^{28}Si$ that these analyses could not be sensibly filtered out. These cpx analyses are highly unusual, and additional analyses are needed to better characterize these unique samples. Because of the large uncertainty associated with N106-GN (970 ppm ± 1245 ppm), and the very high water content of EMGN29 (1744 ppm) based on a relatively small number of analyses (n = 2), both of these samples are not included in figures or in the discussion. Excluding these two samples, the water contents of measured cpx range from 38 to 581 ppm.

Orthopyroxene and clinopyroxene water contents correlate along a ~1.3:1 linear relationship (cpx:opx; Fig. 4.3). Previously analyzed CP xenoliths sampled from the Grand Canyon volcanic field also fall along a ~1.3:1 line (Li et al., 2008). However, this linear relationship is dissimilar to regressions of globally compiled cpx and opx NAM water contents, which find cpx:opx ratios close to ~2.1:1 (Demouchy and Bolfan-Casanova, 2016).

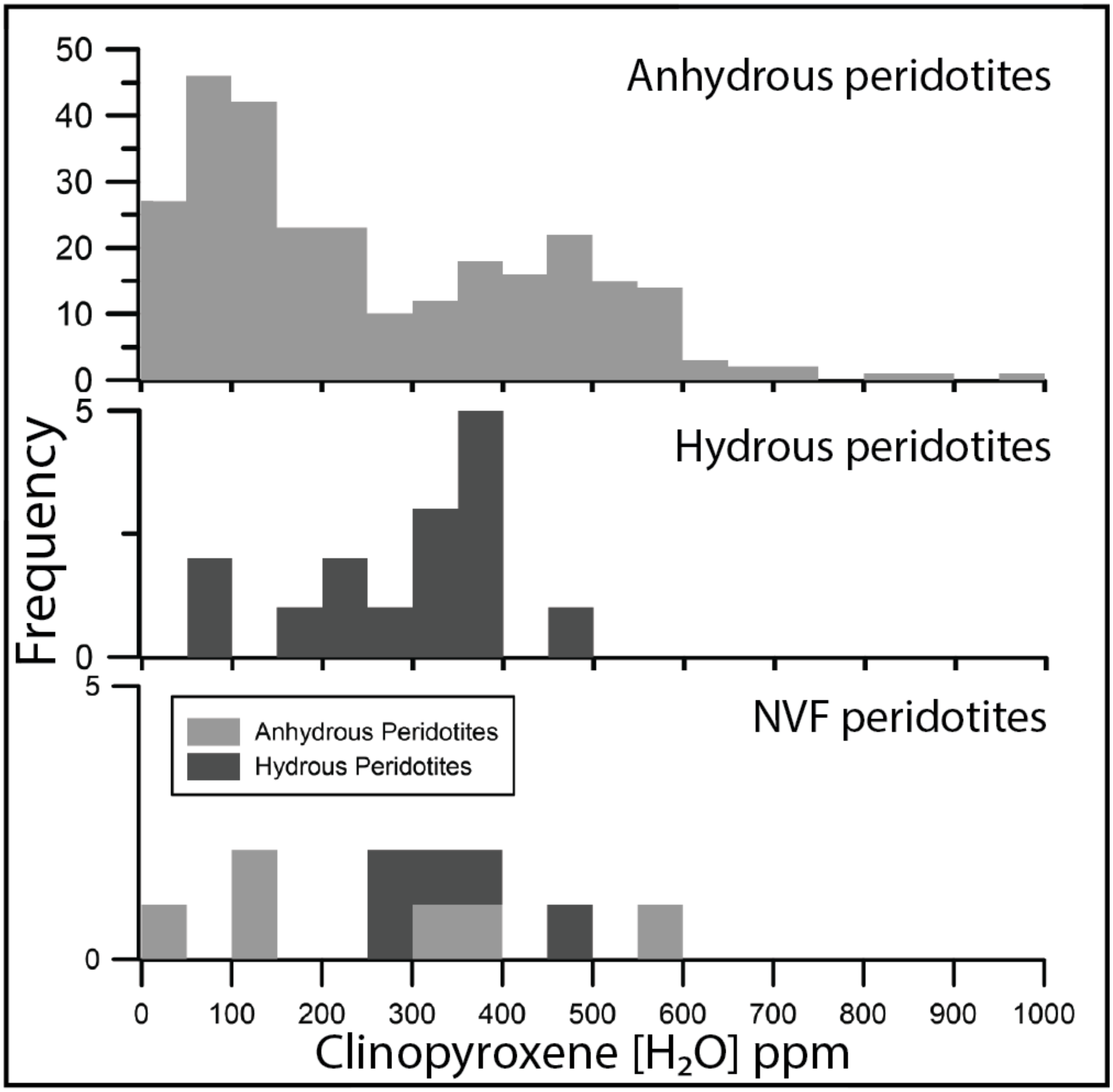

Fig. 4.1: Histograms of clinopyroxene water content sorted into anhydrous samples and hydrous mineral bearing samples, and those from the Navajo Volcanic Field (NVF) peridotites. NVF peridotite histogram is a stacked histogram with hydrous samples on top of anhydrous samples. Data from literature compilations of Peslier (2010) and Demouchy and Bolfan-Casanova (2016). Water contents of NVF peridotites have considerable overlap with both hydrous and anhydrous xenolith compilations. This suggests that clinopyroxene water content in hydrated and metasomatized SCLM is not necessarily higher than clinopyroxene water content in anhydrous, depleted SCLM.

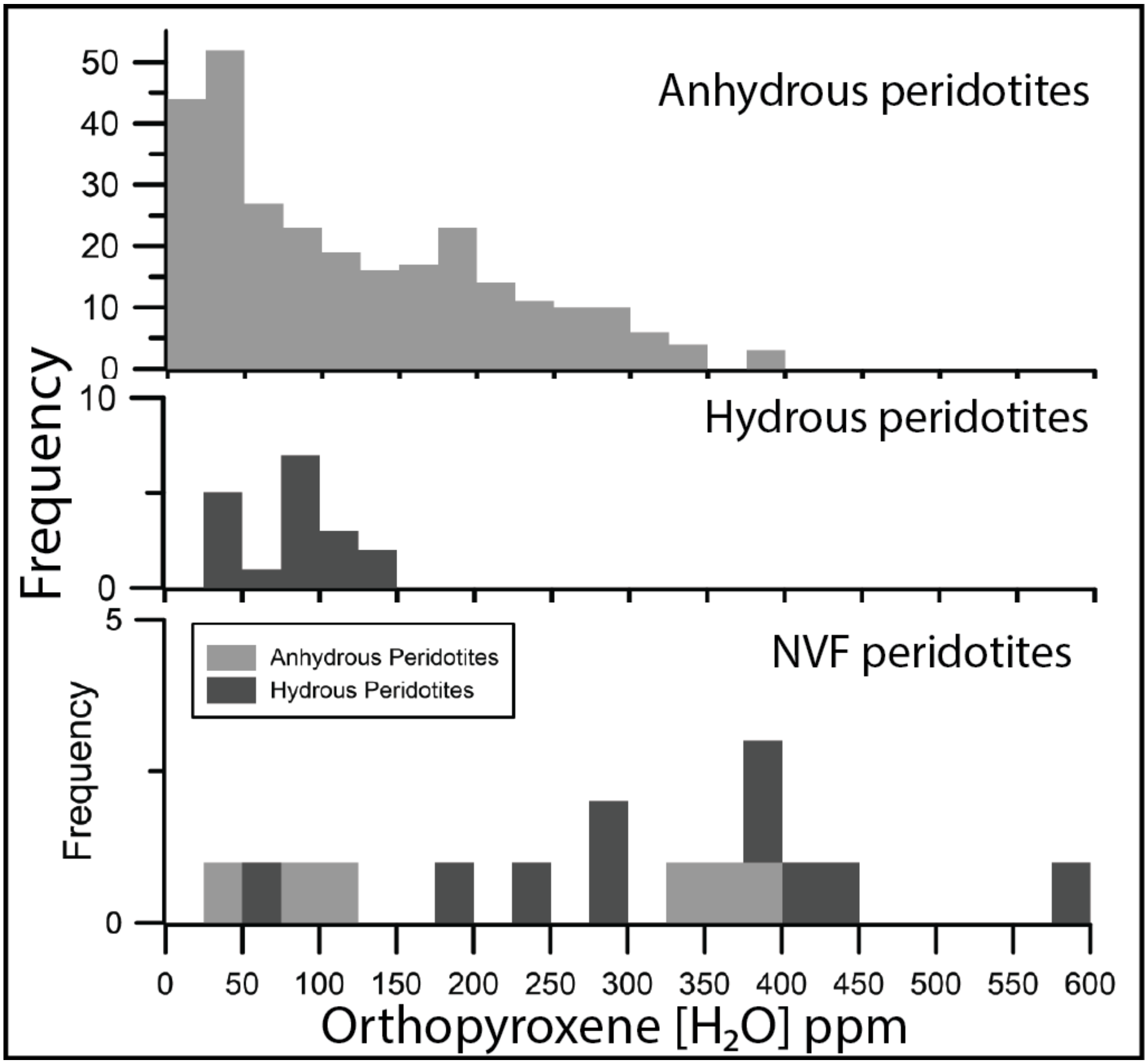

Fig. 4.2: Histograms of orthopyroxene water content sorted into anhydrous samples and hydrous mineral bearing samples, and those from the Navajo Volcanic Field (NVF). NVF peridotite histogram is a stacked histogram with hydrous samples on top of anhydrous samples. Data from literature compilations of Peslier (2010) and Demouchy and Bolfan-Casanova (2016). NVF orthopyroxenes contain some of the highest water contents measured globally. This may be related to water enrichment from metasomatic or hydration processes. However, NVF orthopyroxene contains a wide range of compositions, some as low as orthopyroxene from very dry cratonic SCLM.

## 4.6 DISCUSSION:

Mantle viscosity is strongly dependent on the concentration of water within NAMs. Therefore, NAM water content is important for understanding phenomena that are controlled by mantle viscosity such as SCLM stability and mantle convection. Water behaves as an incompatible species, and therefore should be depleted during partial melting and enriched during metasomatism (Dixon et al., 2004). However, correlations between indices of partial melting or metasomatism and NAM water content are often poor or not present in many xenolith suites. Often these correlations are supported by only a few samples or are weak (e.g., Peslier et al., 2012; Denis et al., 2015). Some correlations display behavior that is inconsistent with experimental partitioning constraints. For example, correlations between bulk peridotite water content and indices of melt depletion, where present, suggest bulk partition coefficients an order of magnitude greater than experimentally measured (Hao et al., 2014; Warren and Hauri, 2014). We analyzed xenoliths from the NVF that have been variably metasomatized and modally hydrated during Farallon flat slab subduction. Previous studies have suggested the western Cordilleran lithosphere should be enriched in water due to Farallon slab dehydration (Dixon et al., 2004). However, measured NAM water contents from NVF xenoliths largely overlap the global distribution of NAM water content (Figs. 4.1 and 4.2). In the following discussion we reexamine the influence of melt depletion, metasomatism, and modal hydration on NAM water contents in the NVF peridotites and in other previously examined suites of mantle xenoliths.

### 4.6.1 Effect of diffusion on water content in NAMs during emplacement:

Nominally anhydrous minerals in mantle xenoliths and basalt-hosted xenocrysts often have water-depleted rims as a result of diffusive water loss during ascent (Demouchy et al., 2006; Peslier and Luhr, 2006; Li et al., 2008; Peslier et al., 2008). Olivine is more likely to have water depleted rims than pyroxene, and previous studies have proposed that pyroxene is more likely to retain its primary water content than olivine (Grant et al., 2007; Sundvall and Stalder, 2011; Warren and Hauri, 2014). This study therefore, focuses on water contents in pyroxenes rather than olivines.

However, pyroxenes may still experience diffusive loss during ascent and emplacement. Ideally, core-rim measurements of intact pyroxene grains would best test for diffusive water loss in grain rims. Unfortunately, the NVF samples are modally hydrated and serpentine veins have fractured intact grains. Grains measured in this study represent random grain fragments, rather than grain portions where the core-rim context is known. The water content reproducibility in different cpx or opx from the same sample is an estimate of inter- and intra-grain homogeneity. Water content analyses from a mixture of cores and rims in a sample that has experienced diffusion will display significant variability. However, this is not observed in most samples. 90% of pyroxenes have internal reproducibilties similar to, or better than, the PMR-53 secondary standard. In addition, if significant water loss had occurred in the pyroxenes, this would disturb the correlation between cpx and opx water content (Fig. 4.3). Because hydrogen diffusion in opx is faster than in cpx (Tian et al., 2017), diffusion in pyroxenes would variably increase the measured cpx/opx water content ratio and therefore disrupt a cpx-opx water content correlation. The NVF cpx-opx data in Fig. 4.3 are relatively well correlated, suggesting that there has not been significant diffusive loss. Taken together, these observations suggest that the pyroxenes have not detectibly experienced diffusive water loss.

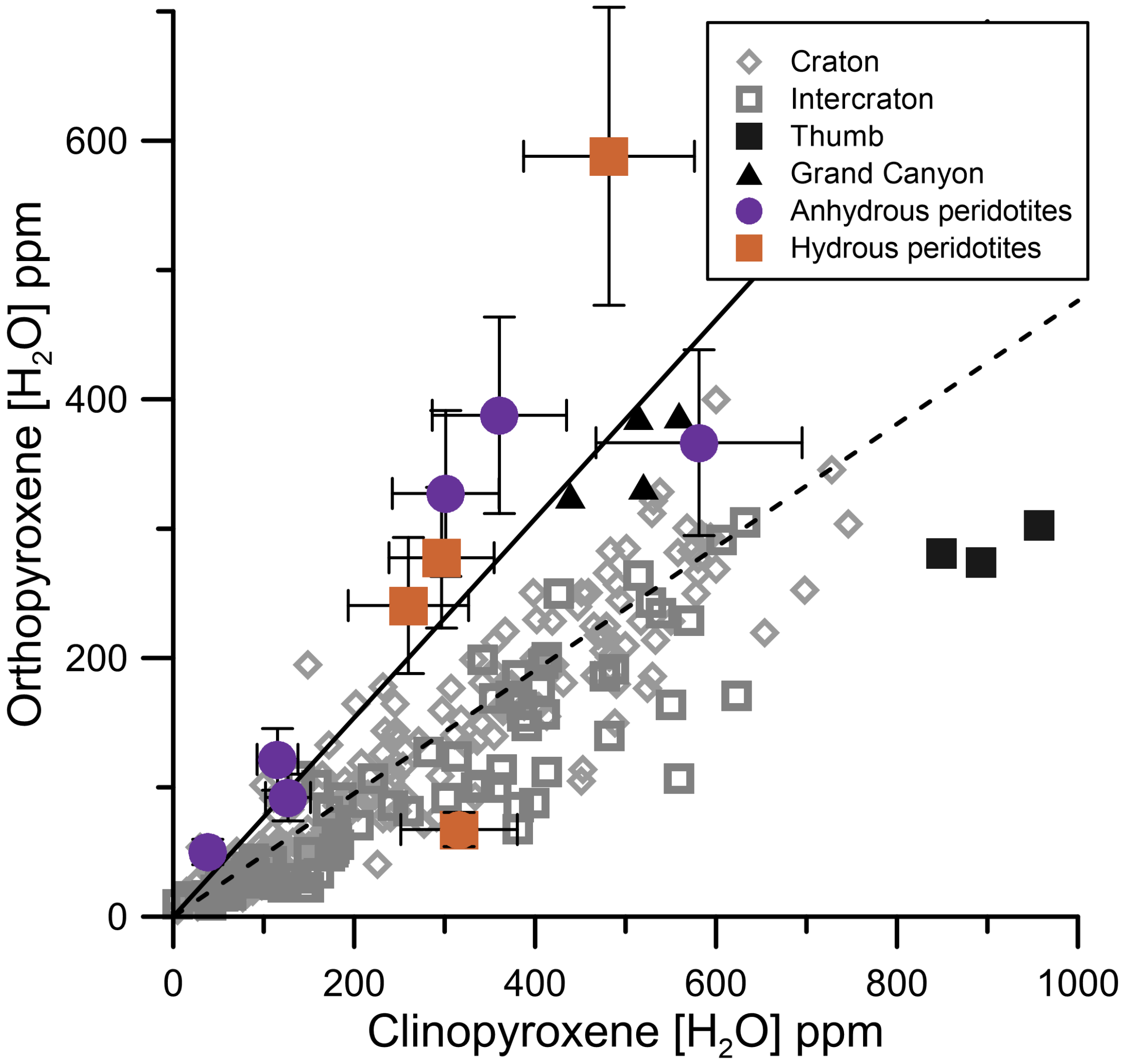

Fig. 4.3: Plot of clinopyroxene water content versus orthopyroxene water content. Note that NVF samples plot along a cpx:opx ratio line of 1.3:1 (solid black line), similar to experimentally derived partition coefficients, rather than a 2.1:1 ratio (dashed black line) that represents an origin-forced regression of compiled NAM water contents from cratonal and intracratonal xenoliths from Peslier (2010) and Demouchy and Bolfan-Casanova (2016). Colorado Plateau xenolith samples from the Thumb and Grand Canyon are from Li et al. (2008). Error bars indicate either the error of sample reproducibility or the error of PMR-53 replicate analyses (19.6%), whichever is larger.

### 4.6.2 Influence of melt depletion on NAM water content:

Water behaves as an incompatible species and is extracted from peridotite residue during melting (Michael, 1995; Tenner et al., 2009). Because water reduces olivine strength and thus mantle viscosity, water removal through mantle melting is expected to increase mantle rigidity. This increase in rigidity may help to explain the stability of SCLM over geologic time (Lee et al., 2011). Previous studies have identified correlations between indices of melt extraction and calculated whole rock water content in two suites of mantle peridotites from the Cathaysia block in China (Hao et al., 2014) and in unveined abyssal peridotites (Fig. 4.4a) (Warren and Hauri, 2014). However, melting models based on experimentally derived mineral/melt partition coefficients predict greater water depletion than observed. Two hypotheses to explain this apparent mismatch are that water may be less incompatible during melt extraction than predicted from partitioning experiments or that water may be replenished in NAMs following melting.

In detail, these previously observed correlations between indices of melt extraction and calculated bulk water content are better explained by variations in cpx modal abundance rather than NAM water content. Because cpx has the highest water content among NAMs, removing cpx from a peridotite decreases its bulk water content. Cpx is removed from peridotites during melt extraction. Therefore, regardless of changes in NAM water content, bulk peridotite water content is expected to correlate with indices of melt extraction. In Cathaysia block xenoliths, cpx modal abundance correlates with bulk water content ($R^2$=0.76) better than other indices of melt extraction such as spinel Cr# ($R^2$= 0.60) or cpx Yb ($R^2$=0.52) (Hao et al., 2014). Melt extraction should reduce the water content of both NAMs and bulk peridotite. However, cpx water contents in both the Cathaysia block xenoliths and unveined abyssal peridotites have weaker correlations with indices of melt extraction than bulk water content (Fig. 4.4b) (Hao et al., 2014; Warren and Hauri, 2014). Furthermore, metasomatism should disturb any initial correlation between indices of melt extraction and bulk water content. Instead, metasomatized xenoliths from the Cathaysia block fall along the same trend as unmetasomatised xenoliths. Therefore, the previously observed correlations between bulk water content and indices of melt extraction are more likely related to variations in the modal compositions of these peridotites rather than melt extraction per se.

Bulk water contents in NVF peridotites correlate with indices of melt depletion, but this correlation is not expected (Fig. 4.4). Several events have geochemically overprinted the CPLM following melt depletion at 2.0 to 1.6 Ga, including a major magmatic event at 1.4 Ga that reset the Nd isotope system, and aqueous metasomatism and modal hydration during Farallon subduction (80 Ma to 25 Ma) (Marshall et al., 2017a; Marshall et al., 2017b). These episodes should have overprinted any previous relationship between melt depletion and water content. Water contents of NAMs or bulk peridotite are not expected to correlate with indices of melt extraction. Therefore, the correlation between bulk peridotite water content and cpx modal abundance in the NVF illustrates that modal composition, rather than melt depletion, controls bulk water content.

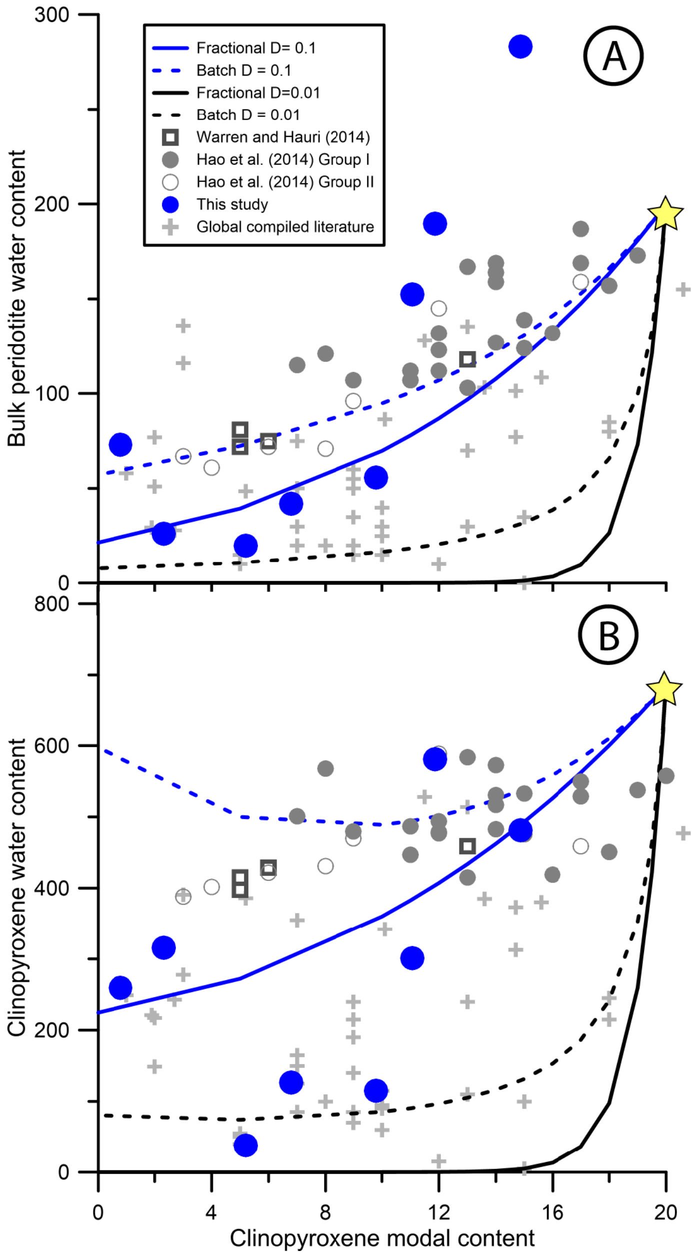

Figure 4.4: Clinopyroxene modal content versus bulk peridotite water content (a) and clinopyroxene water content (b). Yellow star represents starting composition of 18 mode% cpx, 200 ppm bulk water content. Water content partition coefficents used for the melting model are Cpx/opx = 2.3, olivine/cpx = 0.025. Global compilation from the database in Peslier (2010). Hao et al. (2014) Group I xenoliths are LREE-depleted and Group II xenoliths are LREE-enriched.

Melt depletion models predict greater water depletion in residual peridotites than is observed (Fig. 4.4). Either the experimentally determined bulk partition coefficient for water is too low by approximately an order of magnitude, or peridotites have been enriched in water following melt extraction. The measured partitioning behavior of water in MORB appears similar to Ce (Michael, 1995). This natural water partitioning behavior (i.e., Ce-like partitioning) agrees with experimentally determined crystal-melt partition coefficients (Tenner et al., 2009; O'Leary et al., 2010). Therefore, there is reasonably good agreement between natural and experimental mineral-melt partition coefficients for water and no reason to suspect these data. Instead, the peridotites have likely been enriched in water following melt extraction. Regardless, although indices of melt extraction may correlate with bulk water content, NAM water content is not clearly controlled by melt depletion. Recall that viscosity of mantle peridotite is a function of NAM water content, in particular olivine water content. Therefore, the trends observed between bulk water content and indices of melt depletion have no effect on mantle viscosity. Although we do not dispute that melt extraction should deplete peridotites of water, this relationship has yet to be observed in nature.

### 4.6.3 Influence of metasomatism on NAM water content

Metasomatism enriches peridotites in incompatible species and should therefore enrich water as well. This enrichment could explain why peridotites appear to have higher water contents than predicted by melt depletion models. Previous studies have identified correlations between indices of metasomatism and NAM water content. A study of garnet peridotite xenoliths from Liqhobong, Lesotho showed correlations between cpx and garnet Ca, Na and Fe3+ content and cpx water content (Peslier et al., 2012). Another study of garnet peridotite xenoliths from Udachnaya, Russia found correlations between whole rock Fe, Ti, and modal cpx and garnet abundance with garnet water content (Doucet et al., 2014). The correlations in both studies were interpreted to be a result of metasomatism.

However, the relationships between metasomatism and NAM water content are not as clear in detail. Although garnet water content correlates with indices of metasomatism in the Udachnaya xenoliths, orthopyroxene water contents (which are much higher than for garnet) do not. Similarly, the Liqhobong xenoliths display correlations between cpx water content and indices of metasomatism, but not between opx water content and indices of metasomatism (olivine not analyzed). This is unexpected, because water diffuses in minerals faster than indices of metasomatism (e.g., REEs, Ti, Fe). At the equilibration temperatures of the Udachnaya and Liqhobong xenoliths (~1300°C and ~1000 °C, respectively), hydrogen diffusion in peridotites is rapid enough to come to equilibrium within months at the grain scale ($D = \sim10^{-10}$ $m^2s^{-1}$) (Demouchy and Mackwell, 2006). A key feature of metasomatism in the Udachnaya xenoliths is Fe enrichment. Although metasomatic enrichment of Fe affects olivine, opx, and cpx in the Udachnaya xenoliths, water contents in these phases do not correlate with any indicator of metasomatism including Fe enrichment. Diffusion of Fe into olivines and pyroxenes is >1000 times slower than diffusion of water (Chakraborty, 1997; Cherniak and Dimanov, 2010; Spandler and O'Neill, 2010). Therefore, if metasomatic enrichment of Fe is recorded in mineral phases, then metasomatic enrichment of water should also have occurred. The lack of a consistent effect of metasomatism on NAM water content in the Udachnaya and Liqhobong xenoliths demonstrates inconsistency in the link between metasomatism and NAM water content.

Ce and water concentrations are well correlated in MORB and OIB lavas, but there is no similar correlation in peridotites. H2O and Ce have similar incompatibilities in MORB and OIB lavas, yielding consistent H2O/Ce ratios ranging from ~50 to ~350 (Michael, 1995; Workman et al., 2006). However, peridotite H2O/Ce ratios span a much wider range, from 1.9 to 28000 (Fig. 4.5). This suggests that H2O and Ce have different behavior in the mantle than in basalt melts, as evidenced by the absence of a correlation in Fig 4.5. Therefore, incompatible behavior alone does not control H2O and Ce content in the mantle. H2O and Ce appear to be decoupled in peridotites. Curiously, the water and Ce concentrations from the peridotite dataset yield a median H2O/Ce of 113, similar to values typical of MORBs and OIBs. This suggests that although mantle peridotites have a wider range of H2O/Ce than basalts, H2O/Ce ratios in melts from these heterogeneous peridotites are averaged to more homogenous basaltic compositions through aggregation and mixing during melt extraction and storage.

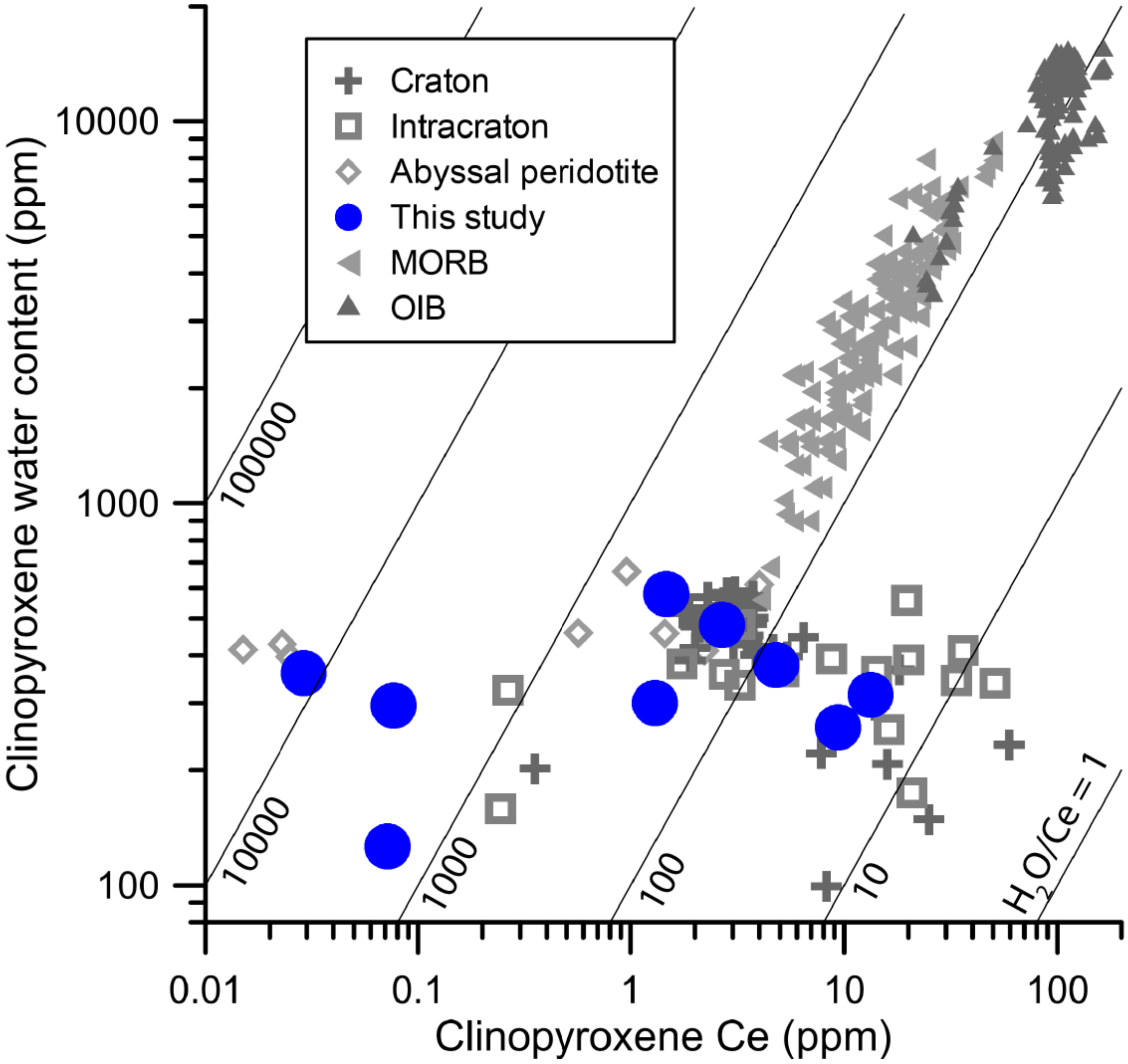

Figure 4.5: Plot of clinopyroxene Ce content versus clinopyroxene water content. The thin black lines represent lines of constant $H_2O$/Ce. Literature data are sorted by tectonic context: cratonal xenoliths (Peslier et al., 2012; Doucet et al., 2014; Hao et al., 2014), intracratonal xenoliths (also contains xenoliths from Ontong Java) (Demouchy et al., 2015; Denis et al., 2015), and abyssal peridotite samples (Warren and Hauri, 2014). For comparison, MORB data (Michael, 1995) and OIB data (Michael, 1995; Workman et al., 2006) are also plotted.

There is no clear correlation between indices of metasomatism and NAM water content in the NVF xenoliths. Orthopyroxene and clinopyroxene water contents do correlate with whole rock CaO and $Na_2O$ suggesting a possible connection to melt extraction or metasomatism, but there is no correlation with typical indices of metasomatism or melt extraction (e.g., cpx Ce/Sm, cpx Cr#; Fig 4.6, cpx water contents not shown). In Fig 4.4b, cpx water content weakly correlates with cpx modal abundance. Given this correlation and that the dominant host of CaO and $Na_2O$ in peridotites is cpx, it is expected that cpx and opx water contents correlate with whole rock CaO and $Na_2O$. Despite wide variation in NVF xenolith pyroxene water content from dry, craton-like values (<100 ppm) to extremely high water content (~600 ppm), pyroxene water content does not seem to be directly controlled by melt extraction or metasomatic processes.

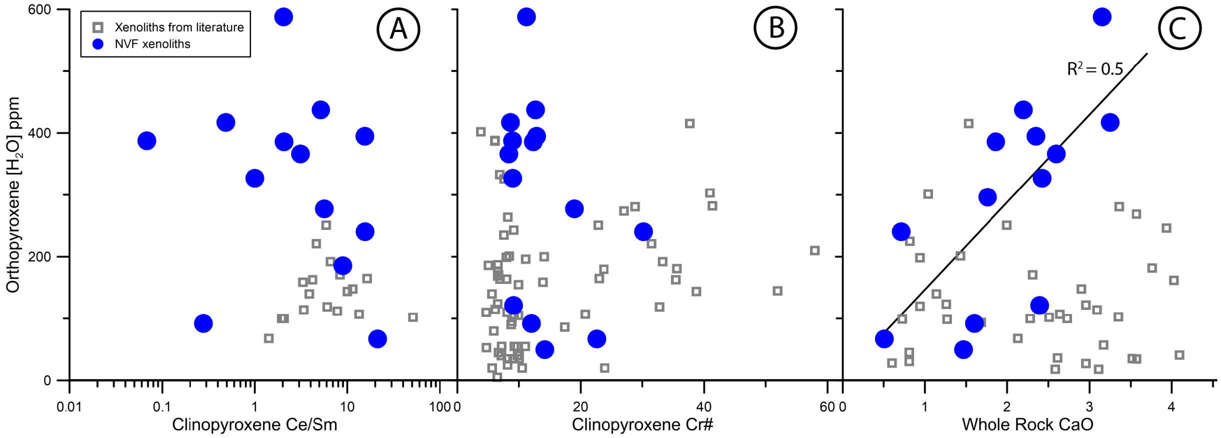

Fig. 4.6: Plots of cpx Ce/Sm, cpx Cr#, and whole rock CaO versus orthopyroxene water content. Whole rock CaO correlates with opx water content in the NVF xenoliths. There is no clear correlation between cpx Ce/Sm or cpx Cr# and opx water content.

### 4.6.4 Relationship of NAM water content and hydrous minerals

Hydrous minerals in mantle peridotites are not unusual as minor phases. Most hydrous minerals in peridotites are associated with growth during melt or fluid metasomatism. Xenoliths from any tectonic setting may contain hydrous minerals, but they are most common in alkali basalt and kimberlite hosted xenoliths from SCLM (Frost, 2006). As an example, hydrous-mineral-bearing peridotites represent 13% of samples in the literature compilation of Fig. 4.1 and Fig. 4.2. However, composite xenoliths that contain metasomatic veins are usually excluded from study, and therefore hydrous-mineral-bearing peridotites may be underrepresented in the literature. These samples are important for understanding the behavior of water in the mantle because they can contain substantially more bulk water than anhydrous peridotites. For example, a peridotite with only ~2 modal % amphibole or phlogopite, will contain most of its water within hydrous minerals instead of NAMs.

Intuitively, one might expect NAM water contents to be higher in hydrous-mineral-bearing peridotites than in anhydrous peridotites. Previous studies have attempted to identify a correlation between hydrous mineral abundance and NAM water content (Demouchy et al., 2015; Denis et al., 2015; Demouchy and Bolfan-Casanova, 2016). In these studies no correlation was observed. In detail, NAMs are expected to be in thermodynamic equilibrium with hydrous minerals in the same sample with respect to water content (due to rapid hydrogen diffusion). Therefore, it is the activity of water in the hydrous phases and not their abundance that should control NAM water content. Surprisingly however, NAM water content in anhydrous and hydrous-mineral-bearing peridotites also broadly overlap (Fig. 4.1).

NAM water contents in hydrous-mineral-bearing peridotites are well below calculated saturation limits. For example, water content at saturation of cpx and opx with ~4 wt% $Al_2O_3$ at 1000 °C and 1.5 GPa (a "typical" SCLM spinel-facies pyroxene) is estimated to be ~1250 to 2000 ppm and ~1500 ppm, respectively (Mierdel and Keppler, 2004; Hauri et al., 2006; Gavrilenko, 2008). Most measured NAM water contents previously reported for hydrous-mineral-bearing peridotites are well below these estimates (Fig. 4.1), which indicates the water activity recorded in these peridotites is low. Water activity in a NAM at a given P and T can be approximated as $a_{H_2O} \approx C_{H_2O}^{NAM}/C_{H_2O}^{SAT}$, where $a_{H_2O}$ is water activity, $C_{H_2O}^{NAM}$ is the water content in a given NAM, and $C_{H_2O}^{SAT}$ is the NAM water content at saturation (the equation is approximate because it does not take into account different hydrogen substitution mechanisms) (Lamb and Popp, 2009). Thus, given these roughly constrained saturation limits and the range of hydrous-mineral-bearing peridotite NAM water contents (67 to 588 ppm), water activity in most hydrous-mineral-bearing peridotites ranges from ~0.02 to 0.3. Water activity can also be estimated from amphibole mineral equilibria. Lamb and Popp (2009) estimated a water activity of <0.04 in an amphibole-bearing spinel peridotite xenolith from Dish Hill, CA using this method. Thus, the water activity suggested by both amphibole compositions and NAM water contents in hydrous-mineral-bearing peridotites appear mutually consistent and are for the most part low.

The similarity in NAM water contents in anhydrous and hydrous-mineral-bearing peridotites (Fig. 4.1) suggests that both peridotite types have similar water activity. The water content at saturation is controlled by composition, temperature and pressure. Both anhydrous and hydrous-mineral-bearing peridotites often appear in the same suites of peridotites and commonly record overlapping equilibration temperatures, pressures, and mineral compositions (e.g., Yang et al., 2008; Demouchy et al., 2015). Because of these similarities, both peridotites should have similar water contents at saturation. Having both similar measured NAM water contents and estimated water contents at saturation implies that the peridotites record similar water activities.

One explanation for this similarity is that anhydrous and hydrous-mineral-bearing peridotites undergo diffusive exchange with one another that results in equilibration of NAM water content and water activity. The diffusivity of water in peridotites is rapid. For example, olivine diffusivity in SCLM (~1000 °C) or in asthenospheric mantle (~1350 °C) has been estimated to be ~$1\mathrm{x}10^{-12}$ $\mathrm{m}^2\mathrm{s}^{-1}$ or ~$2\mathrm{x}10^{-10}$ $\mathrm{m}^2\mathrm{s}^{-1}$, respectively (Demouchy and Mackwell, 2006; Demouchy and Bolfan-Casanova, 2016). Given these diffusivities, over 10 Ma the typical diffusion length scale ($2\sqrt{Dt}$) for water in SCLM peridotites is ~35 m, or ~500 m for asthenospheric peridotites. Because most anhydrous and hydrous-mineral-bearing peridotites from the same locality have overlapping equilibration temperatures, we infer that both peridotite types derive from similar depths. Metasomatism in lithospheric mantle is common, and veins are observed in many xenolith suites (e.g. Warren, 2016). Because metasomatism enriches peridotites in incompatible species, metasomatic melts or fluids responsible for vein formation should have high water content and water activity, as will the vein at the time of formation. Over time, however, diffusion will equilibrate water activity between the vein and surrounding peridotite, lowering the water activity in the vein and increasing it in the unmetasomatized peridotite (Fig. 4.7). Hydrous minerals present in metasomatized peridotite will either dehydrogenate or break down as water activity decreases, providing additional water to enrich the surrounding, initially dryer peridotite. Eventually, water activity in veins or metasomatized peridotite and unmetasomatized peridotite will come to equilibrium with a slightly higher water activity than was initially present before fluid or melt injection. As long as the diffusion length scale is equal to or greater than the mean spacing separating metasomatic veins or channels, diffusive equilibration will act to equalize water activity in peridotites from a given depth, irrespective of their prior history of melt depletion or metasomatism.

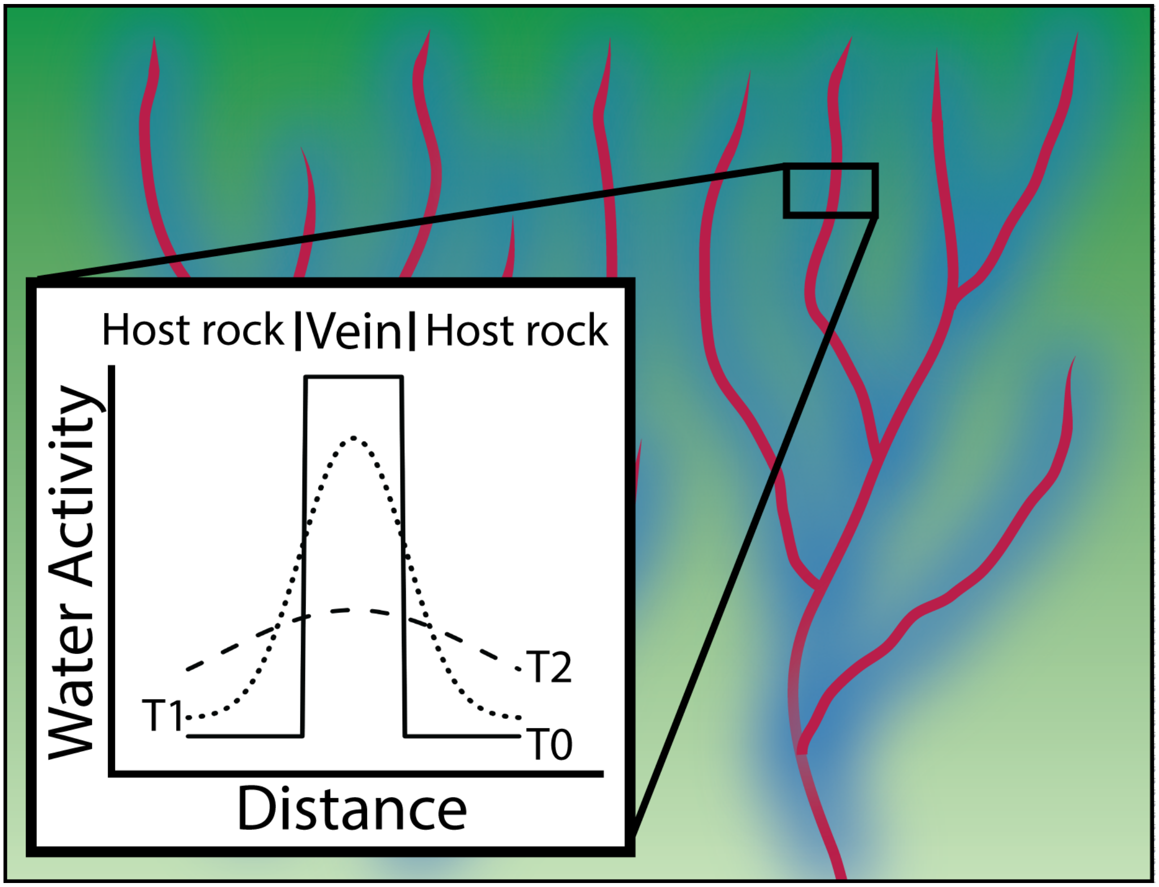

Fig. 4.7: Depiction of water diffusion between metasomatic veins and surrounding peridotite. High water activity in veins (red) diffuses water into the surrounding peridotite and increases its water activity (blue). Inset figure: Initially, the metasomatic vein has higher water activity than the surrounding peridotite (T0). However, over time water activity changes as water diffuses out of the vein (T1). Eventually, the metasomatic vein approaches equilibrium with the surrounding peridotite (T2). Through diffusion, the water activity of the metasomatic vein is reduced, while the water activity of the surrounding peridotite is enriched.

The above model provides an explanation for the general lack of strong correlations between NAM water content and either metasomatism or melt extraction in mantle peridotites. Diffusion reduces variability in NAM water content, blurring or eliminating these correlations. Melt extraction and metasomatism will respectively deplete or enrich incompatible species in peridotites. However, only water can be transported significant distances via diffusion from metasomatized to unmetasomatized portions of the mantle. Consequently, mantle that has undergone melt extraction will initially be depleted in both incompatible tracers (e.g., Ce) and water, but over time water concentrations will increase due to diffusive influx from nearby metasomatized regions. As a result, unmetasomatized, melt-depleted peridotites will evolve to have anomalously high H2O/Ce ratios due to re-enrichment of water, but not Ce. Similarly, metasomatized portions of the mantle will initially be enriched in both incompatible tracers and water, but over time water will be transported to surrounding water-depleted peridotites via diffusion, resulting in low H2O/Ce ratios in the metasomatized veins. These predictions are consistent with observed variations in H2O/Ce in many peridotite suites. For example, melt-depleted abyssal peridotites have H2O/Ce ratios that extend to much higher values than observed in basaltic melts, with ratios ranging from 150 up to ~28,000 (Warren and Hauri, 2014) (Fig. 4.5). Similarly, H2O/Ce ratios in metasomatized peridotites from the Kaapvaal and North China cratons extend to very low H2O/Ce (~4), again falling outside the range observed in primitive MORB and OIB (Peslier et al., 2012; Hao et al., 2014) (Fig. 4.5).

In MORBs and OIBs, water and Ce display similar behavior during melting and magmatic differentiation and primitive basalts span a relatively narrow range of H2O/Ce ratios (50 to 350). However, water diffusion in the mantle decouples it from Ce, resulting in a much wider range of H2O/Ce than in MORBs and OIBs (Fig. 4.5). Globally, mantle peridotites have clinopyroxene water concentrations that only span ~1 order of magnitude, whereas Ce concentrations span nearly 4 orders of magnitude. Given the similar incompatibility of Ce and water during processes such as partial melting, the greatly reduced concentration variability observed for water relative to Ce requires that processes such as diffusive re-equilibration act to destroy heterogeneity generated by partial melting and metasomatism. As a result, correlations between indices of metasomatism or melt extraction and NAM water content are unlikely to be observed in peridotite suites except where these processes have affected peridotite compositions very recently.

Although diffusion strongly affects the activity of water in typical lithospheric or asthenospheric mantle, this process does not likely control the Colorado Plateau xenoliths that are studied in this paper. Farallon flat-slab subduction dramatically cooled the Colorado Plateau lithospheric mantle to temperatures less than 650 C, resulting in significantly reduced diffusion rates compared to ~1000 C. Diffusion is too slow at these temperatures to allow for meter-scale diffusive equilibration of water activity between modally hydrated and anhydrous peridotites. Instead, water contents in the hydrous-mineral-bearing peridotites are controlled by grain-scale equilibration with hydrous phases that results in low water content. As hydrous minerals cool, the equilibrium water activity of these minerals decreases and causes the hydrous minerals to take up water from surrounding NAMs. Because hydrous minerals dominate the water budgets of hydrous-mineral-bearing peridotites, changes in water activity in the hydrous minerals will control the water activity of the other NAMs. Therefore, cooling during Farallon subduction will decrease water content in NAMs within hydrous-mineral-bearing peridotites such that NVF hydrous-mineral-bearing peridotites have a similar distribution of water content to the anhydrous peridotites.

## 4.7 CONCLUSIONS:

Previous studies have identified correlations between NAM water content and indices of metasomatism or melt extraction. However in detail, these correlations do not demonstrate robust controls of NAM water content. Similarly, although the NVF xenoliths show relatively wide variability in NAM water content, NVF xenoliths do not clearly define relationships between NAM water content and metasomatism or melt extraction.

Comparing the NAM water contents of anhydrous and hydrous-mineral-bearing peridotite can further test the connection between metasomatism and enrichment of NAM water content. Hydrous minerals require elevated peridotite water activity to form. Therefore, hydrous-mineral-bearing peridotites should have higher NAM water contents than anhydrous peridotites. However, anhydrous and hydrous-mineral-bearing peridotites in both the NVF xenolith suite and in the global compiled literature do not show a difference in their range of either NAM water content or water activity.

We propose that over geologic time the large diffusivity of water in peridotites results in equilibration of water activity and a reduction in the variability of NAM water content in the mantle. Melt-extracted residues that are water-poor are replenished in water via diffusion, while metasomatized veins or channels that are initially water-rich diffuse water to surrounding peridotites. Diffusion of water in the mantle explains the rarity of correlations between NAM water content and indices of either metasomatism or melt extraction, because over time diffusion should weaken and destroy these correlations. Equilibration of water activity between portions of SCLM can explain why anhydrous and hydrous-mineral-bearing peridotites have similar NAM water contents and water activities. Finally, diffusive equilibration of water activity can explain why, despite similar incompatibilities, cpx Ce concentration varies by approximately four orders of magnitude in peridotites, while cpx water contents vary by only one order of magnitude. This results in the observed wide range of cpx $H_2O$/Ce ratios in peridotites relative to MORBs or OIBs. The relatively narrow range of MORB and OIB $H_2O$/Ce ratios is similar to the median peridotite $H_2O$/Ce ratio, suggesting that MORB and OIB $H_2O$/Ce ratios are formed via the mixing of melts from different mantle portions.

# Chapter 5: Conclusions

Xenoliths from diatremes in the central Colorado Plateau reveal a long history that is dominated by subduction processes. The Colorado Plateau is composed of two crustal provinces: the Yavapai and Mazatzal, which are both thought to be accreted arcs. At ~1.4 Ga, the Colorado Plateau SCLM was affected by a major magmatic event, likely related to Proterozoic subduction. Finally, in the Cenozoic, Farallon flat slab subduction cooled, hydrated, and metasomatized the Colorado Plateau SCLM.

The main conclusions of the project are:

1) The 1.4 Ga granite magmatic event was not caused by delamination or radiogenic heat build-up. Instead, it is likely related to magma or fluid percolation during subduction.

2) Stable isotope data ($\delta^{18}O$ and $\delta D$), combined with trace element geochemistry, suggest that the fluid that formed the hydrous minerals in the NVF xenoliths is a slab-derived, most likely related to Farallon flat-slab subduction. In addition, fluids derived from the serpentinized lithospheric mantle of the Farallon flat slab are the most likely metasomatic agent. Integration of stable isotope data with other geochemical tracers of subduction potentially provides a method for probing Archean lithospheric mantle for evidence of early subduction.

3) Pyroxene water contents in the NVF xenoliths and in previous studies are not clearly controlled by metasomatic or melt extraction processes. Instead, pyroxene water content is controlled through diffusive exchange. Water activity in peridotites equilibrates

with surrounding rock, decreasing the overall variability of water activity and NAM water content in the mantle.

# Appendix A: Supplement to Chapter 2

## APPENDIX A.1: CLINOPYROXENE MAJOR AND TRACE ELEMENT DATA

**Table A1: Clinopyroxene major and trace elements**

| | **MR-ATG-13 Average** | **2σ** | **N106-GN Average** | **2σ** | **N61-GN Average** | **2σ** | **EMGN24 Average** | **2σ** | **N16-GN Average** | **2σ** | **N126-GN Average** | **2σ** | **EMGN2 Average** | **2σ** |
|---|---|---|---|---|---|---|---|---|---|---|---|---|---|---|
| | **Group D** | | **Group D** | | **Group D<br>R&S (1993)** | | **Group D** | | **Group D<br>R&S (1993)** | | **Group D** | | **Group T** | |
| | **n = 5** | | **n = 8** | | | | **n = 5** | | | | **n = 7** | | **n = 4** | |
| **$SiO_2$** | 52.20 | (0.06) | 52.03 | (0.37) | *52.80* | | 53.25 | (0.57) | *51.40* | | 51.88 | (0.12) | 52.87 | (0.45) |
| **$TiO_2$** | 0.13 | (0.02) | 0.21 | (0.02) | *0.32* | | 0.48 | (0.04) | *0.37* | | 0.08 | (0.01) | 0.19 | (0.01) |
| **$Al_2O_3$** | 5.52 | (0.06) | 4.84 | (0.36) | *5.68* | | 5.54 | (0.63) | *5.95* | | 6.99 | (0.12) | 5.62 | (0.47) |
| **$Cr_2O_3$** | 1.13 | (0.04) | 0.68 | (0.04) | *0.84* | | 1.04 | (0.07) | *0.71* | | 1.05 | (0.04) | 0.76 | (0.03) |
| **FeO** | 1.98 | (0.14) | 1.89 | (0.11) | *1.76* | | 2.31 | (0.34) | *2.86* | | 2.21 | (0.14) | 2.23 | (0.35) |
| **MnO** | 0.09 | (0.01) | 0.06 | (0.01) | | | 0.08 | (0.01) | | | 0.11 | (0.01) | 0.09 | (0.02) |
| **MgO** | 15.80 | (0.30) | 16.60 | (0.30) | *14.90* | | 15.53 | (0.75) | *15.10* | | 15.16 | (0.15) | 15.64 | (0.89) |
| **CaO** | 21.94 | (0.37) | 22.20 | (0.26) | *21.20* | | 20.18 | (0.92) | *22.10* | | 21.44 | (0.19) | 21.14 | (1.52) |
| **$Na_2O$** | 1.33 | (0.04) | 1.42 | (0.12) | *2.03* | | 2.04 | (0.19) | *1.23* | | 1.52 | (0.09) | 1.52 | (0.11) |
| **Total** | 100.14 | | 99.96 | | *99.53* | | 100.48 | | *99.72* | | 100.48 | | 100.07 | |
| | | | | | | | | | | | | | | |
| | **n = 5** | | **n = 8** | | | | **n = 5** | | | | **n = 7** | | **n = 4** | |
| **La** | 0.01 | (0.00) | 0.18 | (0.05) | | | 0.74 | (0.05) | | | bd | | 0.61 | (0.03) |
| **Ce** | 0.07 | (0.01) | 0.33 | (0.03) | *1.30* | | 2.69 | (0.13) | *0.58* | | bd | | 1.46 | (0.05) |
| **Pr** | | | | | | | 0.51 | (0.02) | | | | | 0.17 | (0.00) |
| **Nd** | 0.24 | (0.02) | 0.86 | (0.11) | *3.10* | | 3.20 | (0.14) | *1.70* | | 0.04 | (0.00) | 0.79 | (0.03) |
| **Sm** | 0.26 | (0.02) | 0.67 | (0.08) | *1.30* | | 1.31 | (0.05) | *1.40* | | 0.15 | (0.01) | 0.47 | (0.03) |
| **Eu** | 0.14 | (0.01) | 0.30 | (0.04) | *0.59* | | 0.50 | (0.03) | *0.60* | | 0.10 | (0.00) | 0.24 | (0.01) |
| **Gd** | 0.71 | (0.05) | 1.38 | (0.14) | | | 1.68 | (0.07) | | | 0.56 | (0.03) | 1.08 | (0.05) |
| **Dy** | 1.50 | (0.07) | 2.19 | (0.28) | *1.60* | | 1.49 | (0.07) | *3.10* | | 1.33 | (0.05) | 2.00 | (0.10) |
| **Er** | 1.21 | (0.07) | 1.45 | (0.21) | *1.00* | | 0.54 | (0.09) | *2.10* | | 1.12 | (0.04) | 1.49 | (0.03) |
| **Yb** | 1.25 | (0.08) | 1.33 | (0.23) | *1.00* | | 0.34 | (0.10) | *2.40* | | 1.23 | (0.03) | 1.47 | (0.08) |
| **Lu** | 0.19 | (0.01) | 0.18 | (0.03) | | | 0.04 | (0.01) | | | 0.18 | (0.00) | 0.22 | (0.01) |
| **Rb** | 0.00 | (0.00) | 0.01 | (0.02) | | | 0.04 | (0.02) | | | 0.08 | (0.07) | 0.02 | (0.01) |
| **Th** | 0.00 | (0.00) | 0.00 | (0.00) | | | 0.01 | (0.01) | | | 0.00 | (0.00) | 0.03 | (0.00) |
| **U** | 0.00 | (0.00) | 0.01 | (0.00) | | | 0.00 | (0.00) | | | 0.00 | (0.00) | 0.01 | (0.00) |
| **Nb** | 0.01 | (0.00) | 0.01 | (0.00) | | | 0.08 | (0.02) | | | 0.00 | (0.00) | 0.30 | (0.05) |
| **Ta** | 0.00 | (0.00) | 0.00 | (0.00) | | | 0.02 | (0.00) | | | 0.00 | (0.00) | 0.02 | (0.00) |
| **Pb** | 0.02 | (0.03) | 0.30 | (0.09) | | | 0.31 | (0.19) | | | 0.01 | (0.01) | 0.04 | (0.03) |
| **Sr** | 5.64 | (1.84) | 39.40 | (7.16) | *85.00* | | 65.69 | (8.62) | *9.50* | | 0.91 | (0.65) | 22.71 | (0.69) |
| **Zr** | 1.65 | (0.08) | 5.58 | (0.70) | *6.60* | | 19.37 | (0.86) | *7.60* | | 0.07 | (0.01) | 0.81 | (0.03) |
| **Hf** | 0.11 | (0.01) | 0.30 | (0.01) | | | 0.78 | (0.04) | | | 0.02 | (0.00) | 0.11 | (0.01) |
| **Y** | 9.99 | (0.32) | 11.75 | (1.62) | | | 5.84 | (0.64) | | | 9.10 | (0.18) | 12.42 | (0.45) |
| **V** | 262 | (6.58) | 229 | (10.11) | *260* | | 316 | (14.78) | *280* | | 240 | (5.85) | 238 | (1.61) |

**Reference: R&S (1993): Roden and Shimizu, (1993); bd: below detection**

Table A1: Clinopyroxene major and trace elements

| | N17-GN Average | 2σ | N55-GN Average | 2σ | EMGN21 Average | 2σ | N178-GN Average | 2σ | N23-GN Average | 2σ | N53-GN Average | 2σ | EMGN12 Average | 2σ |
|---|---|---|---|---|---|---|---|---|---|---|---|---|---|---|
| | Group T | | Group E | | Group E | | Group E | | Group D<br>R&S (1993) | | Group D | | Group D | |
| | **n = 10** | | **n = 3** | | **n = 1** | | **n = 7** | | | | **n = 5** | | **n = 7** | |
| **SiO2** | 51.85 | (0.13) | 53.53 | (0.53) | 55.37 | | 54.56 | (0.13) | *54.10* | | 52.25 | (1.41) | 51.75 | (1.21) |
| **TiO2** | 0.04 | (0.01) | 0.07 | (0.03) | 0.00 | | 0.01 | (0.01) | *0.33* | | 0.24 | (0.06) | 0.05 | (0.07) |
| **Al2O3** | 5.07 | (0.17) | 2.41 | (0.84) | 1.34 | | 0.72 | (0.03) | *3.67* | | 6.69 | (0.89) | 5.20 | (0.33) |
| **Cr2O3** | 1.06 | (0.04) | 0.50 | (0.02) | 0.38 | | 0.46 | (0.05) | *1.35* | | 0.90 | (0.09) | 1.00 | (0.16) |
| **FeO** | 1.88 | (0.08) | 1.65 | (0.21) | 1.26 | | 1.60 | (0.07) | *1.98* | | 2.08 | (0.54) | 2.04 | (0.41) |
| **MnO** | 0.08 | (0.01) | 0.08 | (0.02) | 0.08 | | 0.06 | (0.01) | | | 0.08 | (0.05) | 0.08 | (0.04) |
| **MgO** | 15.91 | (0.20) | 17.53 | (0.21) | 17.58 | | 17.60 | (0.06) | *15.90* | | 14.84 | (1.63) | 15.77 | (1.91) |
| **CaO** | 23.08 | (0.27) | 23.38 | (1.08) | 24.10 | | 24.24 | (0.07) | *21.00* | | 21.27 | (1.50) | 22.42 | (2.10) |
| **Na2O** | 1.01 | (0.06) | 0.69 | (0.26) | 0.57 | | 0.58 | (0.06) | *2.28* | | 1.90 | (0.24) | 1.00 | (0.27) |
| **Total** | 100.00 | | 99.87 | | 100.72 | | 99.86 | | *100.61* | | 100.29 | (1.73) | 99.36 | (1.07) |
| | | | | | | | | | | | | | | |
| | **n = 10** | | **n = 3** | | **n = 1** | | **n = 7** | | | | **n = 6** | | **n = 8** | |
| **La** | 0.04 | (0.01) | 1.17 | (0.22) | 4.75 | | 3.44 | (0.28) | | | 0.01 | (0.00) | 0.01 | (0.01) |
| **Ce** | 0.03 | (0.01) | 2.02 | (0.27) | 4.80 | | 9.36 | (0.30) | *0.93* | | 0.03 | (0.00) | 0.01 | (0.01) |
| **Pr** | | | | | 0.38 | | | | | | 0.02 | (0.00) | 0.00 | |
| **Nd** | bd | | 0.63 | (0.06) | 1.19 | | 4.84 | (0.51) | *2.10* | | 0.31 | (0.02) | bd | |
| **Sm** | 0.01 | (0.00) | 0.13 | (0.03) | 0.10 | | 0.60 | (0.09) | *1.20* | | 0.43 | (0.05) | 0.02 | (0.00) |
| **Eu** | 0.01 | (0.00) | 0.06 | (0.01) | 0.04 | | 0.16 | (0.02) | *0.41* | | 0.23 | (0.02) | 0.02 | (0.01) |
| **Gd** | 0.12 | (0.01) | 0.27 | (0.07) | 0.08 | | 0.29 | (0.04) | | | 1.03 | (0.08) | 0.15 | (0.04) |
| **Dy** | 0.52 | (0.02) | 0.51 | (0.19) | 0.12 | | 0.28 | (0.02) | *0.52* | | 1.85 | (0.13) | 0.57 | (0.06) |
| **Er** | 0.56 | (0.03) | 0.34 | (0.17) | 0.19 | | 0.27 | (0.02) | *0.26* | | 1.34 | (0.08) | 0.57 | (0.08) |
| **Yb** | 0.71 | (0.04) | 0.36 | (0.17) | 0.36 | | 0.44 | (0.02) | *0.26* | | 1.40 | (0.13) | 0.70 | (0.06) |
| **Lu** | 0.11 | (0.01) | 0.05 | (0.02) | 0.06 | | 0.08 | (0.00) | | | 0.19 | (0.02) | 0.11 | (0.02) |
| **Rb** | bd | | 0.13 | (0.12) | 0.37 | | 0.04 | (0.02) | | | bd | | bd | |
| **Th** | bd | | 0.04 | (0.01) | 0.28 | | 0.00 | (0.00) | | | 0.00 | (0.00) | bd | |
| **U** | 0.01 | (0.00) | 0.04 | (0.01) | 0.05 | | 0.01 | (0.00) | | | bd | | bd | |
| **Nb** | 0.004 | (0.001) | 0.49 | (0.28) | 0.20 | | 0.00 | (0.00) | | | 0.01 | (0.00) | 0.00 | (0.00) |
| **Ta** | bd | | 0.00 | (0.00) | 0.02 | | bd | | | | | | | |
| **Pb** | 0.03 | (0.01) | 0.54 | (0.22) | 0.97 | | 1.12 | (0.22) | | | | | | |
| **Sr** | 3.15 | (1.27) | 77.27 | (22.65) | 43.49 | | 443.00 | (87.52) | *36.00* | | 1.81 | (0.33) | 0.59 | (0.94) |
| **Zr** | bd | | 0.05 | (0.01) | 0.28 | | 1.39 | (0.13) | *8.70* | | 1.00 | (0.10) | bd | |
| **Hf** | bd | | 0.02 | (0.01) | 0.01 | | 0.06 | (0.01) | | | 0.12 | (0.02) | 0.00 | (0.00) |
| **Y** | 4.22 | (0.18) | 2.94 | (1.35) | 1.20 | | 1.97 | (0.08) | | | 11.30 | (0.81) | 4.39 | (0.45) |
| **V** | 233 | (5.20) | 199 | (41.49) | 171 | | 141 | (4.77) | *420* | | | | | |

Reference: R&S (1993): Roden and Shimizu, (1993); bd: below detection

Table A1: Clinopyroxene major and trace elements

| | EMMR4 Average | 2σ | EMMR25 Average | 2σ | EMGN6 Average | 2σ | EMGN29 Average | 2σ | EMGN9 Average | 2σ | EMGN27 Average | 2σ | NMNH Cr-Augite Average | 2σ |
|---|---|---|---|---|---|---|---|---|---|---|---|---|---|---|
| | **Group D** | | **Group T** | | **Group T** | | **Group T** | | **Group T** | | **Group E** | | | |
| | **n = 1** | | **n = 1** | | **n = 1** | | **n = 6** | | **n = 4** | | **n = 6** | | **n = 36** | |
| **SiO2** | 53.48 | | 56.06 | | 53.25 | | 51.75 | (1.02) | 53.61 | (1.58) | 54.91 | (3.22) | 50.66 | (1.19) |
| **TiO2** | 0.14 | | 0.02 | | 0.07 | | 0.05 | (0.01) | 0.10 | (0.05) | 0.00 | (0.04) | 0.48 | (0.08) |
| **Al2O3** | 5.36 | | 0.37 | | 4.92 | | 5.44 | (0.83) | 4.20 | (1.30) | 1.56 | (1.01) | 8.06 | (0.28) |
| **Cr2O3** | 1.33 | | 0.06 | | 1.06 | | 1.11 | (0.23) | 0.79 | (0.32) | 0.98 | (1.05) | 0.87 | (0.12) |
| **FeO** | 2.08 | | 1.99 | | 2.52 | | 2.03 | (0.35) | 1.65 | (0.19) | 1.33 | (0.40) | 4.80 | (0.32) |
| **MnO** | 0.13 | | 0.12 | | 0.09 | | 0.08 | (0.02) | 0.09 | (0.01) | 0.05 | (0.06) | 0.13 | (0.03) |
| **MgO** | 15.06 | | 18.12 | | 16.12 | | 15.77 | (1.04) | 15.86 | (0.64) | 17.47 | (0.82) | 17.25 | (0.40) |
| **CaO** | 22.11 | | 24.23 | | 21.93 | | 22.33 | (0.99) | 22.68 | (0.55) | 23.91 | (0.72) | 17.28 | (0.31) |
| **Na2O** | 1.47 | | 0.46 | | 0.88 | | 1.24 | (0.23) | 1.40 | (0.24) | 0.79 | (0.25) | 0.83 | (0.16) |
| **Total** | 101.17 | | 101.54 | | 100.91 | | 99.85 | | 100.41 | (0.73) | 101.01 | | 100.38 | |
| | | | | | | | | | | | | | | |
| | **n = 2** | | **n = 2** | | **n = 2** | | **n = 6** | | **n = 5** | | **n = 9** | | | |
| **La** | bd | | 0.57 | (0.07) | 0.20 | (0.01) | 0.03 | (0.09) | 0.40 | (0.09) | 0.87 | (0.27) | | |
| **Ce** | bd | | 0.98 | (0.14) | 0.24 | (0.01) | 0.02 | (0.07) | 0.89 | (0.16) | 2.55 | (0.77) | | |
| **Pr** | bd | | 0.08 | (0.02) | 0.01 | (0.00) | 0.00 | (0.00) | 0.09 | (0.02) | 0.36 | (0.11) | | |
| **Nd** | bd | | 0.43 | (0.20) | 0.04 | | bd | | 0.37 | (0.07) | 1.41 | (0.46) | | |
| **Sm** | 0.11 | (0.02) | 0.36 | (0.17) | 0.04 | | 0.02 | (0.01) | 0.20 | (0.04) | 0.18 | (0.06) | | |
| **Eu** | 0.07 | (0.01) | 0.18 | (0.05) | 0.03 | (0.00) | 0.02 | (0.02) | 0.10 | (0.02) | 0.04 | (0.01) | | |
| **Gd** | 0.42 | (0.04) | 0.85 | (0.21) | 0.24 | (0.03) | 0.18 | (0.03) | 0.55 | (0.10) | 0.06 | (0.03) | | |
| **Dy** | 0.88 | (0.10) | 1.65 | (0.48) | 0.73 | (0.05) | 0.61 | (0.05) | 1.37 | (0.18) | 0.02 | (0.01) | | |
| **Er** | 0.62 | (0.06) | 1.28 | (0.35) | 0.71 | (0.05) | 0.59 | (0.05) | 1.21 | (0.14) | 0.01 | (0.01) | | |
| **Yb** | 0.60 | (0.12) | 1.37 | (0.30) | 0.85 | (0.01) | 0.70 | (0.04) | 1.36 | (0.15) | 0.01 | (0.01) | | |
| **Lu** | 0.08 | (0.01) | 0.20 | (0.03) | 0.13 | (0.00) | 0.11 | (0.01) | 0.21 | (0.03) | 0.00 | (0.00) | | |
| **Rb** | bd | | bd | | 0.58 | (0.68) | 0.23 | (0.24) | 0.11 | (0.10) | 0.38 | (0.74) | | |
| **Th** | bd | | bd | | 0.01 | | bd | | 0.01 | (0.01) | 0.02 | (0.03) | | |
| **U** | 0.03 | (0.09) | 0.21 | (0.08) | 0.00 | (0.00) | 0.01 | (0.01) | 0.01 | (0.01) | 0.01 | (0.01) | | |
| **Nb** | bd | | bd | | 0.57 | (0.00) | 0.00 | (0.00) | 0.22 | (0.19) | 0.02 | (0.04) | | |
| **Ta** | | | | | | | 0.00 | (0.00) | 0.01 | (0.00) | | | | |
| **Pb** | | | | | | | 0.09 | (0.33) | 0.11 | (0.18) | | | | |
| **Sr** | 4.05 | (9.79) | 332.85 | (79.62) | 3.55 | (0.09) | 3.47 | (10.68) | 8.05 | (6.21) | 78.57 | (93.60) | | |
| **Zr** | 0.28 | (0.05) | 0.32 | (0.03) | 0.01 | | 0.00 | (0.01) | 1.29 | (0.19) | 0.28 | (0.08) | | |
| **Hf** | 0.05 | (0.01) | 0.04 | (0.01) | 0.00 | (0.00) | bd | | 0.04 | (0.01) | 0.01 | (0.01) | | |
| **Y** | 5.44 | (0.42) | 10.36 | (2.73) | 5.59 | (0.45) | 4.57 | (0.42) | 9.36 | (1.11) | 0.08 | (0.05) | | |
| **V** | | | | | | | 217 | (13.46) | 246 | (21.82) | | | | |

Reference: R&S (1993): Roden and Shimizu, (1993); bd: below detection

**Table A1: Clinopyroxene major and trace elements**

| | BCR-2G<br>Average | 2σ |
|---|---|---|
| **SiO2** | | |
| **TiO2** | | |
| **Al2O3** | | |
| **Cr2O3** | | |
| **FeO** | | |
| **MnO** | | |
| **MgO** | | |
| **CaO** | | |
| **Na2O** | | |
| **Total** | | |
| | **n = 22** | |
| **La** | 25.50 | (1.33) |
| **Ce** | 54.50 | (3.14) |
| **Pr** | 6.46 | (0.11) |
| **Nd** | 29.14 | (1.27) |
| **Sm** | 6.75 | (0.31) |
| **Eu** | 1.97 | (0.10) |
| **Gd** | 6.55 | (0.36) |
| **Dy** | 6.40 | (0.29) |
| **Er** | 3.61 | (0.15) |
| **Yb** | 3.42 | (0.18) |
| **Lu** | 0.51 | (0.03) |
| **Rb** | 47.90 | (1.98) |
| **Th** | 5.97 | (0.22) |
| **U** | 1.70 | (0.09) |
| **Nb** | 12.60 | (0.72) |
| **Ta** | 0.78 | (0.03) |
| **Pb** | 10.60 | (0.49) |
| **Sr** | 349.28 | (14.48) |
| **Zr** | 178.11 | (7.66) |
| **Hf** | 4.61 | (0.17) |
| **Y** | 32.91 | (1.58) |
| **V** | 442 | (12.83) |

**Reference: R&S (1993): Roden and Shimizu, (1993); bd: below detection**

## APPENDIX A.2: SAMPLE PETROGRAPHIC DESCRIPTIONS

This section presents a mineralogic and petrographic summary of each sample. Mineral modal abundances are visually estimated in thin section, not point counted. All samples were spinel peridotites, except N23-GN, EMGN21, EMGN24, N106-GN and N55-GN. N23-GN was interpreted by Roden et al. (1990) to have been garnet peridotite with garnets having been replaced by chlorite. Their interpretation was based largely on HREE depletion in clinopyroxene, which is typical of cpx in equilibrium with garnet, and the garnet-like shape of the chlorite clusters. We have identified two other xenoliths with cpx REE patterns similar to N23-GN: EMGN21 and EMGN24. Both of these samples have depleted HREE concentration and chlorite interpreted as replacing garnet, similar to N23-GN. N55-GN has garnet rims around Al-spinel cores (see Smith and Levy, 1976). N106-GN was noted to have garnet rims around spinel (personal communication, D. Smith), but we were unable to confirm this texture.

Our petrologic observations agree with the findings of Smith (1979) that Green Knobs (35.9533° N, 109.0227° W) xenoliths have three hydrous peridotite assemblages:

1) Mineral assemblages that contain *aluminous-spinel* (Al-Spinel) and are poor in hydrous phases (~ <5% by mode).

2) Mineral assemblages that contain amphibole and chlorite. These samples generally all contain *chlorite clusters*-- a textural feature formed by aluminous phases (e.g., Al-spinel, garnet) reacting with fluid and olivine to form chlorite. In spinel

peridotites, these chlorite clusters contain Cr-spinel interpreted to be the Al-depleted reaction product of the original Al-spinel.

3) Mineral assemblages that contain *abundant antigorite* relative to the other two assemblage types (>5% by mode). A key textural feature of this assemblage is that platy antigorite crystals are found throughout the sample. In addition, antigorite rims chlorite clusters and individual chlorite grains. This assemblage typically contains chlorite and amphibole in addition to serpentine.

Moses Rock (37.1081°N, 109.7841°W) peridotite xenoliths contain similar textures to Green Knobs peridotites and range from nearly anhydrous peridotites to fully hydrated assemblages (assemblages containing only hydrous phases with rare/absent relict grains, e.g. EMMR4). On average, Moses Rock xenoliths tend to have a greater abundance of hydrous minerals compared to Green Knobs, as McGetchin and Silver (1970, 1972) found spinel peridotite much less abundant than “serpentine schist.”

### Appendix A.2.1: Moses Rock

**MR-ATG-13** (Sample collected by Anna T. Gavasci)

**Mineralogy:** ol + opx + cpx + serpentine + Al-spinel

**Petrography**: Spinel lherzolite with large (>5mm) opx porphyroblasts. Olivine is fractured with serpentine commonly filling the fractures. Opx, cpx, and spinel are not fractured. Serpentine < 10% by mode.

**Location:** 37.1081°N, 109.7841°W

**EMMR4:**

**Mineralogy:** Serpentine + amphibole + chlorite + opaque

**Petrography:** Serpentinite. All primary silicate minerals have been reacted to serpentine, chlorite and/or amphibole; no relict grains are observed in thin section. However, relict grains were found in crushed mineral separates. Thin bands of opaque minerals (likely Cr-spinel) appear to define the grain boundaries of the serpentine and amphibole pseudomorphs. Chlorite clusters surround opaques. Fibrous amphibole grows irregularly in clusters, and along cleavages in pseudomorphous serpentine. Serpentine ~80% by mode, amphibole ~10%, chlorite ~5%,

**Location:** 37.1081°N, 109.7841°W

**EMMR25**

**Mineralogy:** Ol + opx + chlorite + cpx + amphibole + serpentine + opaque

**Petrography:** Hydrated lherzolite. ~1 cm clusters of chlorite surround opaques, most likely Cr-spinel. Prismatic amphibole grows along the grain boundaries of pyroxenes and rim chlorite clusters. Chlorite forms centimeter-scale clusters around spinel, but also is found intergrown with clinopyroxene. Olivine is fractured throughout the thin section, and these fractures are filled with serpentine.

**Location:** 37.1081°N, 109.7841°W

## Appendix A.2.2: Green Knobs

### EMGN2

**Mineralogy:** Ol + opx + cpx + Al-Spinel + serpentine

**Petrography:** Deformed equigranular spinel lherzolite. Grain boundaries are filled with very tiny, high birefringence grains. These small grains have optical properties consistent with olivine and pyroxene, but are too small to confirm. Olivines have undulose extinction and pyroxenes are kinked. Olivine is fractured, with fractures containing serpentine. Cpx is cloudy with inclusions too small to identify. Spinel is not opaque. Serpentine growth is limited to fractures and grain boundaries, making up less than 5% by mode.

**Location:** 35.9533° N, 109.0227° W

**EMGN6**

**Mineralogy:** Ol + opx + serpentine + amphibole + chlorite + cpx

**Petrography:** Hydrated equigranular peridotite. Amphibole forms twinned, prismatic prisms that incompletely replace pyroxenes. Amphibole tends to grow across grain boundaries as far as the cores of some grains, rather than forming rims. Amphibole commonly contains abundant opaque inclusions. Chlorite is limited to thin rims around opaque grains. Occasionally chlorite is found as inclusions within amphiboles. Serpentine occurs throughout the section as slender prismatic crystals, rimming chlorite, and included in amphibole, pyroxenes and olivine. Serpentine is sometimes intergrown with amphibole and chlorite. Olivine is replaced by serpentine heterogeneously-- some olivine grains have a small amount of serpentine in fractures, other grains are almost entirely replaced as serpentine replaces olivine along [010] cleavages. A vein, now filled with serpentine, cuts across the thin section. Serpentine 15% by mode, amphibole 15% by mode, chlorite 5% by mode.

**Location:** 35.9533° N, 109.0227° W

**EMGN9**

**Mineralogy:** Ol + opx  + chlorite + opaque + amphibole + serpentine

**Petrography:** Deformed, hydrated equigranular peridotite, containing very large (>8mm) chlorite clusters around opaques. Cpx was not found in thin section, and has most likely been reacted to amphibole. Cpx was found in mineral separates. Olivine [010] cleavages define a foliation in the peridotite. Amphibole grows in prismatic grains that replace pyroxenes. Serpentine grows across pyroxenes with fanning bunches of crystals. Serpentine forms irregular masses within olivines. Chlorite is ~20-25%, amphibole ~5%, serpentine is <5% by mode.

**Location:** 35.9533° N, 109.0227° W

**EMGN12**

**Mineralogy:** Ol + Opx + amphibole + chlorite + serpentine + opaque

**Petrography:** Hydrated equigranular peridotite. Olivines and opx form a mosaic texture, typical of mantle peridotites. Olivine is fractured and contains serpentine in the fractures. Amphibole replaces pyroxene. Chlorite forms clusters around opaques and is also found intergrown with amphibole. Chlorite ~10%, amphibole ~10%. serpentine ~ 1% by mode.

**Location:** 35.9533° N, 109.0227° W

**EMGN21**

**Mineralogy:** Ol + opx + chlorite + serpentine + opaque.

**Petrography:** Hydrated equigranular harzburgite.

Depleted HREE in EMGN21 cpx supports the idea that EMGN21 was a garnet peridotite before all garnet in the sample was reacted to chlorite.

Olivine displays [010] cleavage. The olivine cleavage fractures are filled with serpentine. Chlorite forms clusters, containing few opaques. Olivine and opx are commonly cut across by serpentine. Cpx was not found in thin section, but was found in mineral separates. Chlorite ~10% by mode, serpentine ~7% by mode.

**Location:** 35.9533° N, 109.0227° W

**EMGN24**

**Mineralogy:** Ol + opx + serpentine + amphibole + chlorite + opaques + clinohumite + carbonate

**Petrography:** Hydrated equigranular peridotite. Depleted HREE in EMGN24 cpx indicate that EMGN24 was garnet bearing prior to hydration. Chlorite clusters surround aggregates of small opaque grains. Chlorite clusters are small (~1400 μm), but are abundant in contrast to samples that have fewer, larger chlorite clusters (e.g., EMGN9). Chlorite and amphibole frequently grow within and surround opx. Cpx was not observed in thin section, but found in mineral separates. Dense intergrowth clusters of chlorite and amphibole may be a hydration product of Al-rich cpx. Serpentine rims chlorite clusters and forms slender crystals growing within and around pyroxenes and olivines. Carbonate is present as a long vein that cuts across the thin section.

Serpentine is ~15%, chlorite is ~10%, amphibole ~5%, clinohumite is <1% by mode.

**Location:** 35.9533° N, 109.0227° W

### EMGN27

**Mineralogy:** Ol + opx + serpentine + amphibole + carbonate + chlorite + cpx + opaques

**Petrography:** Hydrated equigranular harzburgite. Olivine displays [010] cleavage, made visible by thin fractures filled with serpentine. Serpentine also forms irregular-shaped clumps that grow within olivines. Chlorite thinly rims opaques (tens of microns thick). Prismatic amphibole can rarely be found replacing pyroxenes. Three carbonate grains in this section contain inclusions of silicate minerals, likely opx. Serpentine ~ 15% by mode, chlorite ~ 1%, amphibole ~1% by mode.

**Location:** 35.9533° N, 109.0227° W

### EMGN29

**Mineralogy:** Ol + opx + cpx + chlorite + amphibole + opaque + serpentine

**Petrography:** Lherzolite, modal olivine abundance (~50%) is similar to modal pyroxene abundance (~50%). EMGN29 has very little textural overprinting by hydrous mineral growth. Olivines have curved boundaries with pyroxenes, but with other olivines they have straight boundaries with 120° triple junctions. Olivines and pyroxenes may display undulose extinction. Finer sized cpx, amphibole and chlorite (~ 50 μm) are found at some junctions and grain boundaries. Cpx has two populations, larger (~1500 μm) grains similar in size to olivine and opx in the section, and small (~500 μm) grains that are found in the interstities of larger grains. Cpx (of both sizes) is frequently cloudy with inclusions. Chlorite surrounds opaque grains. Serpentine fills fractures in olivine. Serpentine, amphibole and chlorite make up ~ 1% of the sample by mode.

**Location:** 35.9533° N, 109.0227° W

**EMGN37**

**No thin section.**

**Location:** 35.9533° N, 109.0227°

**N16-GN**

**Mineralogy:** Ol + Al-spinel + cpx + opx + serpentine

**Petrology:** Equigranular spinel lherzolite. Olivines and pyroxenes show minor undulose extinction. Sample is close to textural equilibrium, containing many 120° triple junctions. Hydrous minerals are limited to grain boundaries and fractures. Serpentine is ~5% by mode.

**Previous studies also using this sample:** Smith and Levy, 1976; Roden et al., 1990; Roden and Shimizu, 1993; Smith, 2013; Behr and Smith, 2016**.**

**Location:** 35.9533° N, 109.0227° W

**N17-GN**

**Mineralogy:** Ol + opx + cpx + chlorite + serpentine + amphibole + opaque

**Petrology:** Equigranular lherzolite-harzburgite. Thin chlorite rims surround opaques. Larger Al-spinel grains have opaque rims with semi-transparent cores. Serpentine fills fractures and grain boundaries. Amphibole grows in grain boundaries around pyroxenes. Olivines and pyroxenes display kinking and undulose extinction. Chlorite ~1%, Amphibole <1%, serpentine <1% by mode.

**Previous studies also using this sample:** Smith and Levy, 1976; Smith, 1979; Roden and Shimizu, 1993; Smith, 2013.

**Location:** 35.9533° N, 109.0227° W

**N23-GN**

**Mineralogy:** Ol + opx + chlorite + cpx + amphibole + clinohumite + opaque

**Petrography:** Hydrated lherzolite. Chlorite forms round clusters that are rimmed with amphibole, but contain no opaques. The clusters make up ~10% of the sample. Roden et al. (1990) interpreted N23-GN to be a garnet peridotite prior to hydration, based on HREE depletions in cpx and the similarity of the shape of the chlorite clusters to garnets. Cpx is noticeably exsolved and is often rimmed with fine grained amphibole and chlorite. Chlorite ~ 25%, amphibole ~ 10% by mode.

**Previous studies also using this sample:** Smith, 1979; Roden et al., 1990; Roden and Shimizu, 1993; Smith, 2013.

**Location:** 35.9533° N, 109.0227° W

**N53-GN**

**Mineralogy:** Ol + opx + cpx + Al-spinel + serp

**Petrology:** Equigranular spinel lherzolite. Sample is close to textural equilibrium, containing many 120° triple junctions. In parts of the thin section, linear fractures containing fine grained, unidentified material cut across the sample. Serpentine fills thin cracks and grain boundaries, making up <1% by mode.

**Previous studies also using this sample:** Smith and Levy, 1976; Roden and Shimizu, 1993; Smith, 2013.

**Location:** 35.9533° N, 109.0227° W

**N55-GN**

**Mineralogy:** Ol + opx + cpx + sp + amph + serpentine + gar + serp

**Petrology:** Spinel-garnet lherzolite. Garnet rims spinel in irregularly thick rims. In places, clusters of neoblastic olivine, amphibole and chlorite occur at grain junctions. Amphibole grows around cpx, forming thin or partial rims of nucleating amphibole grains. Amphibole ~1% by mode.

**Previous studies also using this sample:** Smith and Levy, 1976; Smith, 1979.

**Location:** 35.9533° N, 109.0227° W

### N61-GN

**Mineralogy:** Ol + opx + cpx + Al-spinel +amph

**Petrology:** Equigranular spinel lherzolite. Similar to N53-GN, fractures cut across the sample containing unidentified, fine grained material. Unlike N53-GN, fine grained material can also be found at grain boundaries throughout the sample. Amphibole appears in a small cluster. Amphibole <1% by mode.

**Previous studies also using this sample:** Smith and Levy, 1976; Roden et al., 1990; Roden and Shimizu, 1993.

**Location:** 35.9533° N, 109.0227° W

### N106-GN

**Mineralogy:** Ol + opx + cpx + chlorite + amphibole + opaques

**Petrology:** Hydrated lherzolite. Chlorite surrounds opaque grains. Fine grained amphibole surrounds cpx grains. Cpx is cloudy with inclusions. Cpx and opx are both intergrown with amphibole in places. One olivine porphyroblast is unusually long, almost 1cm in length. Garnet rims around spinel were reported in an informal description, but could not be confirmed (personal communication, D. Smith). Chlorite ~1%, amphibole ~10% by mode.

**Location:** 35.9533° N, 109.0227° W

**N126-GN**

**Mineralogy:** Ol + opx + cpx + Al-spinel + serpentine

**Petrology:** Spinel lherzolite. Sample is close to textural equilibrium, containing many 120° triple junctions. Olivines display undulose extinction. Evidence of hydration is limited to serpentine that fills thin fractures and grain boundaries. Serpentine <1% by mode. The rock has distinctive intergrowths of spinel and pyroxene, interpreted by Smith (1977) as products of garnet-olivine reaction.

**Previous studies also using this sample:** Smith, 1977.

**Location:** 35.9533° N, 109.0227° W

**N178-GN**

**Mineralogy:** Ol + opx + cpx + chlorite + Cr-spinel + phlogopite (trace)

**Petrology:** Deformed harzburgite. N178-GN is strongly foliated. Kinking of opx and olivine is found in almost all grains. Spinel is absent. Chlorite is present, but does not form clusters. Chlorite ~5% by mode.

**Previous studies also using this sample:** Smith, 2010; Smith, 2013.

**Location:** 35.9533° N, 109.0227° W

# APPENDIX A.3: WHOLE ROCK MAJOR AND TRACE ELEMENT COMPOSITIONS

**Table A2: Whole Rock major and trace elements**

| Sample | MR-ATG-13 | EMGN2 | N61-GN | EMGN24 | N16-GN | N126-GN | N17-GN | N55-GN | EMGN21 | N178-GN |  | N106-GN | EMGN27 |
|---|---|---|---|---|---|---|---|---|---|---|---|---|---|
|  |  |  |  |  |  |  |  |  |  | n = 3 | **2σ** |  |  |
| **SiO2** | 43.82 | 44.76 | 44.68 | 43.45 | 40.62 | 45.00 | 45.61 | 43.19 | 43.37 | 43.22 | (0.92) | 45.21 | 42.02 |
| **TiO2** | 0.02 | 0.04 | 0.09 | 0.10 | 0.03 | 0.02 | 0.01 | 0.01 | 0.00 | 0.00 | (0.00) | 0.06 | 0.00 |
| **Al2O3** | 1.98 | 2.73 | 2.71 | 2.54 | 2.12 | 2.54 | 2.00 | 1.91 | 0.96 | 0.81 | (0.33) | 3.67 | 0.98 |
| **Cr2O3** | 0.47 | 0.24 | 0.37 | 0.35 | 0.35 | 0.37 | 0.42 | 0.34 | 0.23 | 0.30 | (0.14) | 0.47 | 0.27 |
| **FeO** | 7.65 | 7.60 | 8.12 | 7.24 | 10.15 | 7.79 | 7.27 | 8.18 | 7.15 | 7.04 | (0.22) | 7.71 | 6.74 |
| **MnO** | 0.12 | 0.12 | 0.12 | 0.11 | 0.14 | 0.12 | 0.12 | 0.12 | 0.13 | 0.11 | (0.00) | 0.13 | 0.11 |
| **MgO** | 40.27 | 39.01 | 39.88 | 35.59 | 42.99 | 39.11 | 40.93 | 42.37 | 42.33 | 44.89 | (1.93) | 37.80 | 41.53 |
| **CaO** | 1.60 | 2.60 | 2.42 | 3.15 | 1.50 | 2.40 | 1.86 | 2.35 | 1.11 | 0.55 | (0.35) | 3.25 | 0.57 |
| **Na2O** | 0.05 | 0.27 | 0.24 | 0.30 | 0.07 | 0.14 | 0.13 | 0.21 | 0.02 | 0.02 | (0.00) | 0.36 | 0.03 |
| **K2O** | 0.01 | 0.02 | 0.00 | 0.04 | 0.01 | 0.00 | 0.01 | 0.02 | 0.01 | 0.00 | (0.00) | 0.01 | 0.02 |
| **NiO** | 0.29 | 0.21 | 0.26 | 0.20 | 0.36 | 0.27 | 0.27 | 0.31 | 0.24 | 0.32 | (0.03) | 0.25 | 0.23 |
| **P2O5** | 0.00 | 0.00 | 0.01 | 0.00 | 0.01 | 0.01 | 0.00 | 0.00 | 0.00 | 0.00 | (0.00) | 0.01 | 0.00 |
| **LOI** | 3.77 | 1.31 | 0.90 | 6.08 | 1.64 | 2.42 | 1.67 | 1.21 | 4.38 | 2.97 | (0.24) | 1.15 | 6.78 |
| **Total** | 100.05 | 98.92 | 99.81 | 99.15 | 100.00 | 100.18 | 100.31 | 100.25 | 99.92 | 100.24 |  | 100.07 | 99.29 |
|  |  |  |  |  |  |  |  |  |  |  |  |  |  |
| **La** | 0.03 | 0.19 | 0.18 | 0.19 | 0.11 | 0.05 | 0.16 | 0.38 | 0.19 | 0.14 | (0.06) | 0.11 | 0.06 |
| **Ce** | 0.06 | 0.30 | 0.58 | 0.44 | 0.22 | 0.11 | 0.23 | 0.56 | 0.32 | 0.35 | (0.16) | 0.16 | 0.07 |
| **Pr** | 0.01 | 0.04 | 0.12 | 0.07 | 0.06 | 0.01 | 0.03 | 0.06 | 0.04 | 0.04 | (0.02) | 0.02 | 0.01 |
| **Nd** | 0.04 | 0.15 | 0.63 | 0.36 | 0.18 | 0.04 | 0.08 | 0.16 | 0.16 | 0.17 | (0.09) | 0.15 | 0.03 |
| **Sm** | 0.01 | 0.05 | 0.24 | 0.17 | 0.09 | 0.03 | 0.02 | 0.03 | 0.04 | 0.03 | (0.01) | 0.13 | 0.00 |
| **Eu** | 0.01 | 0.03 | 0.10 | 0.07 | 0.04 | 0.01 | 0.00 | 0.01 | 0.01 | 0.01 | (0.01) | 0.06 | 0.00 |
| **Gd** | 0.03 | 0.15 | 0.27 | 0.26 | 0.15 | 0.07 | 0.02 | 0.06 | 0.03 | 0.02 | (0.01) | 0.23 | 0.00 |
| **Tb** | 0.01 | 0.04 | 0.05 | 0.05 | 0.03 | 0.02 | 0.01 | 0.02 | 0.00 | 0.00 | (0.00) | 0.05 | 0.00 |
| **Dy** | 0.08 | 0.27 | 0.31 | 0.33 | 0.23 | 0.19 | 0.06 | 0.14 | 0.03 | 0.01 | (0.01) | 0.40 | 0.00 |
| **Ho** | 0.02 | 0.07 | 0.07 | 0.07 | 0.06 | 0.05 | 0.02 | 0.04 | 0.01 | 0.00 | (0.00) | 0.09 | 0.00 |
| **Er** | 0.07 | 0.20 | 0.17 | 0.19 | 0.17 | 0.15 | 0.07 | 0.12 | 0.03 | 0.02 | (0.01) | 0.29 | 0.00 |
| **Tm** | 0.01 | 0.03 | 0.03 | 0.03 | 0.02 | 0.03 | 0.01 | 0.02 | 0.01 | 0.00 | (0.00) | 0.04 | 0.00 |
| **Yb** | 0.11 | 0.22 | 0.17 | 0.19 | 0.16 | 0.18 | 0.09 | 0.14 | 0.04 | 0.02 | (0.01) | 0.30 | 0.01 |
| **Lu** | 0.02 | 0.04 | 0.03 | 0.03 | 0.03 | 0.03 | 0.01 | 0.02 | 0.01 | 0.00 | (0.00) | 0.05 | 0.00 |
| **Rb** | 0.09 | 0.34 | 0.34 | 0.10 | 0.65 | 0.11 | 0.22 | 0.30 | 0.14 | 0.23 | (0.04) | 0.11 | 0.49 |
| **Pb** | 0.07 | 0.46 | 0.39 | 0.10 | 0.25 | 0.11 | 0.59 | 1.54 | 0.32 | 0.19 | (0.06) | 0.65 | 0.23 |
| **Th** | 0.01 | 0.03 | 0.02 | 0.01 | 0.04 | 0.01 | 0.03 | 0.03 | 0.06 | 0.02 | (0.01) | 0.01 | 0.02 |
| **U** | 0.20 | 0.02 | 0.01 | 0.01 | 0.01 | 0.00 | 0.01 | 0.03 | 0.01 | 0.01 | (0.00) | 0.01 | 0.01 |
| **Nb** | 0.02 | 0.06 | 0.05 | 0.04 | 0.06 | 0.03 | 0.06 | 0.72 | 0.14 | 0.03 | (0.01) | 0.02 | 0.00 |
| **Sr** | 34.14 | 28.17 | 19.97 | 22.93 | 7.96 | 11.60 | 19.84 | 26.75 | 11.91 | 14.71 | (6.41) | 16.60 | 7.74 |
| **Zr** | 0.34 | 0.57 | 1.56 | 0.27 | 1.20 | 0.39 | 0.53 | 0.36 | 0.30 | 0.33 | (0.21) | 1.18 | 0.39 |
| **Hf** | 0.01 | 0.03 | 0.03 | 0.01 | 0.05 | 0.01 | 0.01 | 0.01 | 0.01 | 0.01 | (0.00) | 0.05 | 0.01 |
| **Y** | 0.56 | 1.76 | 1.63 | 0.19 | 1.44 | 1.23 | 0.48 | 0.97 | 0.22 | 0.10 | (0.05) | 2.37 | 0.31 |
| **Sc** | 11.69 | 12.61 | 11.77 | 7.94 | 7.63 | 11.97 | 11.33 | 10.90 | 7.30 | 7.42 | (2.36) | 13.95 | 9.74 |
| **V** | 56.46 | 60.74 | 63.28 | 73.44 | 37.68 | 57.98 | 57.29 | 48.43 | 33.99 | 25.81 | (9.15) | 73.32 | 28.12 |

Table A2: Whole Rock major and trace elements

| Sample | N23-GN | EMGN12 | EMMR4 | EMMR25 | EMGN6 | EMGN29 | EMGN9 | N17-GN | EMGN37 | BHVO-2 | |
|---|---|---|---|---|---|---|---|---|---|---|---|
| | | | | | | | | | | | published |
| **SiO2** | 42.64 | 43.25 | 44.04 | 44.95 | 44.53 | 46.04 | 43.58 | 45.61 | 40.52 | 49.88 | 49.90 |
| **TiO2** | 0.07 | 0.01 | 0.02 | 0.05 | 0.02 | 0.01 | 0.02 | 0.01 | 0.00 | 2.76 | 2.73 |
| **Al2O3** | 4.45 | 1.72 | 2.00 | 3.60 | 2.42 | 2.51 | 2.20 | 2.00 | 0.41 | 13.61 | 13.50 |
| **Cr2O3** | 0.28 | 0.35 | 0.47 | 0.52 | 0.38 | 0.45 | 0.41 | 0.00 | 0.44 | 0.04 | 0.04 |
| **FeO** | 7.37 | 7.18 | 6.71 | 7.60 | 6.77 | 7.14 | 7.28 | 7.27 | 7.18 | 11.18 | 11.07 |
| **MnO** | 0.11 | 0.12 | 0.05 | 0.07 | 0.11 | 0.12 | 0.12 | 0.12 | 0.12 | 0.17 | 0.17 |
| **MgO** | 36.69 | 40.21 | 32.52 | 29.85 | 36.76 | 37.76 | 38.77 | 40.93 | 44.44 | 7.30 | 7.23 |
| **CaO** | 2.46 | 1.71 | 1.66 | 2.95 | 2.67 | 2.20 | 2.07 | 1.86 | 0.33 | 11.42 | 11.40 |
| **Na2O** | 0.46 | 0.15 | 0.28 | 0.24 | 0.35 | 0.10 | 0.25 | 0.13 | 0.00 | 2.23 | 2.22 |
| **K2O** | 0.07 | 0.01 | 0.09 | 0.10 | 0.04 | 0.01 | 0.05 | 0.01 | 0.00 | 0.52 | 0.52 |
| **NiO** | 0.19 | 0.29 | 0.28 | 0.29 | 0.24 | 0.24 | 0.26 | 0.00 | 0.31 | 0.01 | 0.02 |
| **P2O5** | 0.05 | 0.00 | 0.00 | 0.00 | 0.00 | 0.00 | 0.00 | 0.00 | 0.00 | 0.26 | 0.27 |
| **LOI** | 5.12 | 4.77 | 11.40 | 8.76 | 5.47 | 2.90 | 4.52 | 1.67 | 5.82 | 0.00 | 0.00 |
| **Total** | 99.96 | 99.76 | 99.52 | 98.98 | 99.76 | 99.47 | 99.52 | 99.62 | 99.59 | 99.37 | 99.06 |
| | | | | | | | | | | | |
| **La** | 0.71 | 0.05 | 0.08 | 0.19 | 0.18 | 0.09 | 0.16 | 0.16 | 0.11 | 15.29 | 15.20 |
| **Ce** | 0.84 | 0.10 | 0.13 | 0.36 | 0.37 | 0.11 | 0.29 | 0.23 | 0.14 | 36.95 | 37.50 |
| **Pr** | 0.10 | 0.01 | 0.01 | 0.04 | 0.04 | 0.01 | 0.04 | 0.03 | 0.01 | 5.26 | 5.29 |
| **Nd** | 0.42 | 0.04 | 0.04 | 0.19 | 0.17 | 0.02 | 0.15 | 0.08 | 0.03 | 24.14 | 24.50 |
| **Sm** | 0.19 | 0.01 | 0.02 | 0.10 | 0.03 | 0.00 | 0.03 | 0.02 | 0.01 | 6.41 | 6.07 |
| **Eu** | 0.08 | 0.00 | 0.01 | 0.04 | 0.01 | 0.00 | 0.02 | 0.00 | 0.00 | 2.19 | 2.07 |
| **Gd** | 0.31 | 0.02 | 0.04 | 0.17 | 0.06 | 0.02 | 0.07 | 0.02 | 0.01 | 6.42 | 6.24 |
| **Tb** | 0.07 | 0.01 | 0.01 | 0.04 | 0.01 | 0.01 | 0.01 | 0.01 | 0.00 | 1.02 | 0.94 |
| **Dy** | 0.48 | 0.07 | 0.07 | 0.31 | 0.11 | 0.08 | 0.15 | 0.06 | 0.01 | 5.68 | 5.31 |
| **Ho** | 0.11 | 0.02 | 0.02 | 0.08 | 0.03 | 0.02 | 0.04 | 0.02 | 0.00 | 1.05 | 0.97 |
| **Er** | 0.33 | 0.07 | 0.06 | 0.24 | 0.11 | 0.08 | 0.12 | 0.07 | 0.01 | 2.61 | 2.54 |
| **Tm** | 0.05 | 0.01 | 0.01 | 0.04 | 0.02 | 0.01 | 0.02 | 0.01 | 0.00 | 0.35 | 0.34 |
| **Yb** | 0.30 | 0.09 | 0.06 | 0.24 | 0.14 | 0.11 | 0.14 | 0.09 | 0.01 | 1.94 | 2.00 |
| **Lu** | 0.05 | 0.01 | 0.01 | 0.04 | 0.02 | 0.02 | 0.02 | 0.01 | 0.00 | 0.28 | 0.27 |
| **Rb** | 0.30 | 0.17 | 0.73 | 1.03 | 0.35 | 0.23 | 0.46 | 0.22 | 0.40 | 8.94 | 9.08 |
| **Pb** | 1.62 | 0.43 | 1.90 | 0.94 | 0.61 | 0.20 | 0.62 | 0.59 | 0.40 | 1.60 | 1.40 |
| **Th** | 0.05 | 0.02 | 0.00 | 0.03 | 0.02 | 0.01 | 0.02 | 0.03 | 0.01 | 1.24 | 1.18 |
| **U** | 0.03 | 0.00 | 3.99 | 3.70 | 0.02 | 0.03 | 0.03 | 0.01 | 0.01 | 0.42 | 0.44 |
| **Nb** | 0.29 | 0.02 | 0.03 | 0.09 | 0.12 | 0.01 | 0.07 | 0.06 | 0.06 | 16.80 | 16.40 |
| **Sr** | 117.00 | 13.82 | 50.93 | 118.99 | 19.56 | 17.36 | 20.88 | 19.84 | 10.52 | 394.86 | 396.00 |
| **Zr** | 1.73 | 0.36 | 0.13 | 0.71 | 0.74 | 0.31 | 0.51 | 0.53 | 0.28 | 166.20 | 160.00 |
| **Hf** | 0.07 | 0.01 | 0.01 | 0.03 | 0.02 | 0.00 | 0.01 | 0.01 | 0.01 | 4.42 | 4.10 |
| **Y** | 2.79 | 0.52 | 0.49 | 2.07 | 0.89 | 0.59 | 0.92 | 0.48 | 0.06 | 25.60 | 23.00 |
| **Sc** | 14.33 | 9.95 | 10.17 | 14.80 | 13.32 | 12.69 | 11.57 | 11.33 | 4.85 | 31.86 | 31.00 |
| **V** | 75.92 | 47.91 | 64.72 | 89.63 | 58.94 | 66.48 | 54.46 | 57.29 | 21.67 | 312.47 | 317.00 |

## APPENDIX A.4 OSMIUM ISOTOPE COMPOSITIONS

**Table A3: Whole rock Osmium isotope compositions.**

| | 187Re/188Os | 187Os/188Os | Os | Re | Whole Rock $Al_2O_3$ |
|---|---|---|---|---|---|
| **EMMR25*** | 0.24 | 0.1287(2) | 2.98 | 0.15 | 3.60 |
| **EMMR04** | 1.82 | 0.12053(4) | 4.99 | 1.92 | 2.00 |
| **EMGN6** | 0.65 | 0.12704(3) | 3.57 | 0.49 | 2.42 |
| **EMGN6*** | 0.33 | 0.12672(5) | 5.20 | 0.37 | 2.42 |
| **EMGN37** | 9.84 | 0.1140(1) | 0.76 | 1.59 | 0.41 |
| **EMGN2** | 0.27 | 0.12556(2) | 3.62 | 0.21 | 2.73 |
| **EMGN24** | 0.49 | 0.1260(3) | 3.89 | 0.40 | 2.54 |
| **EMGN9** | *nd* | 0.12611(3) | 3.44 | *nd* | 2.20 |
| **EMGN9*** | 0.15 | 0.1256(5) | 3.14 | 0.10 | 2.20 |
| **N23-GN** | 0.37 | 0.1272(2) | 3.31 | 0.26 | 4.45 |
| **N178-GN** | 0.27 | 0.1188(10) | 2.97 | 0.17 | 0.81 |
| **N178-GN*** | 0.08 | 0.11521(6) | 2.70 | 0.04 | 0.81 |
| **EMGN27** | 0.22 | 0.1171(5) | 2.88 | 0.13 | 0.98 |
| **EMGN27*** | 8.11 | 0.11596(7) | 4.65 | 8.00 | 0.98 |
| **EMGN29** | *nd* | 0.12663(3) | 3.27 | *nd* | 2.51 |
| **EMGN12** | 0.19 | 0.12428(5) | 4.46 | 0.17 | 1.72 |

*: Sample digested at University of Bonn; *nd*: not determined

## APPENDIX A.5 NEODYMIUM ISOTOPE COMPOSITIONS

**Table A4: Sm-Nd isotope analyses**

| | **First Round (soft leach)** | | | | **Second Round (hard leach)** | | | |
|---|---|---|---|---|---|---|---|---|
| | **Sm (ppm)** | **Nd (ppm)** | **147Sm/144Nd** | **143Nd/144Nd** | **Sm (ppm)** | **Nd (ppm)** | **147Sm/144Nd** | **143Nd/144Nd** |
| **MR-ATG-13** | 0.215(1) | 0.199(1) | 0.6541(35) | 0.517359(44) | | | | |
| **EMGN2** | 0.383(1) | 0.669(3) | 0.3462(19) | 0.514290(3) | 0.252(2) | 0.654(5) | 0.2335(25) | 0.514291(28) |
| **EMGN21** | 0.313(1) | 1.468(6) | 0.1288(7) | 0.512474(4) | | | | |
| **EMGN24** | 0.933(3) | 2.232(9) | 0.2530(14) | 0.513432(2) | | | | |
| **N16-GN**[1] | *0.886* | *1.28* | *0.4180(42)* | *0.514800(60)* | | | | |
| **N17-GN** | 0.0230(1) | 0.154(1) | 0.0921(5) | 0.513172(5) | 0.0193(1) | 0.106(1) | 0.1103(12) | 0.513320(10) |
| **N55-GN** | 0.184(1) | 0.975(4) | 0.1143(6) | 0.512586(8) | | | | |
| **N61-GN**[1] | *1.42* | *3.89* | *0.2210(22)* | *0.513102(25)* | | | | |
| **N106-GN** | | | | | 0.550(4) | 0.719(6) | 0.4624(49) | 0.515414(5) |
| **N126-GN** | 0.1050(3) | 0.0270(1) | 2.3569(126) | 0.533395(14) | 0.189(1) | 0.0469(3) | 2.4298(259) | 0.533356(28) |
| **N178-GN** | 0.497(2) | 3.729(15) | 0.0805(4) | 0.512889(7) | | | | |
| **N53-GN** | | | | | 0.401(3) | 0.292(2) | 0.8300(88) | 0.518925(13) |

[1] : Roden, Smith and Murthy, (1990)

All concentrations determined via isotope dilution, errors are 2σ

## APPENDIX A.6 SUPPLEMENTARY METHODS FOR CHAPTER 2

### Appendix A.6.1: Sample Selection

Peridotite xenoliths were collected from Green Knobs and Moses Rock in 2014. The collected peridotite xenoliths varied in size, texture, mineralogy and hydrous mineral abundance. We selected ~45 xenoliths that spanned this observed variability for further analysis. Additional samples that had been previously characterized were selected from the collection of Dr. Douglas Smith at The University of Texas at Austin. A small portion of each xenolith was crushed and 2-3 clinopyroxenes from each sample were mounted and analyzed by Electron Probe MicroAnalyzer (EPMA) to survey mineral major element variations. Based on these preliminary analyses, a suite of ~25 xenoliths were chosen for further study that span the observed range of compositions and textures.

### Appendix A.6.2: Whole Rock Major and Trace Element Analyses

Analysis of major and trace elements in whole rock powders were performed at Washington State University GeoAnalytical Labs following the procedures of Johnson et al. (1999). For each sample, 5 to 10 grams of rock was powdered in a tungsten carbide (WC) swingmill at WSU. Whole rock major elements were determined via X-Ray Fluorescence (XRF), and trace element concentrations were determined via solution ICP-MS. Two powder duplicates, two grinding media duplicates, and BHVO-2 were all analyzed to test reproducibility and constrain potential contamination of the grinding media.

Tungsten carbide (WC) is commonly used for grinding samples in preparation for geochemical analysis because WC does not contaminate major elements. However, Hickson and Juras (1986) have suggested that WC may contaminate high field strength elements (HFSE, e.g., Ta, Nb). To test for possible HFSE contamination, separate splits from two samples (EMGN2 and EMGN23) were ground in WC and in agate for comparison. Ta concentrations were higher in the WC-ground powders for both samples, but were close to the detection limit. We did not observe a systematic increase in Nb in the WC-prepared powders or any other systematic differences for elements above detection limits.

Replicates of XRF powder splits are reproducible to better than 1% for elements with abundances greater than 5 wt% (Si, Fe, Mg), varied less than 5% for elements with concentrations between than 0.1 wt% and 5 wt% (Al, Cr, Mn, Ca, Na, Ni), and varied less than 10% for Ti (usually <0.1 wt%). Duplicate ICP-MS analyses varied within 5% for elements with abundances higher than 1ppm, and varied within 25% for concentrations less than 1 ppm. Analyzed replicates of BHVO-2 (See Appendix 1.3) were within the published 2σ compositional variation of the standard.

### Appendix A.6.3: Clinopyroxene Major Element Analyses

Clinopyroxene major elements were analyzed on a JEOL JXA-8200 EPMA at the University of Texas at Austin. EPMA analyses used a 20 nA beam current, 15 kV accelerating voltage, and a 10 μm defocussed beam. Count times were 30-40 s on peak and 15-20 s off peak, with shorter count times for more abundant elements. Precision of repeated analysis on secondary standard NMNH Cr-Augite 164905 (see Appendix 1.1) for a given element is inversely correlated with that element's concentration. Reproducibility for elements with concentrations greater than 1 wt. % was better than 5%, and better than 12% for elements with concentrations less than 1 wt. %. Averaged analyses of NMNH Cr Augite were within 5% of the standard composition, except for Mn (within 12%) (Jarosewich et al., 1980). However because Al was calibrated using the Cr-Augite standard, NMNH Kakanui Hornblende 143965 was used as a secondary standard for this element. Reproducibility for Al on the Kakanui Hornblende standard was better than 2%. Probe analyses of the same cpx grain show similar reproducibility to the Cr-Augite standard for all elements except Ti, which has significantly worse reproducibility (141%) due to extremely low Ti concentration (<1000ppm) in most samples. Because Ti concentration by LA-ICP-MS has better reproducibility than the EPMA (1.5% on glass standards, 8% on grain duplicates) and because there is a 1:1 correlation between the EPMA and LA-ICP-MS datasets, we use Ti concentration data measured in clinopyroxene by LA-ICP-MS in place of data measured by EPMA. Clinopyroxenes in samples with chlorite growth typically display $Al_2O_3$ depletion in the edges of grains. Data presented in Appendix 1.1 are average analyses of 4-5 cpx grain interiors from each sample. Previously published EPMA clinopyroxene analyses for two of the samples are available in Appendix 1.1 for comparison with our results.

## Appendix A.6.4: Clinopyroxene Trace Element Analyses

Clinopyroxene trace elements concentrations were measured via LA-ICP-MS using a New Wave UP-193FX laser system coupled to an Agilent 7500Ce quadrupole instrument at the University of Texas at Austin. The maximum spot size of 150 μm was used to achieve maximum signal intensity due to the low concentrations present for many trace elements. All spots were pre-ablated before analysis. Each individual laser ablation analysis consisted of a 40 sec gas blank followed by 60 sec laser dwell time. The laser wavelength was 193nm and had a 10 Hz firing rate. Ablated material was transported with a He sweep gas flow rate of 700 mL per min and Ar carrier gas flow rate of 650 mL per min. NIST 612 was used as the primary standard. Repeat analyses of the BCR-2G secondary standard are reproducible within 5% of the published composition, except for Pb, Hf, Gd, and Y which were reproduced within 8% of the published composition. Interior-to-edge variability is found in most Group T clinopyroxenes and in some Group D clinopyroxenes. In these samples, Sr and LREE concentration increases towards the edge of the grain. Typically, interiors of 4-5 clinopyroxene grains were analyzed per sample, using the same spots analyzed previously by EPMA. Data reported in Appendix 1.1 are the average composition of these multiple grain interior analyses. In samples that do not contain interior-to-edge variation, clinopyroxene trace element concentrations from multiple grains are usually within 10%. In samples that do contain interior-to-edge variation, cpx trace element concentrations between multiple grains vary within the range of measured interior-to-edge variability.

### Appendix A.6.5: Sm-Nd Isotope Analyses

Sm-Nd isotopes were measured on ~50 to ~200 mg of hand-picked cpx separates. Before digestion, the separates were either leached for 20 min in 2.5 N HCl at 60°C (soft leach) or for 1 hour in 6 N HCl at 90°C (hard leach). Samples were spiked with a $^{149}$Sm-$^{150}$Nd mixed spike. The dissolution and chemical extraction procedures followed the procedures of Connelly et al. (2006). Following sample dissolution in HF:$HNO_3$, Nd and Sm were extracted via column chemistry using AG50W-X8 and HDEHP resins. Sm and Nd were loaded onto double Re filaments, and analyzed as metal ions on a Triton TIMS at the University of Texas at Austin. The full Nd procedural blank was less than 30 pg, and the full Sm procedural blank was less than 2.5 pg. The average $^{143}$Nd/$^{144}$Nd value obtained at UT Austin for the AMES Nd standard during the period of this study was 0.512088±0.000013 (2σ), slightly higher than the value of Scher and Delaney (2010), 0.512069 ±0.000014. Similarly, the average composition of rock standard USGS BCR-2 measured during the same period was 0.512656±0.000014(2σ), slightly higher than the published composition of 0.512633 ±0.000007 (2σ) (Raczek et al., 2001). In order to eliminate inter-laboratory bias, the data have been adjusted by 0.000002, correcting to the published compositions of AMES and BCR-2 standards.

Clinopyroxene grains from hydrated xenolith assemblages usually contain fractures filled with hydrous minerals (e.g., chlorite, serpentine, amphibole) and often contain~~s~~ oxide and silicate inclusions. Most clinopyroxenes have a cloudy appearance and are not optically clear. As a result, completely optically pure separates could not be obtained. In addition, Group T cpx display LREE enriched rims, as observed in LA-ICP-

MS core-to-rim profiles. This zoning may have affected Nd isotopes and Sm/Nd ratios in the rims relative to the cores. To constrain the influence of hydrous phases and LREE enrichment in the rims we analyzed duplicate cpx splits from three samples using two different leaching procedures. Nd isotope analyses using the two different procedures were reproducible within error for two samples. Nd isotopes for a third sample were higher by 2.89 epsilon units in the hard leach, but this split also had higher measured Sm/Nd, consistent with increased removal of the LREE-enriched rim component through the hard leach. Measured Sm/Nd compositions were variable in the different splits, but were not consistently higher in the hard leached splits relative to the soft leached splits. Variability in measured Sm/Nd and Nd isotope composition between different mineral splits from the same sample likely reflects in part differing abundances of inclusions in the separate splits. Despite this variability, isochron ages calculated from the Group D soft leach and hard leach samples yield similar ages (soft leach: 1.45 ±0.04 Ga, n=5; hard leach: 1.39 ±0.2 Ga, n=3). The Sm-Nd data are listed in Appendix 1.5 for both soft and hard leach analyses. In Figure 3 and for calculation of the Group D isochron, we average the hard and soft leach data for each sample. The reported error is either the internal standard error of the measurement (2 SE) or two times the external standard error of the duplicates, whichever is greater.

### Appendix A.6.6: Rhenium-Osmium Isotope Analyses

Re and Os were isolated from whole rock powders following the method of Byerly and Lassiter (2012). Most Re-Os digestions were performed at UT Austin. The

Jackson School of Geosciences building at UT Austin was closed for renovations during the summer of 2015. A subset of samples was digested at the University of Bonn, Germany during the building closure. The digestion procedure at University of Bonn is similar to the procedure at UT Austin, except solvent extraction used chloroform instead of carbon tetrachloride. Rind-free chips of the xenoliths were cut with a water saw, and saw marks were removed with SiC sand paper. Chips were then ground to a fine powder in an alumina ball mill. Small amounts (~1.5-3 g) of powder were prepared in order to preserve as much of the xenoliths as possible for further analyses. As a result, intra-sample heterogeneity may not be fully homogenized by the small powder splits that were prepared. Separate chips were powdered for digestion at UT Austin and the University of Bonn. Approximately 1.5 g of whole rock powders were put in quartz pressure vessels, spiked with a $^{185}$Re-$^{190}$Os mixed spike and then reacted in reverse aqua regia in a *Anton-Paar* High-Pressure Asher (at 105 bar and 300°C). Osmium was extracted from the aqua regia using $CCl_4$, and then back-extracted into HBr. The Os was purified further using microdistillation (Birck et al., 1997). Rhenium was separated from the aqua regia using anion exchange columns. Finally, Os was loaded onto Pt filaments, as described in Chatterjee and Lassiter (2015), and analyzed in negative ion mode (N-TIMS) as $OsO_3^-$ on the Triton TIMS at UT Austin. Re was analyzed via solution MC-ICP-MS using the Micromass Isoprobe at UT-Austin, and on a Thermo Scientific Element XR SF-ICP-MS at University of Bonn. Total procedural Os blanks were <1pg at UT Austin and <2 pg at the University of Bonn. Re blanks were <5 pg. The average $^{187}$Os/$^{188}$Os ratio of the

Johnson-Matthey Os standard run during the period of this study was 0.113832 ±0.000006.

Osmium isotopes and Os concentration in replicate analyses (powders from separate xenolith chips) show greater variability than can be accounted for by analytical error. This may reflect variable sampling of different sulfide populations in the different xenolith splits and thus reflects intra-sample heterogeneity. From petrographic observation, many peridotite xenoliths from Green Knobs and Moses Rock contain abundant sulfides both as inclusions in silicate phases and along grain boundaries. In addition, EDS imaging of thin sections revealed the occasional presence of rare PGE alloy and PGE-sulfide grains, including a Ru-Rh-Ir alloy grain and PtS. Several analyses produced high Re concentrations (not quantitatively determined due to underspiking), which may have resulted from inclusion of Re-rich "nuggets". Despite the intra-sample heterogeneity, whole rock $Al_2O_3$ and $^{187}Os/^{188}Os$ are well correlated. For Figure 2, we report the average of replicate analyses. The reported error is either the internal standard error of the measurement (2 SE) or two times the external standard error of the replicates, whichever is greater. The data for all Re-Os replicate analyses can be found in Appendix 1.4.

# APPENDIX A.7: SUPPLEMENTARY PLOTS FOR CHAPTER 2

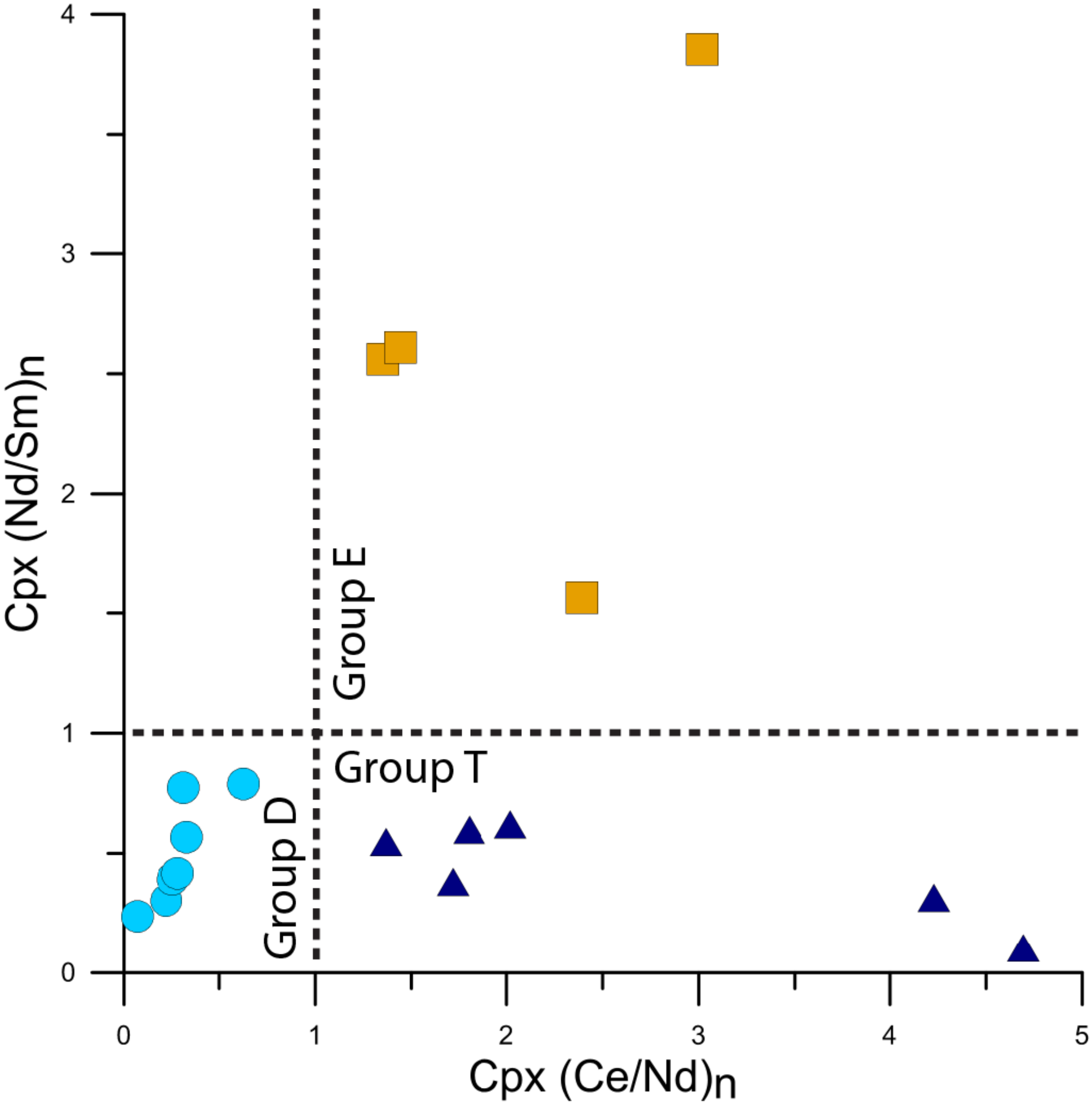

Figure A.1: Groups are defined based on the slope of their REE patterns around Nd. These slopes can be quantified using the ratio of lanthanides with similar incompatibility to Nd. See Figures A1.7.2 to A1.7.4 for individual patterns.

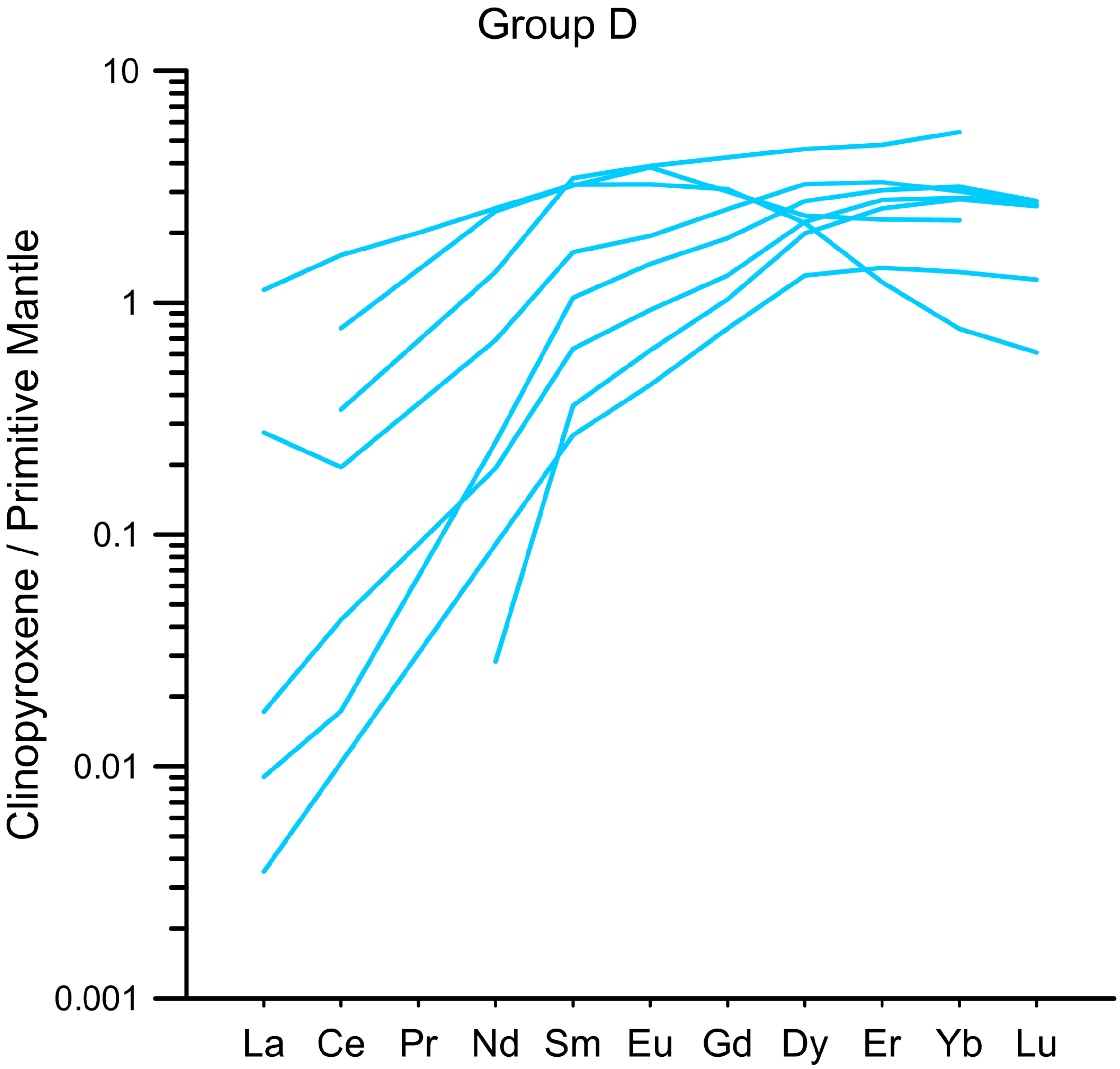

Figure A.2: Rare earth elements in clinopyroxene normalized to primitive mantle (McDonough and Sun, 1995). Group D samples generally display no LREE enrichment, although La is occasionally enriched.

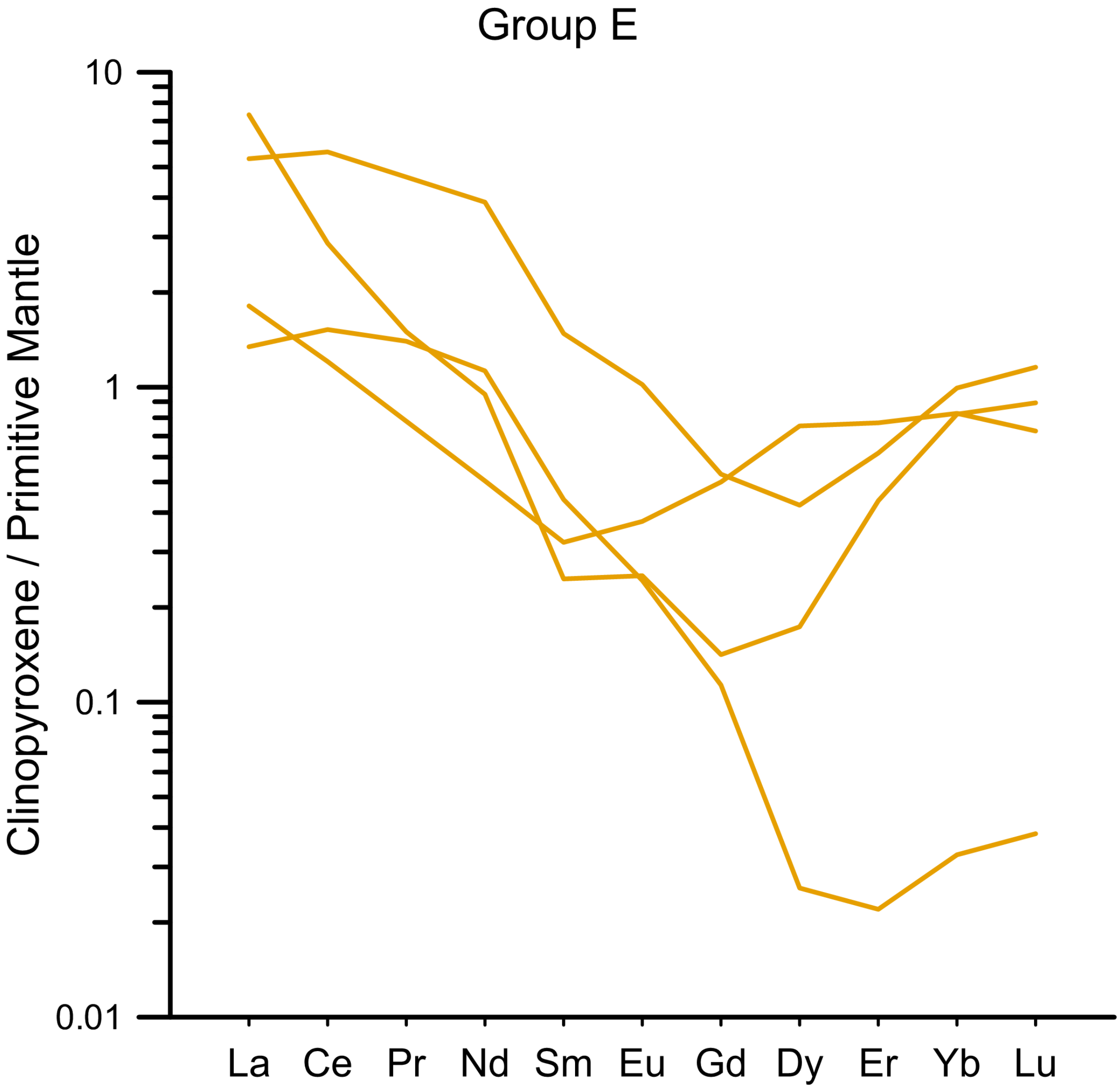

Figure A.3: Rare earth elements in clinopyroxene normalized to primitive mantle (McDonough and Sun, 1995). Group E samples have significant LREE enrichment that certainly affects Nd concentrations.

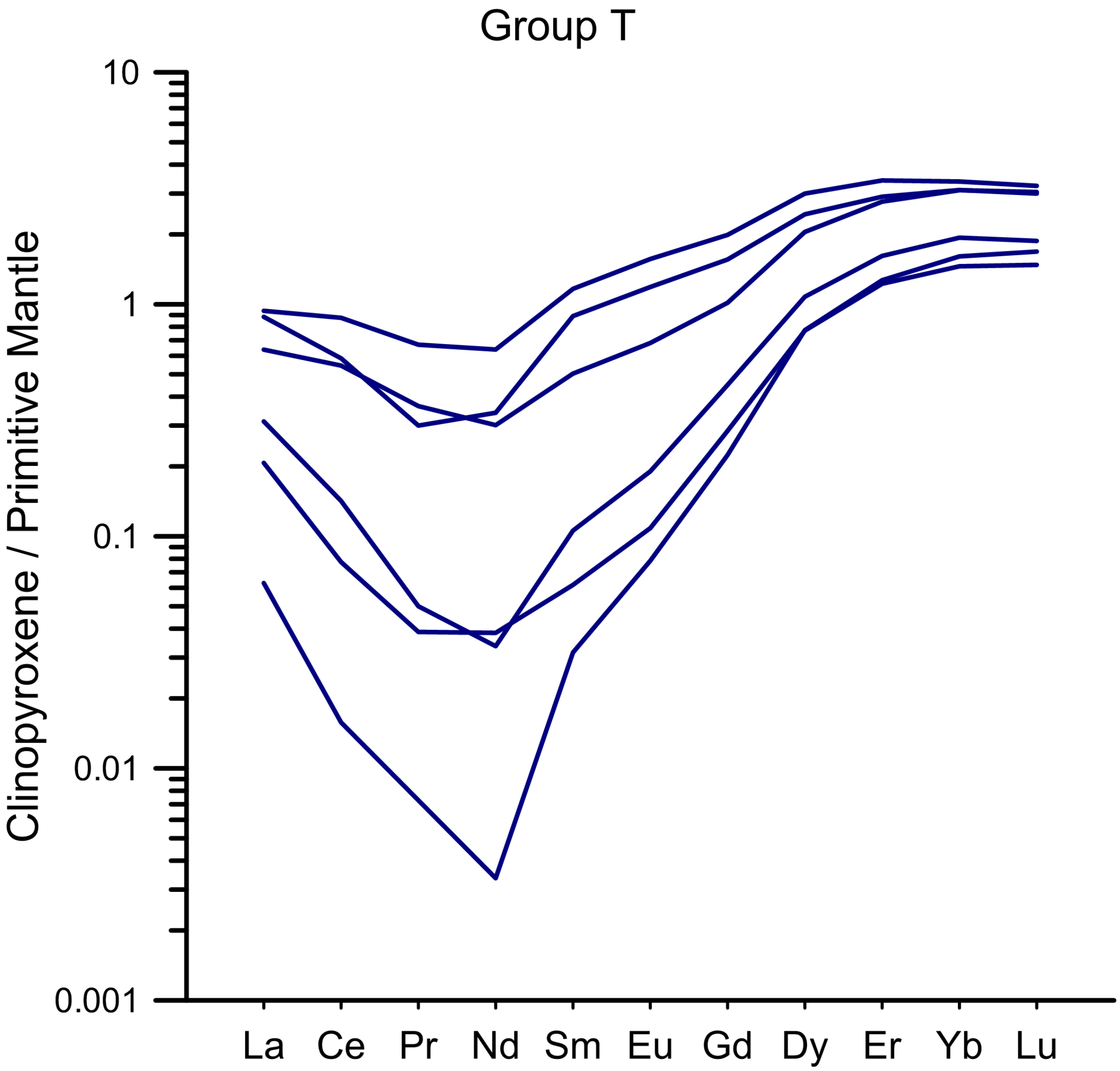

Figure A.4: Rare earth elements in clinopyroxene normalized to primitive mantle (McDonough and Sun, 1995). Group T samples have less LREE enrichment than the Group E samples. However, this LREE enrichment may still affect Nd concentrations.

# Appendix B: Supplementary material for Chapter 3

## APPENDIX B.1: WHOLE ROCK MAJOR AND TRACE ELEMENT COMPOSITIONS

Table B.1: Whole rock major and trace element compositions

| | **EMGN23** |
|---|---|
| **SiO2** | 42.35 |
| **TiO2** | 0.00 |
| **Al2O3** | 1.03 |
| **Cr2O3** | 0.39 |
| **FeO** | 6.87 |
| **MnO** | 0.11 |
| **MgO** | 42.43 |
| **CaO** | 1.05 |
| **Na2O** | 0.01 |
| **K2O** | 0.00 |
| **NiO** | 0.30 |
| **P2O5** | 0.00 |
| **LOI** | 4.57 |
| **Total** | 93.87 |
| | |
| **La** | 0.04 |
| **Ce** | 0.05 |
| **Pr** | 0.01 |
| **Nd** | 0.02 |
| **Sm** | 0.01 |
| **Eu** | 0.00 |
| **Gd** | 0.01 |
| **Tb** | 0.00 |
| **Dy** | 0.02 |
| **Ho** | 0.00 |
| **Er** | 0.02 |
| **Tm** | 0.00 |
| **Yb** | 0.04 |
| **Lu** | 0.01 |
| **Rb** | 0.12 |
| **Pb** | 0.15 |
| **Th** | 0.01 |
| **U** | 0.00 |
| **Nb** | 0.02 |
| **Sr** | 18.92 |
| **Zr** | 0.27 |
| **Hf** | 0.00 |
| **Y** | 0.17 |
| **Sc** | 7.72 |
| **V** | 33.51 |

Major elements are in wt%. Trace elements are in parts per million.

## APPENDIX B.2: CLINOPYROXENE TRACE ELEMENT COMPOSITIONS

Table B.2: Clinopyroxene trace element compositions

| | **EMGN23 Average** | **2σ** | **EMGN7 Average** | **2σ** | **EMMR7 Average** | **2σ** |
|---|---|---|---|---|---|---|
| | **Group D** | | **Group E** | | **Group D** | |
| | **n = 3** | | **n = 9** | | **n = 8** | |
| **La** | 0.08 | (0.04) | 0.05 | (0.02) | 0.05 | (0.01) |
| **Ce** | 0.23 | (0.05) | 0.08 | (0.01) | 0.07 | (0.03) |
| **Pr** | 0.04 | (0.01) | 0.01 | (0.00) | 0.01 | (0.00) |
| **Nd** | 0.24 | (0.05) | 0.03 | (0.01) | 0.05 | (0.01) |
| **Sm** | 0.10 | (0.01) | 0.01 | (0.01) | 0.10 | (0.02) |
| **Eu** | 0.05 | (0.01) | 0.01 | (0.00) | 0.07 | (0.02) |
| **Gd** | 0.20 | (0.05) | 0.02 | (0.01) | 0.39 | (0.06) |
| **Dy** | 0.45 | (0.01) | 0.09 | (0.01) | 0.96 | (0.10) |
| **Er** | 0.46 | (0.06) | 0.16 | (0.02) | 0.80 | (0.10) |
| **Yb** | 0.56 | (0.08) | 0.29 | (0.04) | 0.92 | (0.09) |
| **Lu** | 0.09 | (0.01) | 0.05 | (0.01) | 0.13 | (0.01) |
| **Rb** | 0.02 | (0.05) | bd | | bd | |
| **Th** | 0.01 | (0.01) | bd | | bd | |
| **U** | bd | | bd | | bd | |
| **Nb** | 0.02 | (0.02) | 0.01 | (0.01) | 0.01 | (0.01) |
| **Ta** | 0.00 | (0.00) | bd | | bd | |
| **Pb** | 0.04 | (0.03) | bd | | bd | |
| **Sr** | 7.51 | (6.45) | 2.53 | (2.06) | 0.94 | (0.84) |
| **Zr** | 0.53 | (0.09) | 0.04 | (0.02) | 0.05 | (0.01) |
| **Hf** | 0.01 | (0.00) | bd | | 0.02 | (0.00) |
| **Y** | 3.42 | (0.25) | 1.04 | (0.07) | 6.43 | (0.52) |
| **V** | 190 | (6.71) | | | | |

**bd: below detection**

Major elements are in wt%. Trace elements are in parts per million.

## APPENDIX B.3: SAMPLE DESCRIPTIONS

Samples that have an asterisk (e.g. **EMMR7***) are samples that do not have thin sections. Phase assemblages in these samples were identified using crushed mineral separates, and are less reliable.

### Appendix B.3.1: Moses Rock:

**Collected by Authors:**

**EMMR4**
**Mineralogy:** Serpentine + amphibole + chlorite + opaque
**Location:** 37.1081°N, 109.7841°W
**Previous studies also using this sample:** Marshall et al., 2017.

**EMMR7***
**Mineralogy:** Ol + opx + cpx + Al-spinel + chlorite
**Location:** 37.1081°N, 109.7841°W

**EMMR25**
**Mineralogy:** Ol + opx + chlorite + cpx + amphibole + serpentine + opaque
**Location:** 37.1081°N, 109.7841°W
**Previous studies also using this sample:** Marshall et al., 2017.

**Collected by Prof. Douglas Smith:**

**MR-ATG-13** (Sample collected by Anna T. Gavasci)
**Mineralogy:** ol + opx + cpx + serpentine + Al-spinel
**Location:** 37.1081°N, 109.7841°W
**Previous studies also using this sample:** Marshall et al., 2017.

### Appendix B.3.2: Green Knobs

**Collected by Authors:**

**EMGN2**
**Mineralogy:** Ol + opx + cpx + Al-Spinel + serpentine
**Location:** 35.9533° N, 109.0227° W
**Previous studies also using this sample:** Marshall et al., 2017.

**EMGN7***
**Mineralogy:** Ol + opx + cpx + chlorite + spinel
**Location:** 35.9533° N, 109.0227° W

**EMGN9**
**Mineralogy:** Ol + opx  + chlorite + opaque + amphibole + serpentine
**Location:** 35.9533° N, 109.0227° W
**Previous studies also using this sample:** Marshall et al., 2017.

**EMGN10**
**Mineralogy:** Ol + serpentine + amphibole + opx + chlorite + opaque
**Location:** 35.9533° N, 109.0227° W

**EMGN13***
**Mineralogy:** Ol + opx + chlorite + serpentine + amph?
**Location:** 35.9533° N, 109.0227° W

**EMGN17**
**Mineralogy:** Ol + opx + cpx + serpentine + chlorite
**Location:** 35.9533° N, 109.0227° W

**EMGN21**
**Mineralogy:** Ol + opx + chlorite + serpentine + opaque.
**Location:** 35.9533° N, 109.0227° W
**Previous studies also using this sample:** Marshall et al., 2017.

**EMGN23**
**Mineralogy:** Ol + opx + chlorite + opaque + amphibole
**Location:** 35.9533° N, 109.0227° W

**EMGN24**
**Mineralogy:** Ol + opx + serpentine + amphibole + chlorite + opaques + clinohumite + carbonate
**Location:** 35.9533° N, 109.0227° W
**Previous studies also using this sample:** Marshall et al., 2017.

**EMGN27**
**Mineralogy:** Ol + opx + serpentine + amphibole + carbonate + chlorite + cpx + opaques
**Location:** 35.9533° N, 109.0227° W
**Previous studies also using this sample:** Marshall et al., 2017.

**EMGN33***
**Mineralogy:** Ol + opx + chlorite + spinel
**Location:** 35.9533° N, 109.0227° W

**Collected by Prof. Douglas Smith:**

**N15-GN**
**Mineralogy**: Antigorite + olivine + carbonate + cpx + clinohumite + opaques
**Location:** 35.9533° N, 109.0227° W
**Previous studies also using this sample:** Smith, 1979; Smith, 2010.

**N16-GN**
**Mineralogy:** Ol + Al-spinel + cpx + opx + serpentine
**Location:** 35.9533° N, 109.0227° W
**Previous studies also using this sample:** Smith and Levy, 1976; Roden et al., 1990; Roden and Shimizu, 1993; Smith, 2013; Behr and Smith, 2016; Marshall et al., 2017.

**N17-GN**
**Mineralogy:** Ol + opx + cpx + chlorite + serpentine + amphibole + opaque + magnesite
**Location:** 35.9533° N, 109.0227° W
**Previous studies also using this sample:** Smith and Levy, 1976; Smith, 1979; Roden and Shimizu, 1993; Smith, 2013; Behr and Smith, 2016; Marshall et al., 2017.

**N23-GN**
**Mineralogy:** Ol + opx + chlorite + cpx + amphibole + clinohumite + opaque + magnesite + antigorite
**Location:** 35.9533° N, 109.0227° W
**Previous studies also using this sample:** Smith, 1979; Roden et al., 1990; Roden and Shimizu, 1993; Smith, 2013; Behr and Smith, 2016; Marshall et al., 2017.

**N51-GN**
**Mineralogy:** Ol + Antigorite + chlorite + carbonate + opx + cpx + clinohumite
**Location:** 35.9533° N, 109.0227° W

**N55-GN**
**Mineralogy:** Ol + opx + cpx + sp + amph + serpentine + garnet + chlorite
**Location:** 35.9533° N, 109.0227° W
**Previous studies also using this sample:** Smith and Levy, 1976; Smith, 1979; Marshall et al., 2017.

**N57-GN**

**Mineralogy:** Ol + opx + chlorite + serpentine + amphibole + cpx + carbonate
**Location:** 35.9533° N, 109.0227° W
**Previous studies also using this sample:** Smith, 1979.

**N61-GN**
**Mineralogy:** Ol + opx + cpx + Al-spinel +amph
**Location:** 35.9533° N, 109.0227° W
**Previous studies also using this sample:** Smith and Levy, 1976; Roden et al., 1990; Roden and Shimizu, 1993; Marshall et al., 2017.

**N71-GN**
**Mineralogy:** Ol + opx + chlorite + amphibole + serpentine + cpx + carbonate + opaque
**Location:** 35.9533° N, 109.0227° W
**Previous studies also using this sample:** Smith, 1979; Roden et al., 1990; Roden and Shimizu, 1993.

**N106-GN**
**Mineralogy:** Ol + opx + cpx + chlorite + amphibole + opaques + spinel + garnet + antigorite
**Location:** 35.9533° N, 109.0227° W
**Previous studies also using this sample:** Behr and Smith, 2016; Marshall et al., 2017.

**N126-GN**
**Mineralogy:** Ol + opx + cpx + Al-spinel + serpentine
**Location:** 35.9533° N, 109.0227° W
**Previous studies also using this sample:** Smith, 1977; Marshall et al., 2017.

**N143-GN**
**Mineralogy:** Ol + serpentine + opx + cpx + carbonate + chlorite
**Location:** 35.9533° N, 109.0227° W

**N178-GN**
**Mineralogy:** Ol + opx + cpx + chlorite + Cr-spinel + phlogopite (trace)
**Location:** 35.9533° N, 109.0227° W
**Previous studies also using this sample:** Smith, 2010; Smith, 2013; Behr and Smith, 2016; Marshall et al., 2017.

**N182-GN***
**Mineralogy:** Ol + serpentine + chlorite + opx
**Location:** 35.9533° N, 109.0227° W

**N234-GN***
**Mineralogy:** Serpentine
**Location:** 35.9533° N, 109.0227° W

**N363-GN***
**Mineralogy:** Serpentine + carbonate
**Location:** 35.9533° N, 109.0227° W

## APPENDIX B.4: OXYGEN ISOTOPE COMPOSITIONS

Table B.4: Oxygen isotope compositions

| | | δ18O Duplicates (‰) | | | | | |
|---|---|---|---|---|---|---|---|
| | | 1 | 2 | 3 | 4 | Average δ18O | 1 s.d. |
| MR-ATG-13 | Group D | 5.28 | | | | 5.28 | |
| N126 | Group D | 5.21 | | | | 5.21 | |
| N16-GN | Group D | 5.34 | 5.36 | | | 5.35 | 0.01 |
| N61-GN | Group D | 5.14 | 5.14 | | | 5.14 | 0.00 |
| N106-GN | Group D | 5.15 | 5.32 | | | 5.24 | 0.12 |
| EMGN24 | Group D | 5.12 | | | | 5.12 | |
| N23-GN | Group D | 5.16 | 5.24 | 5.05 | | 5.15 | 0.10 |
| EMGN23 | Group D | 5.27 | 5.25 | | | 5.26 | 0.01 |
| EMGN2 | Group T | 5.14 | | | | 5.14 | |
| N17-GN | Group T | 5.13 | 5.05 | 5.04 | 5.09 | 5.08 | 0.04 |
| EMMR7 | Group T | 5.13 | | | | 5.13 | |
| N55-GN | Group E | 5.07 | 5.02 | | | 5.05 | 0.03 |
| EMGN21 | Group E | 5.08 | | | | 5.08 | |
| EMGN27 | Group E | 5.10 | | | | 5.10 | |
| EMGN7 | Group E | 5.08 | 5.16 | | | 5.12 | 0.06 |

All values are reported relative to SMOW

## APPENDIX B.5: HYDROGEN ISOTOPE COMPOSITIONS

Table B.5: Hydrogen isotope compositions

| | | δD Duplicates (‰) | | | | | | | | |
|---|---|---|---|---|---|---|---|---|---|---|
| Sample | Mineral | 1 | 2 | 3 | 4 | 5 | 6 | 7 | δD value (‰) | 1 s.d. |
| EMGN10 | Serpentine | -79 | | | | | | | -79 | |
| EMGN13 | Chlorite | -37 | -34 | | | | | | -36 | 2 |
| EMGN17 | Chlorite | -41 | -41 | | | | | | -41 | 0 |
| EMGN21 | Chlorite | -42 | -42 | | | | | | -42 | 0 |
| EMGN23 | Chlorite | -49 | -52 | | | | | | -51 | 2 |
| EMGN27 | Chlorite | -45 | -42 | | | | | | -44 | 2 |
| EMGN33 | Chlorite | -67 | -74 | | | | | | -71 | 5 |
| EMGN7 | Chlorite | -44 | -44 | | | | | | -44 | 0 |
| EMGN9 | Chlorite | -44 | -49 | -41 | -46 | | | | -45 | 3 |
| EMMR25 | Chlorite | -46 | -43 | | | | | | -45 | 2 |
| EMMR4 | Chlorite | -67 | -65 | | | | | | -66 | 2 |
| N106-GN | Chlorite | -35 | -53 | | | | | | -44 | 13 |
| N143-GN | Serpentine | -47 | | | | | | | -47 | |
| N15-GN | Serpentine | -47 | -48 | -54 | | | | | -50 | 4 |
| N178-GN | Chlorite | -49 | | | | | | | -49 | |
| N182-GN | Serpentine | -50 | | | | | | | -50 | |
| N23-GN | Chlorite | -32 | -34 | -31 | -31 | -31 | -33 | -36 | -33 | 2 |
| N234-GN | Serpentine | -65 | | | | | | | -65 | |
| N363-GN | Serpentine | -45 | | | | | | | -45 | |
| N51-GN | Serpentine | -66 | -46 | | | | | | -56 | 14 |
| N57-GN | Serpentine | -71 | | | | | | | -71 | |
| N71-GN | Chlorite | -47 | -45 | -44 | -50 | | | | -46 | 3 |

All δD values relative to SMOW

## APPENDIX B.6: SUPPLEMENTARY PLOTS FOR CHAPTER 3

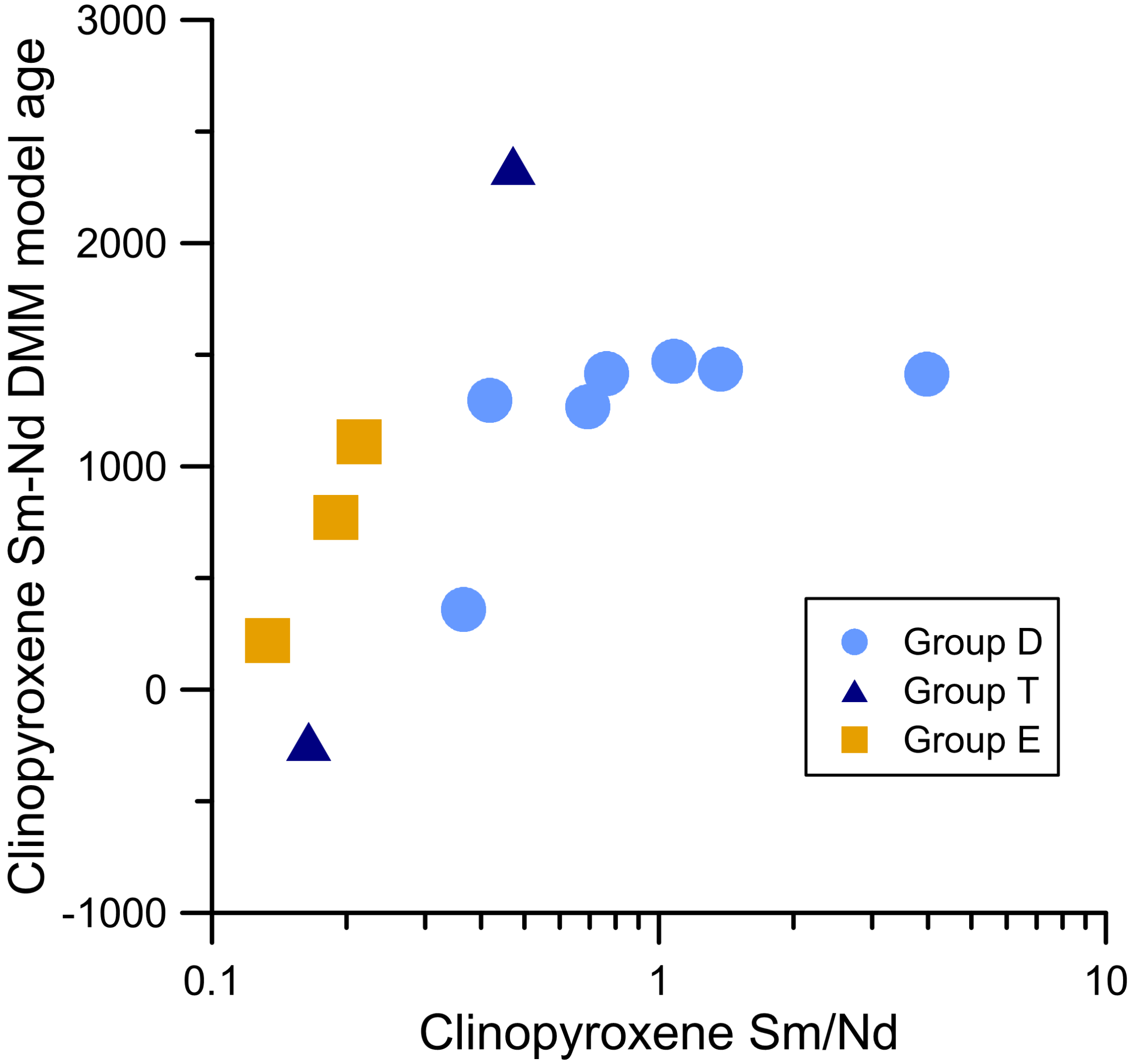

Figure B.1: Plot of Sm/Nd in clinopyroxene versus Sm-Nd DMM model age in clinopyroxene. Lower Sm/Nd ratios represents more metasomatised samples. As samples become more metasomatised, they have a younger DMM model age. This trend suggests recent metasomatism, most likely related to Farallon subduction.

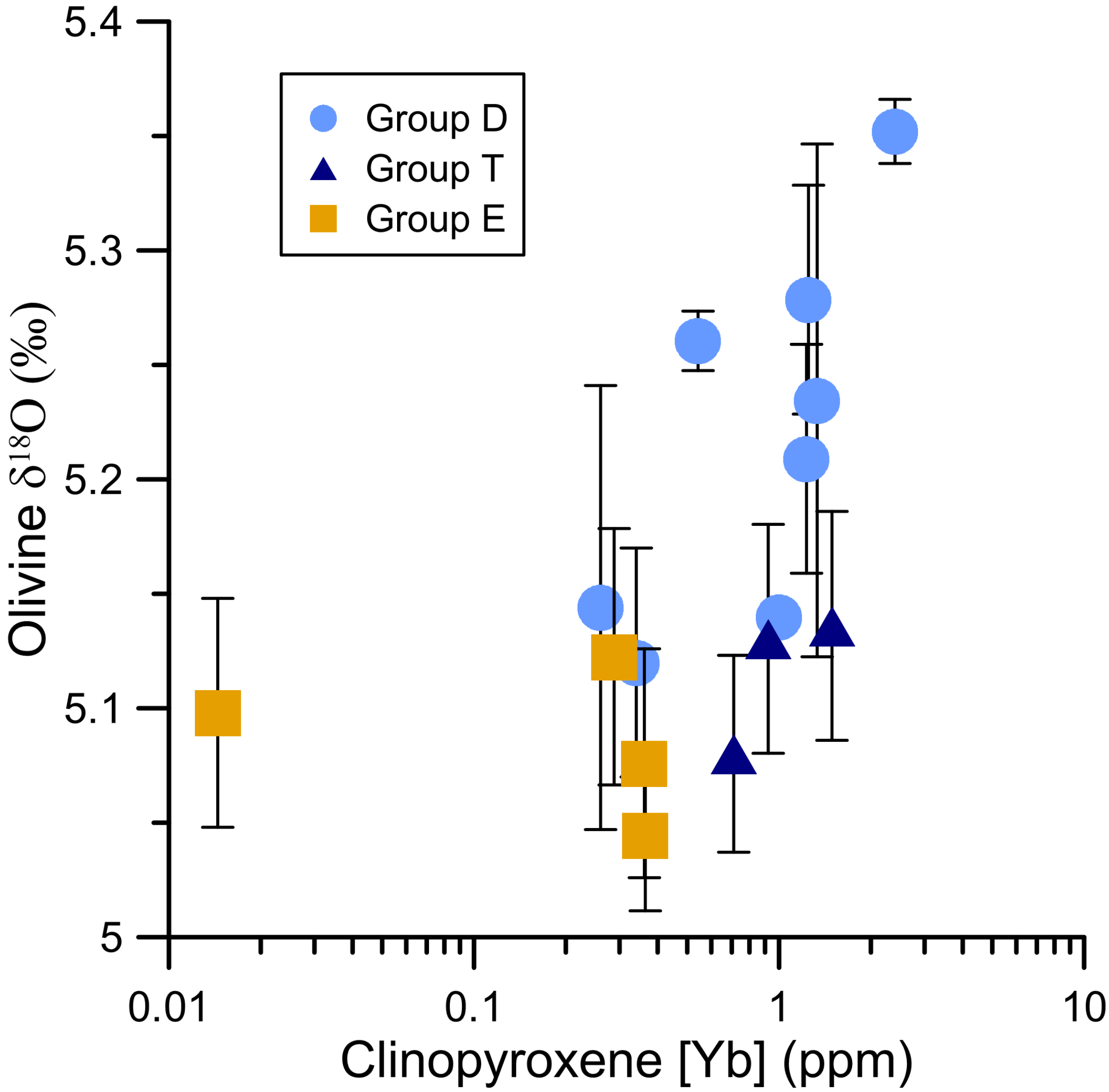

Figure B.2: Clinopyroxene Yb concentration versus olivine oxygen isotope composition. Lower Yb concentration represents increasing melt depletion.

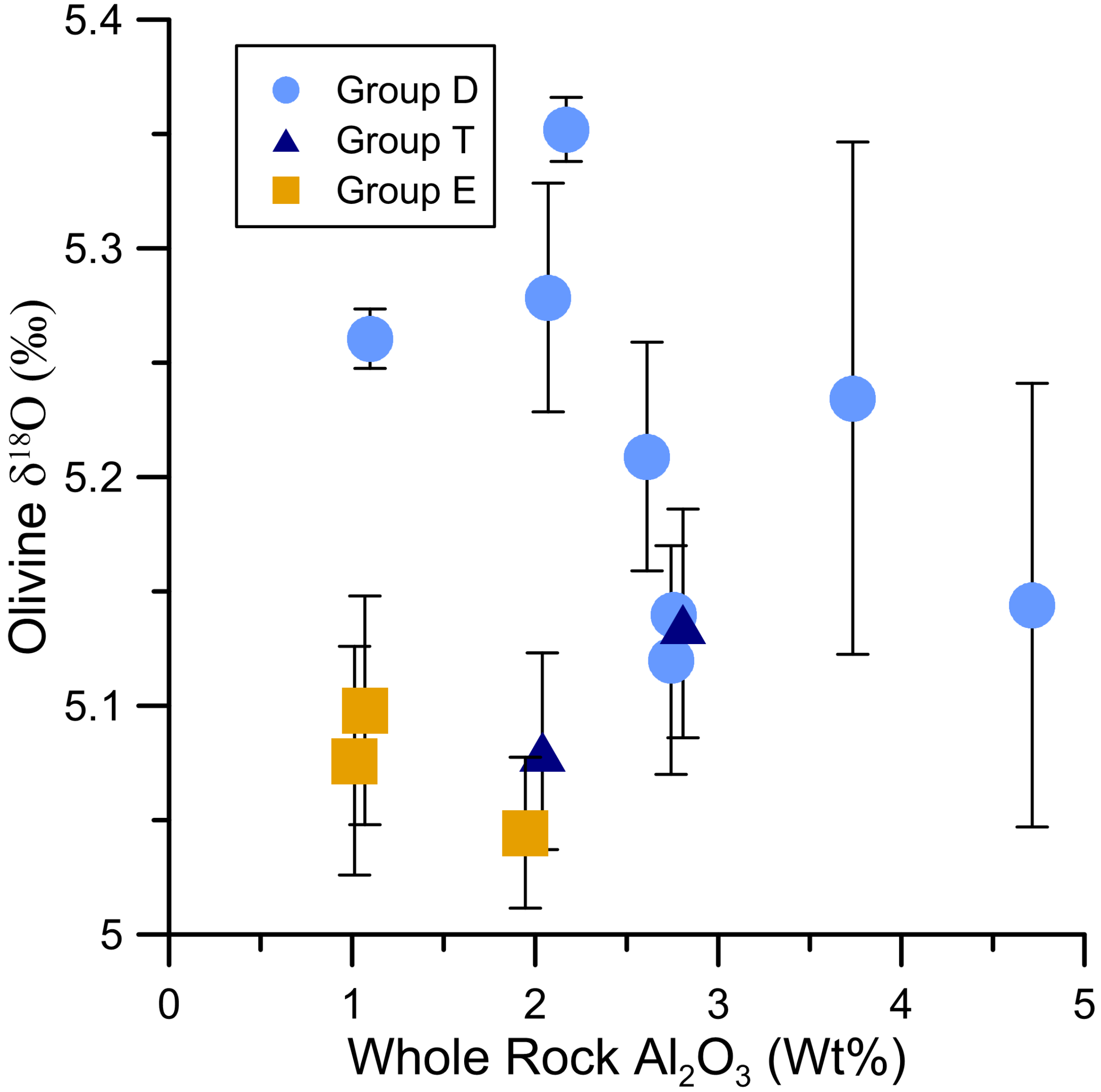

Figure B.3: Dry whole rock $Al_2O_3$ concentration (normalized without LOI) versus olivine oxygen isotope composition. Increasing melt depletion lowers the whole rock $Al_2O_3$ concentration.

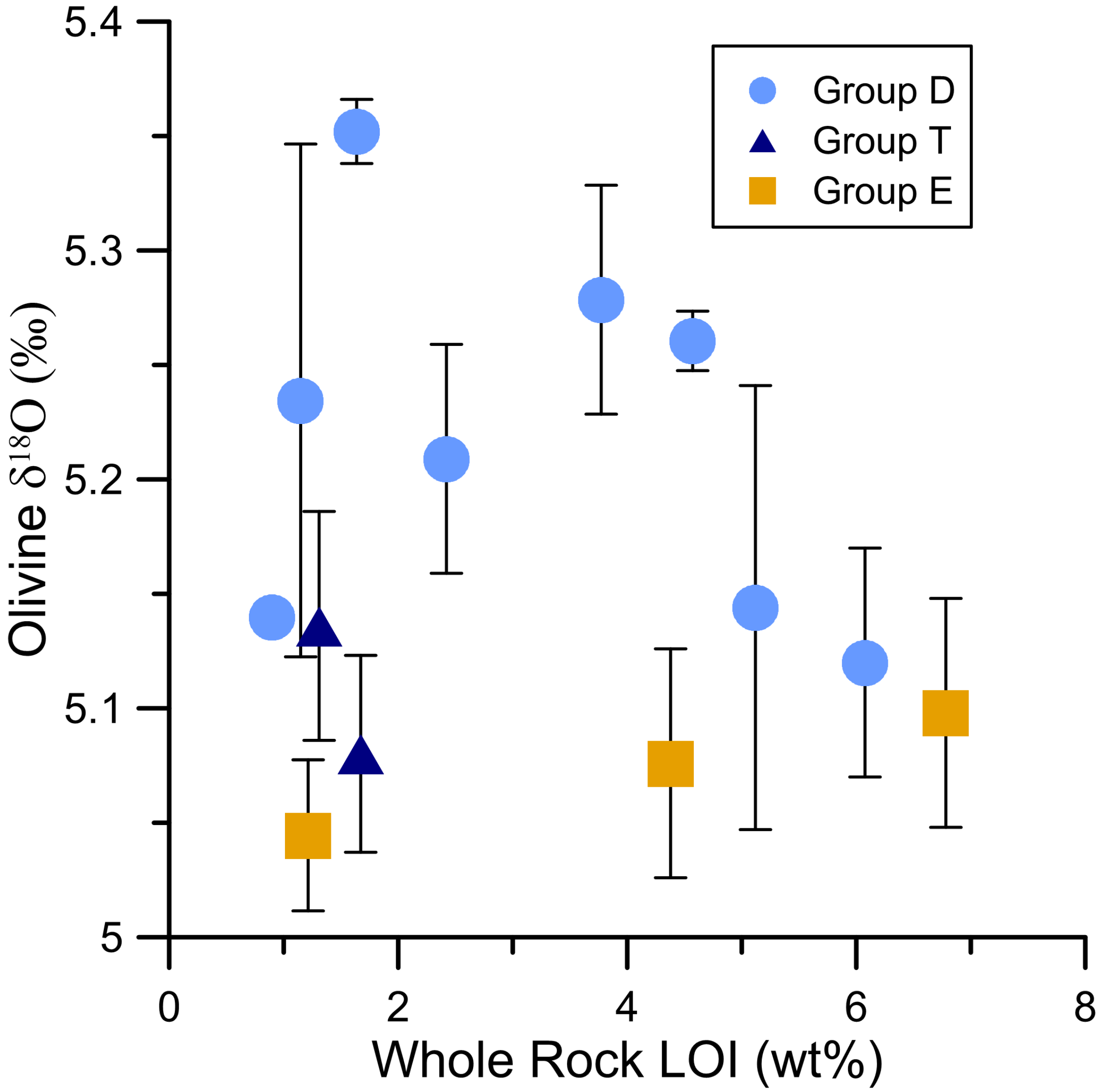

Figure B.4: Whole rock Loss-on-Ignition (LOI) versus olivine oxygen isotope composition. Higher LOI represents more abundant hydrous minerals in a sample.

# Appendix C: Supplementary material for Chapter 4

## APPENDIX C.1: SUPPLEMENTARY ANALYTICAL METHODS FOR CHAPTER 4

### Appendix C.1.1: Indium sample mount preparation

~10 grams of each xenolith sample were crushed in a steel mortar and pestle to separate individual peridotite mineral grains. The crushed minerals were then washed and sonicated to remove dust and clinging surficial material. Approximately thirty inclusion-free clinopyroxene (cpx) and orthopyroxene (opx) grains were then picked from each sample. These grains were mounted in crystalbond and polished up to 1 micron grit. The crystal bond was dissolved in an acetone bath, and the grains were rinsed with clean acetone, ethanol, and finally DI water. The grains were then ready to be mounted in the indium mounts.

Samples were mounted in indium metal because epoxy has been found to degas hydrogen at high vacuum and lead to high hydrogen blank. The preparation of these mounts uses the online published procedures of the University of Edinburgh (http://www.ed.ac.uk/files/imports/fileManager/IndiumMountPrep.pdf), and is replicated here. 1'' diameter aluminum disks with a central 0.75'' cylindrical depression were used to hold the indium. High purity (99.9999%) indium beads were melted in the cylindrical depression. The mounts were heated to ca. 250°C on a hot plate to melt the indium and volatilize organics that are adhered to the mount. Following cooling, great care was made to not expose the mounts to particulates, oils or other sources of hydrogen contamination.

The mounts were then pressed in a hydraulic press to achieve a mirror-like flat surface. The mounts were sandwiched between two stiff plastic Melinex™ sheets and polished aluminum blocks. The mounts were pressed to five tons, as measured from the hydraulic jack gauge. We found that this pressure slightly deforms the mount by a few millimeters and that this pressure is probably excessive. Following pressing, the outside of the mounts had to be ground on a polishing wheel by a few millimeters to correct the deformation and fit them into 1'' sample holders for Electron Probe MicroAnalysis (EPMA) and Secondary Ion Mass Spectrometry (SIMS) analysis.

Polished sample grains were then placed gently into the mount and pressed into the indium with a clean microscope slide. The mounts were then repressed in the hydraulic press using the same procedures as in the initial pressing, but only pressing to ~1 ton. Following pressing, each mount was gently polished with 1 micron diamond suspension and a polishing cloth. Finally, each mount was sonicated for 10 seconds in 18MΩ water to remove particulates.

Samples were carbon coated and analyzed for major elements on the JOEL 8200 EPMA at UT Austin before SIMS analysis (methods identical to Marshall et al., 2017b). Samples used the same carbon coat on the EPMA and SIMS. Spot analyses conducted by EPMA and SIMS were made on the same locations to create a spatially matching dataset. If the mounts needed to be stored at any time during the above procedures, the mounts were wrapped in Aluminum foil and left in an oven at 80°C.

### Appendix C.1.2: SIMS Analysis

Hydrogen analyses used the Cameca 6f SIMS at Arizona State University. Because hydrogen analyses are very sensitive to background, care was taken to reduce the H background as much as possible. Before insertion into the main chamber, each mount was left in the antechamber of the SIMS at ca. $2x10^{-8}$ torr for 20 to 24 hours before analysis. Although other studies have had success baking out the SIMS for 24-48 hours before analysis, we found that running the Ti sublimation pump the night before an analytical session resulted in equally reduced chamber pressure. Main chamber pressures ranged between 2.5 and $4x10^{-10}$ torr during SIMS analysis.

Analyses were made using a 10nA rastered Cs+ beam using the same instrument as, and similar analytical approach to, Tenner et al. (2009). The primary beam was approximately 20µm in diameter and the beam was rastered across a 40um square area. During analysis, a field aperture was used to mask the ion beam such that only ions from an 8µm diameter circular area in the center of the rastered area were sampled. Intensities were measured by electron multiplier, for $^{16}O^{1}H$, $^{18}O$, $^{19}F$, $^{28}Si$, $^{35}Cl$. Isotopologues $^{16}O^{1}H$ and $^{17}O$ were distinguished by using a mass resolving power of 5000. Prior to every spot analysis, the $^{16}O^{1}H$ ion image was first monitored to detect the presence of cracks, hydrous mineral inclusions, or other defects that could contaminate the analysis. Spots were presputtered for 2 min before analysis. Variability in $^{16}O^{1}H$ and $^{35}Cl$ were carefully monitored as a test for contamination or inclusions that may be encountered as the sample was sputtered. Even in grains that appear to be optically clear, tiny inclusions and cracks can generate anomalously high water contents. Analyses occasionally sputtered through a crack or inclusion, resulting in abnormally high water content (>10,00ppm).

### Appendix C.1.3: SIMS Data Reduction and Standardization

Water contents in measured NAMs were quantified from their measured $^{16}O^{1}H/^{28}Si$ intensity using a calibration curve made of well-characterized pyroxene and olivine standards. Each mount included grains of 2-4 standards and 1-2 blanks. Because this study analyzed orthopyroxene (opx) and clinopyroxene (cpx), standards composed of opx and cpx were used to minimize matrix effects. Standards in this study have all been characterized in the studies Mosenfelder and Rossman (2013a) and Mosenfelder and Rossman, (2013b): PMR-53, GRR1017 (a blank), 62047-70B, CIT17210, JLM77, GRR2334a, GRR1650b, and JLM50. Olivine from a San Carlos xenolith (sample#: SC3) in the collection of Professor Douglas Smith was used as a blank in all mounts. SC3 olivine has water content below the detection of several oriented FTIR analyses (<3ppm, see FTIR methods below). Clinopyroxene, opx and olivine standards and blanks can be used on a single calibration curve because matrix effects between opx, cpx and olivine are negligible (Mosenfelder and Rossman, 2013a; Mosenfelder and Rossman, 2013b). Even though there are no considerable matrix effects between olivine and pyroxene, olivine has lower molar abundance of Si than pyroxene that increases the measured $^{16}O^{1}H/^{28}Si$. To account for this compositional difference between olivine and pyroxene, $^{16}O^{1}H/^{28}Si$ intensities of olivine were multiplied by the ratio of molar silicon in each phase (5/7).

Different sample mounts were measured each day on the SIMS. Blanks and standards were measured in blocks throughout the day. Each block of blank and standard analyses was used to background correct and build a calibration curve that would quantify the sample data immediately before and after the blank-standard block. Sample data from each SIMS mount would therefore be calibrated by several independent calibration curves to eliminate any drift over the course of the day. The procedure for constructing a calibration curve is similar to the methods of Koga et al., (2003):

1. For each set of blanks and standards, the $^{16}O^{1}H/^{28}Si$ intensity of the blank was subtracted from the blank, standard, and adjacent sample analyses to generate background-subtracted $^{16}O^{1}H/^{28}Si$ intensities.
2. The accepted water concentrations for the blank and standards and their background-subtracted $^{16}O^{1}H/^{28}Si$ intensities were regressed with a least-squares regression function that was forced through the origin. Calibration curves consisted of at least 1 blank analysis and at least 2 standard analyses.
3. The background-corrected sample $^{16}O^{1}H/^{28}Si$ intensities were converted into water contents using the equation derived from the regression function from step 2.

PMR-53 was used differently than other standards because of its known mismatch of apparent water concentration between the FTIR and SIMS techniques (see Mosenfelder and Rossman, 2013a). Previous studies of PMR-53 water content by SIMS and manometry, found that SIMS analysis of PMR-53 yielded anomalously high OH/Si intensity relative to its water content as measured by manometry (Bell et al., 1995; Mosenfelder and Rossman, 2013a). Grains of PMR-53 were included on all mounts and therefore the treatment of PMR-53 during data reduction is very important. We chose to treat PMR-53 as a homogenous in-house standard instead of as a calibrating standard. On samples where PMR-53 was mounted along with two other non-blank standards (standards as listed above), PMR-53 was analyzed as an unknown and its calculated water content was recorded. The calculated average for PMR-53 in the study, as measured as an unknown, was 296 ±17 (2SE) ppm (n=18), whereas the accepted manometry concentration from Bell et al. (1995) was 268 ppm. For mounts that contained PMR-53 and only one other standard, PMR-53 was used as a calibrating standard with a water concentration of 296 ppm, as averaged from the other mounts.

The background water content for the analyses ranged between 6 and 113 ppm, and was <40ppm for most sample mounts. Background water content was measured by regressing the blank-uncorrected $^{16}O^{1}H/^{28}Si$ intensities of the blank and calibrating standards against their accepted water contents Fig. A3.13.1). The negative y-intercept of this regression is equal to the background.

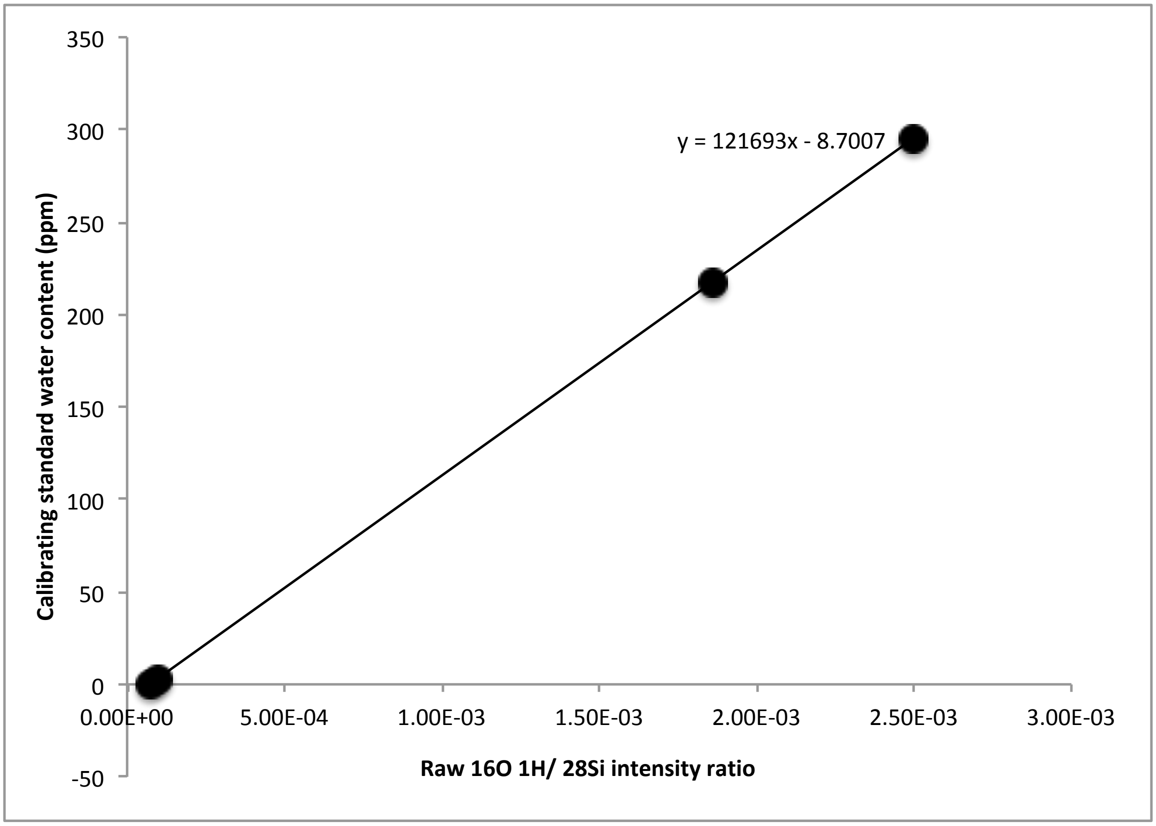

Figure C.1: $^{16}O^{1}H/^{28}Si$ standard intensities versus their accepted values. This is calibration curve A1 (A1 is presented as an example. For other calibration curve data see Appendix 3.3). The background water content is equal to the negative of the y-intercept, or 8.7 ppm.

## Appendix C.1.4: FTIR methods for analysis of olivine blank

Clear, inclusion-free olivine grains from San Carlos xenolith SC3 were doubly exposed and measured for oriented OH absorbance on the Fourier Transform Infared spectrometer (FTIR) at The University of Texas at Austin. Doubly exposed grains that were crystallographically oriented along the x, y, or z optical axes, were identified using a petrographic microscope. Only grains that had centered BXA, BXO, or flash figures were used for analyses. FTIR spectra were collected from 3800 $cm^{-1}$ to 2800 $cm^{-1}$ using a ThermoElectron Nicolet 6700 spectrometer and Continuμm IR microscope. No absorption peaks were observed in the SC3 olivines, related to the low water content of the material and the thinness of the doubly exposed grain mounts (30 μm). An absorption peak that is small enough to be indistinguishable from variability in the absorption curve would have a water concentration of ~3 ppm. Therefore, SC3 olivine contains less than 3 ppm water.

## APPENDIX C.2 SUPPLEMENTARY FIGURES FOR CHAPTER 4

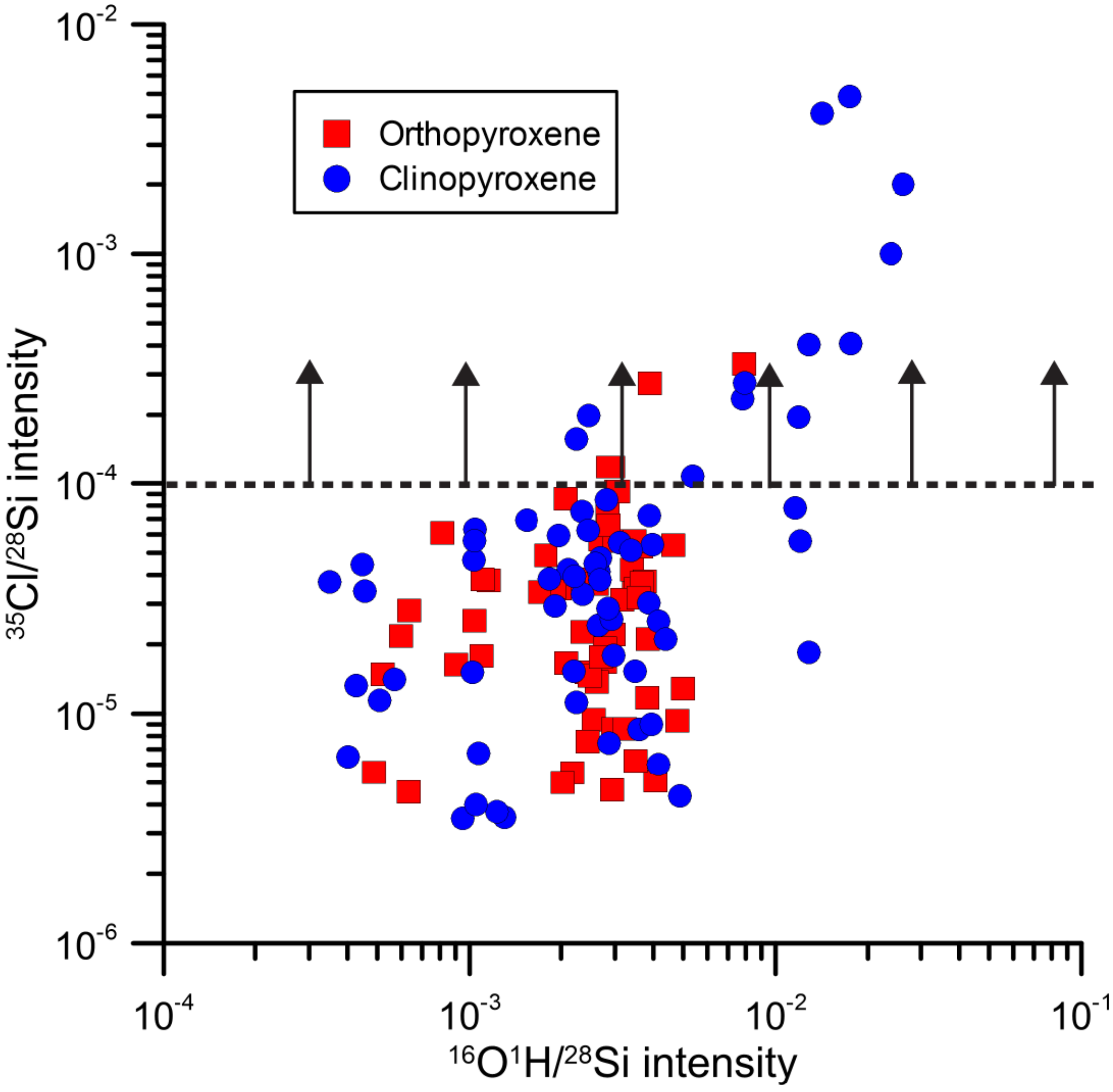

Figure C.2: Plot of OH/Si intensity ratio versus Cl/Si intensity ratio. Dashed line represents the limit above which sample analyses are considered contaminated and not used in filtering or averaging of the data.

# APPENDIX C.3: SAMPLE AND STANDARD INTENSITIES FOR SIMS ANALYSES

Sample Mount A

| Sample ID | Analytical Role | Sample ID | Phase (Identified by probe) | Grain # | Analysis # on grain | Calibration curve | OH/Si | SE (%) | 18O/Si | SE (%) | 19F/Si | SE (%) | 35Cl/Si | SE (%) | 28Si counts | SE (%) | Background subtracted OH/Si | Standard H2O (ppm) | Calculated H2O Content |
|---|---|---|---|---|---|---|---|---|---|---|---|---|---|---|---|---|---|---|---|
| A-SC3-1 | Blank | San Carlos | Olivine | 1 | 1 | A1 | 9.57E-05 | 2.78 | 8.65E-02 | 0.26 | 5.14E-05 | 3.96 | 5.291E-06 | 19.00 | 153316 | 0.19 | 2.48E-05 | 3 | 3 |
| A-JLM77-1 | Calibrating Standard | JLM-77 | Cpx | 1 | 1 | A1 | 1.86E-03 | 0.60 | 6.72E-02 | 0.34 | 1.78E-02 | 0.26 | 1.124E-05 | 13.04 | 230054 | 0.55 | 1.79E-03 | 217 | 218 |
| A-PMR53-1 | Calibrating Standard | PMR-53 | Cpx | 1 | 1 | A1 | 2.50E-03 | 0.88 | 6.66E-02 | 0.98 | 6.27E-03 | 0.87 | 1.414E-05 | 16.42 | 226634 | 2.24 | 2.43E-03 | 296 | 295 |
| A-GRR1017-1 | Blank | GRR1017 | Olivine | 1 | 1 | A1 | 7.08E-05 | 2.48 | 9.23E-02 | 0.17 | 1.16E-05 | 9.60 | 8.545E-06 | 10.76 | 160004 | 0.07 | 0.00E+00 | 0 | 0 |
| A-EMGN7-1 | Sample | EMGN7 | Cpx | 1 | 1 | A1 | 2.24E-03 | 0.58 | 6.25E-02 | 0.19 | 8.51E-05 | 3.90 | 1.123E-05 | 6.85 | 182750 | 0.21 | 2.17E-03 |  | 264 |
| A-EMGN7-2 | Sample | EMGN7 | Cpx | 2 | 1 | A1 | 2.59E-03 | 0.58 | 6.44E-02 | 0.19 | 9.43E-05 | 2.83 | 4.498E-05 | 7.53 | 195211 | 0.15 | 2.52E-03 |  | 306 |
| A-EMGN24-1 | Sample | EMGN24 | Cpx | 1 | 1 | A1 | 3.48E-03 | 0.45 | 6.69E-02 | 0.25 | 4.56E-05 | 6.75 | 1.53E-05 | 10.48 | 168927 | 0.25 | 3.41E-03 |  | 415 |
| A-EMGN24-2 | Sample | EMGN24 | Cpx | 2 | 1 | A1 | 4.16E-03 | 0.62 | 6.99E-02 | 0.21 | 4.77E-05 | 4.86 | 6.025E-06 | 14.57 | 168440 | 0.15 | 4.09E-03 |  | 497 |
| A-MRATG13-1 CORE | Sample | MR-ATG-13 | Cpx | 1 | 1 | A1 | 1.07E-03 | 0.96 | 6.64E-02 | 0.22 | 8.41E-04 | 1.31 | 6.748E-06 | 16.57 | 157888 | 0.10 | 9.99E-04 |  | 122 |
| A-MRATG13-1 RIM | Sample | MR-ATG-13 | Cpx | 1 | 2 | A1 | 1.23E-03 | 0.85 | 6.79E-02 | 0.29 | 8.45E-04 | 0.84 | 3.73E-06 | 21.07 | 155817 | 0.39 | 1.16E-03 |  | 141 |
| A-MRATG13-2 | Sample | MR-ATG-13 | Cpx | 2 | 1 | A2 | 2.68E-03 | 1.40 | 6.92E-02 | 1.48 | 8.28E-04 | 2.07 | 3.824E-05 | 7.97 | 150381 | 1.14 | 2.60E-03 |  | 325 |
| A-EMGN17-1 | Sample | EMGN17 | Cpx | 1 | 1 | A2 | 2.24E-03 | 0.58 | 6.25E-02 | 0.19 | 8.51E-05 | 3.90 | 1.123E-05 | 6.85 | 182750 | 0.21 | 2.16E-03 |  | 270 |
| A-EMGN17-2 | Sample | EMGN17 | Cpx | 2 | 1 | A2 | 2.97E-03 | 0.94 | 7.01E-02 | 0.33 | 4.69E-04 | 2.03 | 1.792E-05 | 5.87 | 169546 | 0.32 | 2.89E-03 |  | 362 |
| A-N126-1 | Sample | N126 | Cpx | 1 | 1 | A2 | 9.51E-04 | 0.82 | 7.28E-02 | 0.27 | 3.77E-05 | 6.50 | 3.501E-06 | 22.44 | 152415 | 0.30 | 8.73E-04 |  | 109 |
| A-N126-2 | Sample | N126 | Cpx | 2 | 1 | A2 | 1.05E-03 | 1.00 | 7.35E-02 | 0.26 | 4.19E-05 | 7.63 | 4.021E-06 | 21.29 | 132443 | 0.15 | 9.71E-04 |  | 121 |
| A-JLM77-2 | Calibrating Standard | JLM-77 | Cpx | 1 | 2 | A2 | 1.81E-03 | 0.45 | 6.62E-02 | 0.15 | 1.79E-02 | 0.29 | 8.169E-06 | 15.11 | 241923 | 0.13 | 1.73E-03 | 217 | 217 |
| A-PMR53-2 | Calibrating Standard | PMR-53 | Cpx | 1 | 2 | A2 | 2.44E-03 | 0.47 | 6.82E-02 | 0.19 | 6.16E-03 | 0.45 | 9.925E-06 | 10.01 | 178438 | 0.50 | 2.37E-03 | 296 | 296 |
| A-GRR1017-2 | Blank | GRR1017 | Olivine | 1 | 2 | A2 | 7.78E-05 | 3.32 | 9.15E-02 | 0.17 | 1.42E-05 | 13.52 | 1.002E-05 | 13.70 | 131350 | 0.16 | 0.00E+00 | 0 | 0 |
| A-JLM77-3 | Calibrating Standard | JLM-77 | Cpx | 1 | 2 | A3 | 1.92E-03 | 0.62 | 5.97E-02 | 0.22 | 1.67E-02 | 0.41 | 1.224E-05 | 11.22 | 164014 | 0.44 | 1.79E-03 | 217 | 197 |
| A-PMR53-4 | Calibrating Standard | PMR-53 | Cpx | 1 | 3 | A3 | 2.94E-03 | 0.49 | 5.99E-02 | 0.26 | 6.13E-03 | 0.50 | 6.424E-06 | 14.41 | 153562 | 0.85 | 2.81E-03 | 296 | 308 |
| A-GRR1017-3 | Blank | GRR1017 | Olivine | 1 | 3 | A3 | 1.31E-04 | 3.22 | 8.44E-02 | 0.25 | 2.30E-05 | 9.91 | 1.56E-05 | 12.84 | 104704 | 0.72 | 0.00E+00 | 0 | 0 |
| A-EMGN2OPX-1 | Sample | N61 | Opx | 1 | 1 | A3 | 3.47E-03 | 0.65 | 7.11E-02 | 0.24 | 7.38E-05 | 5.53 | 5.624E-05 | 7.42 | 108848 | 0.59 | 3.34E-03 |  | 367 |
| A-EMGN2OPX-2 | Sample | N61 | Opx | 2 | 1 | A3 | 2.85E-03 | 0.64 | 8.36E-02 | 0.21 | 5.97E-05 | 6.14 | 0.0001187 | 9.06 | 93414 | 0.17 | 2.74E-03 |  | 300 |
| A-N17OPX-1 | Sample | N17 | Opx | 1 | 1 | A3 | 3.23E-03 | 0.54 | 6.74E-02 | 0.25 | 1.51E-05 | 12.37 | 8.604E-06 | 13.51 | 120850 | 0.11 | 3.12E-03 |  | 343 |
| A-EMGN26OPX-1 | Sample | EMGN26 | Opx | 1 | 1 | A3 | 5.97E-04 | 5.73 | 6.71E-02 | 0.21 | 9.13E-06 | 13.58 | 2.176E-05 | 12.40 | 132794 | 0.51 | 4.86E-04 |  | 53 |
| A-EMGN26OPX-2 | Sample | EMGN26 | Opx | 2 | 1 | A3 | 4.89E-04 | 1.46 | 6.89E-02 | 0.27 | 1.25E-05 | 13.82 | 5.548E-06 | 16.25 | 132418 | 0.65 | 3.77E-04 |  | 41 |
| A-GRR1017-4 | Blank | GRR1017 | Olivine | 1 | 4 | A3 | 1.12E-04 | 2.14 | 8.23E-02 | 0.20 | 1.90E-05 | 9.70 | 8.829E-06 | 18.31 | 112563 | 0.32 | 0.00E+00 | 0 | 0 |

Sample Mount B

| Sample ID | Analytical Role | Sample ID | Phase (Identified by probe) | Grain # | Analysis # on grain | Calibration curve | OH/Si | SE (%) | 18O/Si | SE (%) | 19F/Si | SE (%) | 35Cl/Si | SE (%) | 28Si counts | SE (%) | Background subtracted OH/Si | Standard H2O (ppm) | Calculated H2O Content |
|---|---|---|---|---|---|---|---|---|---|---|---|---|---|---|---|---|---|---|---|
| B-CITI7210-1 | Calibrating Standard | CIT17210 | Cpx | 1 | 1 | B1 | 1.10E-03 | 4.48 | 6.92E-02 | 0.70 | 3.74E-03 | 0.86 | 1.085E-05 | 13.10 | 124075 | 0.26 | 2.16E-04 | 29 | 31 |
| B-SC3-8 | Blank | San Carlos | Olivine | 1 | 1 | B1 | 8.84E-04 | 1.00 | 8.38E-02 | 0.24 | 5.52E-05 | 6.65 | 2.253E-05 | 14.02 | 98239 | 0.31 | 0.00E+00 | 3 | 0 |
| B-PMR53-4 | Calibrating Standard | PMR-53 | Cpx | 1 | 1 | B1 | 2.94E-03 | 0.90 | 6.58E-02 | 0.34 | 5.82E-03 | 0.70 | 5.405E-05 | 4.50 | 136176 | 0.38 | 2.05E-03 | 296 | 296 |
| B-CITi7210-2 | Calibrating Standard | CIT17210 | Cpx | 1 | 2 | B1 | 1.04E-03 | 0.95 | 7.24E-02 | 0.19 | 4.91E-03 | 0.46 | 1.513E-05 | 15.66 | 114374 | 0.34 | 1.60E-04 | 29 | 23 |
| B-N106-1 | Sample | N106 | Cpx | 1 | 1 | B1 | 1.19E-02 | 1.91 | 6.56E-02 | 0.21 | 1.36E-04 | 3.50 | 0.0001964 | 3.57 | 126019 | 0.43 | 1.10E-02 |  | 1584 |
| B-N106-2 | Sample | N106 | Cpx | 2 | 1 | B1 | 1.76E-02 | 0.28 | 7.11E-02 | 0.16 | 1.82E-04 | 3.33 | 0.000409 | 1.67 | 118311 | 0.24 | 1.67E-02 |  | 2408 |
| B-EMGN7-1 | Sample | EMGN7 | Cpx | 1 | 1 | B1 | 2.68E-03 | 0.53 | 6.51E-02 | 0.25 | 6.35E-05 | 6.04 | 4.756E-05 | 8.78 | 110482 | 0.26 | 1.80E-03 |  | 259 |
| B-EMGN7-2 | Sample | EMGN7 | Cpx | 2 | 1 | B1 | 3.10E-03 | 0.79 | 6.65E-02 | 0.18 | 4.93E-05 | 8.47 | 5.529E-05 | 6.30 | 115312 | 0.54 | 2.22E-03 |  | 320 |
| B-EMGN26-1 | Sample | EMGN26 | Cpx | 1 | 1 | B1 | 9.29E-04 | 1.49 | 7.47E-02 | 0.29 | 1.61E-05 | 12.05 | 2.255E-05 | 7.89 | 99006 | 0.18 | 4.53E-05 |  | 7 |
| B-EMGN26-2 | Sample | EMGN26 | Cpx | 2 | 1 | B1 | 1.32E-03 | 1.02 | 7.54E-02 | 0.35 | 4.80E-05 | 6.54 | 0.0003656 | 19.56 | 92784 | 0.39 | 4.33E-04 |  | 62 |
| B-EMGN2-1 | Sample | EMGN2 | Cpx | 1 | 1 | B1 | 3.87E-03 | 0.57 | 7.18E-02 | 0.24 | 2.58E-05 | 8.09 | 3.028E-05 | 8.06 | 112092 | 0.67 | 2.98E-03 |  | 430 |
| B-EMGN24-1 | Sample | EMGN24 | Cpx | 1 | 1 | B2 | 3.94E-03 | 0.45 | 6.82E-02 | 0.19 | 6.47E-05 | 7.43 | 9.041E-06 | 17.86 | 109620 | 0.39 | 3.20E-03 |  | 474 |
| B-EMGN24-2 | Sample | EMGN24 | Cpx | 2 | 1 | B2 | 4.39E-03 | 0.39 | 6.74E-02 | 0.25 | 6.09E-05 | 5.23 | 2.114E-05 | 9.30 | 123450 | 0.14 | 3.65E-03 |  | 541 |
| B-MRATG13-1 | Sample | MR-ATG-13 | Cpx | 1 | 1 | B2 | 1.49E-03 | 0.96 | 6.88E-02 | 0.27 | 8.18E-04 | 2.14 | 8.253E-06 | 14.88 | 107258 | 0.39 | 7.48E-04 |  | 111 |
| B-MRATG13-2 | Sample | MR-ATG-13 | Cpx | 2 | 1 | B2 | 1.53E-03 | 1.06 | 6.96E-02 | 0.47 | 8.65E-04 | 2.13 | 6.928E-05 | 6.65 | 94975 | 0.47 | 7.94E-04 |  | 118 |
| B-N17-1 | Sample | N17 | Opx | 1 | 1 | B2 | 3.66E-03 | 0.75 | 7.83E-02 | 0.28 | 1.93E-05 | 13.40 | 3.703E-05 | 13.39 | 91819 | 0.80 | 2.92E-03 |  | 433 |
| B-N178-1 | Sample | N178 | Cpx | 1 | 1 | B2 | 2.81E-03 | 1.94 | 6.19E-02 | 0.22 | 7.08E-05 | 6.32 | 8.498E-05 | 8.31 | 123872 | 0.12 | 2.07E-03 |  | 307 |
| B-SC3-9 | Blank | San Carlos | Olivine | 1 | 2 | B2 | 7.40E-04 | 1.24 | 8.39E-02 | 0.31 | 7.83E-05 | 6.16 | 4.107E-05 | 10.49 | 97077 | 0.90 | 0.00E+00 | 3 | 0 |
| B-PMR53-5 | Calibrating Standard | PMR-53 | Cpx | 1 | 2 | B2 | 2.74E-03 | 0.84 | 6.74E-02 | 0.45 | 5.89E-03 | 0.85 | 9.081E-06 | 16.16 | 105768 | 0.60 | 2.00E-03 | 296 | 296 |
| B-CITI7210-3 | Calibrating Standard | CIT17210 | Cpx | 1 | 3 | B2 | 7.64E-04 | 0.89 | 6.75E-02 | 0.25 | 4.24E-03 | 0.75 | 9.844E-06 | 12.83 | 113142 | 0.70 | 2.37E-05 | 29 | 4 |
| B-EMGN17-1 | Sample | EMGN17 | Cpx | 1 | 1 | B2 | 7.79E-03 | 1.53 | 6.30E-02 | 0.24 | 1.24E-03 | 1.47 | 0.0002356 | 29.15 | 117702 | 0.48 | 7.05E-03 |  | 1046 |
| B-N126-1 | Sample | N126 | Cpx | 1 | 1 | B2 | 1.27E-03 | 0.98 | 6.42E-02 | 0.26 | 4.45E-05 | 6.66 | 8.264E-06 | 14.91 | 119172 | 0.78 | 5.26E-04 |  | 78 |

Sample Mount C

| Sample ID | Analytical Role | Sample ID | Phase (Identified by probe) | Grain # | Analysis # on grain | Calibration curve | OH/Si | SE (%) | 18O/Si | SE (%) | 19F/Si | SE (%) | 35Cl/Si | SE (%) | 28Si counts | SE (%) | Background subtracted OH/Si | Standard H2O (ppm) | Calculated H2O Content |
|---|---|---|---|---|---|---|---|---|---|---|---|---|---|---|---|---|---|---|---|
| C-SC3-1 | Blank | San Carlos | Olivine | 1 | 1 | C1 | 2.23E-04 | 1.57 | 9.11E-02 | 0.25 | 6.30E-05 | 4.98 | 7.413E-06 | 16.92 | 136277 | 0.48 | 0.00E+00 | 3 | 0 |
| C-PMR53-1 | Calibrating Standard | PMR-53 | Cpx | 1 | 1 | C1 | 2.69E-03 | 3.66 | 6.95E-02 | 0.13 | 6.26E-03 | 0.42 | 4.498E-06 | 14.93 | 197710 | 0.32 | 2.47E-03 | 296 | 302 |
| C-62047708-1 | Calibrating Standard | 62047-70B | Cpx | 1 | 1 | C1 | 1.06E-03 | 97.55 | 1.64E-01 | 59.06 | 5.22E-02 | 95.64 | 0.0500122 | 99.97 | 146252 | 6.88 | 8.37E-04 | 120 | 102 |
| C-EMGn7-1 | Sample | EMGN7 | Cpx | 1 | 1 | C1 | 2.96E-03 |  |  |  |  |  |  |  |  |  | 2.74E-03 |  | 334 |
| C-EMGN2-1 | Sample | EMGN2 | Cpx | 1 | 1 | C1 | 4.88E-03 | 0.39 | 7.34E-02 | 0.25 | 5.10E-05 | 5.25 | 4.364E-06 | 14.69 | 185969 | 0.15 | 4.66E-03 |  | 569 |
| c-MRATG13-1 | Sample | MR-ATG-13 | Cpx | 1 | 1 | C1 | 1.30E-03 | 0.65 | 7.09E-02 | 0.21 | 8.32E-04 | 1.57 | 3.526E-06 | 15.45 | 194072 | 0.11 | 1.08E-03 |  | 132 |
| C-EMGN24-1 | Sample | EMGN24 | Cpx | 1 | 1 | C1 | ~~1.08E-02~~ | ~~2.72~~ | ~~7.45E-02~~ | ~~0.13~~ | ~~1.10E-04~~ | ~~3.71~~ | ~~8.333E-06~~ | ~~12.60~~ | ~~173405~~ | ~~0.12~~ | ~~1.06E-02~~ |  | ~~1294~~ |
| C-EMGN26-1 | Sample | EMGN26 | Opx | 1 | 1 | C1 | 1.15E-03 | 0.82 | 7.35E-02 | 0.31 | 3.51E-05 | 11.74 | 3.799E-05 | 8.93 | 54062 | 0.14 | 9.31E-04 |  | 114 |
| C-N61-1 | Sample | N61 | Opx | 1 | 1 | C1 | 2.78E-03 | 0.54 | 7.89E-02 | 0.23 | 7.76E-05 | 6.21 | 1.926E-05 | 7.50 | 147065 | 0.28 | 2.55E-03 |  | 312 |
| C-N61-2 | Sample | N61 | Opx | 2 | 1 | C1 | 2.70E-03 | 0.52 | 8.17E-02 | 0.37 | 6.57E-05 | 4.79 | 1.769E-05 | 20.14 | 130669 | 0.32 | 2.48E-03 |  | 303 |
| C-N178-1 | Sample | N178 | Cpx | 1 | 1 | C1 | 1.96E-03 | 0.85 | 6.89E-02 | 0.36 | 3.84E-05 | 6.52 | 5.957E-05 | 5.61 | 135488 | 0.33 | 1.74E-03 |  | 213 |
| C-PMR53-2 | Calibrating Standard | PMR-53 | Cpx | 1 | 2 | C2 | 3.01E-03 | 0.71 | 7.59E-02 | 0.32 | 6.49E-03 | 0.57 | 5.193E-06 | 18.92 | 135483 | 0.37 | 2.83E-03 | 296 | 302 |
| C-SC3-2 | Blank | San Carlos | Olivine | 1 | 2 | C2 | 1.75E-04 | 2.08 | 8.91E-02 | 0.35 | 5.34E-05 | 6.11 | 5.26E-06 | 19.50 | 105753 | 0.39 | 0.00E+00 | 3 | 0 |
| C-62047708-2 | Calibrating Standard | 62047-70B | Cpx | 1 | 2 | C2 | 1.13E-03 | 1.23 | 6.63E-02 | 0.30 | 2.30E-03 | 0.84 | 2.626E-05 | 14.96 | 149719 | 0.36 | 9.55E-04 | 120 | 102 |
| C-EMGN17-1 | Sample | EMGN17 | Cpx | 1 | 1 | C2 | ~~1.14E-02~~ | ~~1.42~~ | ~~6.93E-02~~ | ~~0.20~~ | ~~1.83E-03~~ | ~~1.65~~ | ~~4.449E-05~~ | ~~5.91~~ | ~~146534~~ | ~~0.23~~ | ~~1.12E-02~~ |  | ~~1196~~ |
| C-N106-1 | Sample | N106 | Cpx | 1 | 1 | C2 | 1.02E-03 | 0.89 | 6.97E-02 | 0.23 | 3.90E-05 | 5.68 | 1.514E-05 | 7.80 | 145903 | 0.35 | 8.45E-04 |  | 90 |
| C-N126-1 | Sample | N126 | Cpx | 1 | 1 | C2 | 2.61E-02 | 0.28 | 7.36E-02 | 0.31 | 2.49E-04 | 2.98 | 0.0020103 | 0.83 | 121181 | 0.16 | 2.60E-02 |  | 2766 |
| C-N17-1 | Sample | N17 | Opx | 1 | 1 | C2 | 3.82E-03 | 0.43 | 7.99E-02 | 0.25 | 1.12E-05 | 14.45 | 1.176E-05 | 13.05 | 129431 | 0.25 | 3.65E-03 |  | 389 |
| C-N17-2 | Sample | N17 | Opx | 2 | 1 | C2 | 3.75E-03 | 0.50 | 8.16E-02 | 0.22 | 2.05E-05 | 9.91 | 3.757E-05 | 9.21 | 126053 | 0.28 | 3.57E-03 |  | 381 |
| C-PMR53-3 | Calibrating Standard | PMR-53 | Cpx | 1 | 3 | C3 | 2.99E-03 | 0.52 | 7.46E-02 | 0.17 | 6.59E-03 | 0.46 | 7.251E-06 | 10.94 | 139890 | 0.27 | 2.80E-03 | 296 | 297 |
| C-SC3-3 | Blank | San Carlos | Olivine | 1 | 3 | C3 | 1.94E-04 | 1.68 | 9.55E-02 | 0.22 | 6.26E-05 | 7.59 | 6.999E-06 | 16.39 | 108490 | 0.22 | 0.00E+00 | 3 | 0 |
| C-62047708-3 | Calibrating Standard | 62047-70B | Cpx | 1 | 3 | C3 | 1.28E-03 | 1.86 | 7.20E-02 | 1.91 | 2.61E-03 | 2.40 | 3.227E-05 | 12.50 | 137523 | 1.51 | 1.08E-03 | 120 | 115 |

Strikethrough text represent rejected analyses

Sample Mount D

| Sample ID | Analytical Role | Sample ID | Phase (Identified by probe) | Grain # | Analysis # on grain | Calibration curve | OH/Si | SE (%) | 18O/Si | SE (%) | 19F/Si | SE (%) | 35Cl/Si | SE (%) | 28Si counts | SE (%) | Background subtracted OH/Si | Standard H2O (ppm) | Calculated H2O Content |
|---|---|---|---|---|---|---|---|---|---|---|---|---|---|---|---|---|---|---|---|
| D-PMR53-1 | Secondary Standard | PMR-53 | Cpx | 1 | 1 | D1 | 2.51E-03 | 0.43 | 7.18E-02 | 0.15 | 5.94E-03 | 0.60 | 7.855E-06 | 15.91 | 119686 | 0.18 | 2.42E-03 | | 339 |
| D-SC3-1 | Blank | San Carlos | Olivine | 1 | 1 | D1 | 8.59E-05 | 2.59 | 8.60E-02 | 0.14 | 4.59E-05 | 5.75 | 6.379E-06 | 16.76 | 162681 | 0.29 | 0.00E+00 | 3 | 0 |
| D-GRR2334a-1 | Calibrating Standard | GRR2334a | Opx | 1 | 1 | D1 | 7.25E-04 | 0.97 | 7.24E-02 | 0.14 | 3.65E-04 | 1.69 | 4.712E-06 | 14.82 | 187805 | 0.20 | 6.39E-04 | 74 | 89 |
| D-GRR16506-1 | Calibrating Standard | GRR1650b | Opx | 1 | 1 | D1 | 8.43E-04 | 0.60 | 7.44E-02 | 0.20 | 2.56E-04 | 1.67 | 2.86E-06 | 19.18 | 203691 | 0.11 | 7.57E-04 | 119 | 106 |
| D-N178-1 | Sample | N178 | Opx | 1 | 1 | D1 | 2.07E-03 | 1.11 | 7.42E-02 | 0.21 | 2.88E-05 | 6.32 | 8.581E-05 | 14.87 | 197298 | 0.10 | 1.98E-03 | | 278 |
| D-EMGN29-1 | Sample | EMGN29 | Opx | 1 | 1 | D1 | 2.99E-03 | 0.59 | 7.58E-02 | 0.22 | 8.24E-06 | 10.59 | 5.621E-05 | 26.39 | 193701 | 0.18 | 2.91E-03 | | 407 |
| D-EMGN24-1 | Sample | EMGN24 | Opx | 1 | 1 | D1 | ~~1.52E-02~~ | ~~16.39~~ | ~~7.84E-02~~ | ~~0.19~~ | ~~7.83E-05~~ | ~~6.51~~ | ~~7.423E-05~~ | ~~10.53~~ | ~~159020~~ | ~~0.26~~ | ~~1.51E-02~~ | | ~~2120~~ |
| D-EMGN24-2 | Sample | EMGN24 | Opx | 2 | 1 | D1 | 4.52E-03 | 0.48 | 8.01E-02 | 0.23 | 1.79E-05 | 9.06 | 4.847E-06 | 16.28 | 151663 | 0.28 | 4.44E-03 | | 621 |
| D-EMGN24-3 | Sample | EMGN24 | Opx | 3 | 1 | D1 | 4.99E-03 | 0.70 | 7.43E-02 | 0.29 | 1.65E-05 | 8.21 | 1.289E-05 | 11.50 | 147621 | 0.18 | 4.91E-03 | | 687 |
| D-EMGN24-4 | Sample | EMGN24 | Opx | 4 | 1 | D1 | 4.05E-03 | 0.80 | 7.62E-02 | 0.19 | 2.65E-05 | 5.86 | 5.109E-06 | 17.79 | 163778 | 0.18 | 3.97E-03 | | 556 |
| D-EMGN2-1 | Sample | EMGN2 | Opx | 1 | 1 | D1 | 2.95E-03 | 6.30 | 7.56E-02 | 0.23 | 1.88E-05 | 5.92 | 8.616E-06 | 12.18 | 173626 | 0.09 | 2.87E-03 | | 402 |
| D-EMGN2-2 | Sample | EMGN2 | Opx | 2 | 1 | D1 | 2.61E-03 | 1.11 | 7.44E-02 | 0.20 | 1.68E-05 | 10.50 | 1.374E-05 | 19.46 | 170444 | 0.18 | 2.52E-03 | | 354 |
| D-EMGN7-2A | Sample | EMGN7 | Opx | 1 | 1 | D1 | 1.90E-03 | 1.04 | 6.45E-02 | 0.32 | 4.11E-05 | 10.37 | 3.562E-05 | 26.15 | 207207 | 0.27 | 1.81E-03 | | 254 |
| D-EMGN7-2B RIM | Sample | EMGN7 | Opx | 1 | 2 | D1 | 2.03E-03 | 0.64 | 6.47E-02 | 0.17 | 1.35E-05 | 10.50 | 5.019E-06 | 17.67 | 212423 | 0.20 | 1.93E-03 | | 270 |
| D-EMGN7-3 | Sample | EMGN7 | Opx | 2 | 1 | D1 | 2.44E-03 | 0.41 | 6.86E-02 | 0.12 | 1.81E-05 | 11.04 | 7.577E-06 | 10.14 | 183691 | 0.14 | 2.34E-03 | | 328 |
| D-MRATG13-1 | Sample | EMGN7 | Opx | 1 | 1 | D2 | 9.03E-04 | 0.74 | 7.29E-02 | 0.20 | 1.19E-04 | 4.52 | 1.638E-05 | 9.70 | 152982 | 0.14 | 8.01E-04 | | 94 |
| D-EMGN14-1 | Sample | EMGN14 | Opx | 1 | 1 | D2 | 2.08E-03 | 0.84 | 6.41E-02 | 0.24 | 3.50E-05 | 11.48 | 1.661E-05 | 16.16 | 57964 | 0.08 | 1.98E-03 | | 233 |
| D-EMGN14-2 | Sample | EMGN14 | Opx | 2 | 1 | D2 | 2.56E-03 | 0.47 | 7.79E-02 | 0.28 | 1.67E-05 | 8.28 | 9.425E-06 | 12.47 | 121094 | 0.24 | 2.45E-03 | | 289 |
| D-PMR53-2 | Secondary Standard | PMR-53 | Cpx | 1 | 2 | D2 | 2.73E-03 | 0.50 | 7.38E-02 | 0.38 | 6.05E-03 | 0.78 | 7.714E-06 | 19.24 | 82243 | 0.26 | 2.62E-03 | | 309 |
| D-SC3-2 | Blank | San Carlos | Olivine | 1 | 2 | D2 | 1.02E-04 | 1.83 | 9.64E-02 | 0.20 | 5.43E-05 | 5.59 | 1.109E-05 | 13.51 | 116736 | 0.25 | 0.00E+00 | 3 | 0 |
| D-GRR2334A-2 | Calibrating Standard | GRR2334a | Opx | 1 | 2 | D2 | 9.35E-04 | 0.82 | 8.50E-02 | 0.15 | 4.36E-04 | 2.39 | 3.21E-06 | 15.48 | 134130 | 0.24 | 8.33E-04 | 74 | 98 |
| D-GRR16506-3 | Calibrating Standard | GRR1650b | Opx | 1 | 2 | D2 | 9.00E-04 | 12.95 | 8.54E-02 | 0.22 | 9.37E-04 | 23.29 | 1.186E-05 | 23.25 | 138360 | 0.14 | 7.98E-04 | 119 | 94 |
| D-EMGN19-1 | Sample | EMGN19 | Opx | 1 | 1 | D2 | 2.18E-03 | 0.63 | 7.24E-02 | 0.17 | 1.29E-04 | 3.45 | 5.519E-06 | 14.02 | 151305 | 0.21 | 2.08E-03 | | 245 |
| D-N55-1 | Sample | N55 | Opx | 1 | 1 | D3 | 2.97E-03 | 1.66 | 8.16E-02 | 0.20 | 3.38E-05 | 7.56 | 2.215E-05 | 28.56 | 114802 | 0.16 | 2.88E-03 | | 357 |
| D-N55-2 | Sample | N55 | Opx | 2 | 1 | D3 | 3.58E-03 | 0.98 | 7.99E-02 | 0.20 | 4.62E-05 | 6.35 | 3.193E-05 | 7.21 | 150695 | 0.15 | 3.49E-03 | | 433 |
| D-N53-1 | Sample | N53 | Opx | 1 | 1 | D3 | 2.93E-03 | 0.47 | 7.89E-02 | 0.14 | 5.62E-05 | 4.87 | 4.64E-06 | 16.29 | 147355 | 0.18 | 2.84E-03 | | 353 |
| D-N53-2 | Sample | N53 | Opx | 2 | 1 | D3 | 3.50E-03 | 0.33 | 8.06E-02 | 0.32 | 9.91E-05 | 3.17 | 6.233E-06 | 12.04 | 154423 | 0.10 | 3.41E-03 | | 423 |
| D-N126-1 | Sample | N126 | Opx | 1 | 1 | D3 | 1.04E-03 | 0.89 | 8.39E-02 | 0.19 | 1.83E-05 | 12.22 | 2.536E-05 | 12.14 | 135587 | 0.15 | 9.48E-04 | | 118 |
| D-N126-2 | Sample | N126 | Opx | 2 | 1 | D3 | 1.10E-03 | 2.11 | 8.08E-02 | 0.19 | 2.00E-05 | 6.87 | 3.836E-05 | 20.20 | 144535 | 0.16 | 1.01E-03 | | 126 |
| D-EMGN21-1 | Sample | EMGN21 | Opx | 1 | 1 | D3 | ~~7.25E-03~~ | ~~4.61~~ | ~~8.34E-02~~ | ~~0.22~~ | ~~7.59E-05~~ | ~~6.14~~ | ~~6.957E-06~~ | ~~12.45~~ | ~~116750~~ | ~~0.38~~ | ~~7.16E-03~~ | | ~~888~~ |
| D-EMGN17-1 | Sample | EMGN17 | Opx | 1 | 1 | D3 | 6.33E-04 | 0.76 | 7.12E-02 | 0.19 | 3.34E-05 | 5.44 | 4.539E-06 | 10.65 | 178901 | 0.23 | 5.43E-04 | | 67 |
| D-SC3-3 | Blank | San Carlos | Olivine | 1 | 3 | D3 | 8.94E-05 | 3.32 | 9.57E-02 | 0.19 | 5.06E-05 | 7.03 | 6.526E-06 | 16.59 | 124094 | 0.16 | 0.00E+00 | 3 | 0 |
| D-PMR53-3 | Secondary Standard | PMR-53 | Cpx | 1 | 3 | D3 | 2.28E-03 | 0.41 | 6.58E-02 | 0.24 | 5.39E-03 | 0.71 | 1.008E-05 | 16.27 | 130630 | 0.30 | 2.19E-03 | | 271 |
| D-GRR2334A-3 | Calibrating Standard | GRR2334a | Opx | 1 | 3 | D3 | 8.11E-04 | 1.06 | 7.97E-02 | 0.52 | 4.00E-04 | 1.70 | 7.884E-06 | 14.11 | 106395 | 0.56 | 7.21E-04 | 74 | 89 |
| D-GRR16506-4 | Calibrating Standard | GRR1650b | Opx | 1 | 3 | D3 | 9.44E-04 | 1.19 | 8.00E-02 | 0.17 | 2.86E-04 | 2.42 | 7.249E-06 | 14.72 | 132872 | 0.24 | 8.54E-04 | 119 | 106 |

Strikethough text represent rejected analyses

Sample Mount E

| Sample ID | Analytical Role | Sample ID | Phase (Identified by probe) | Grain # | Analysis # on grain | Calibration curve | OH/Si | SE (%) | 18O/Si | SE (%) | 19F/Si | SE (%) | 35Cl/Si | SE (%) | 28Si counts | SE (%) | Background subtracted OH/Si | Standard H2O (ppm) | Calculated H2O Content |
|---|---|---|---|---|---|---|---|---|---|---|---|---|---|---|---|---|---|---|---|
| EMGN29opx-E1a | Sample | EMGN29 | Opx | 1 | 1 | E1 | 2.35E-03 | 1.30 | 7.23E-02 | 0.36 | 1.51E-05 | 15.61 | 2.265E-05 | 17.08 | 40394 | 0.26 | 2.24E-03 |  | 287 |
| N178opx-E1a | Sample | N178 | Opx | 1 | 1 | E1 | ~~3.97E-01~~ | ~~22.77~~ | ~~8.19E-02~~ | ~~5.02~~ | ~~1.49E-03~~ | ~~23.76~~ | ~~0.0040326~~ | ~~26.22~~ | ~~36039~~ | ~~5.65~~ | ~~3.97E-01~~ |  | ~~50904~~ |
| N178opx-E1b | Sample | N178 | Opx | 1 | 2 | E1 | 1.70E-03 | 2.36 | 8.00E-02 | 0.60 | 1.10E-04 | 5.00 | 3.378E-05 | 17.19 | 40620 | 0.46 | 1.59E-03 |  | 203 |
| EMGN2opx-E2a | Sample | EMGN2 | Opx | 2 | 1 | E1 | 3.32E-03 | 4.96 | 6.98E-02 | 0.46 | 2.11E-05 | 16.47 | 2.979E-05 | 14.74 | 46828 | 0.19 | 3.21E-03 |  | 411 |
| EMGN2opx-E1a | Sample | EMGN2 | Opx | 1 | 1 | E1 | 2.45E-03 | 1.32 | 7.00E-02 | 0.43 | 1.93E-05 | 18.50 | 2.706E-05 | 13.79 | 45943 | 0.26 | 2.34E-03 |  | 300 |
| Sancarlos-E1b | Blank | San Carlos | Olivine | 1 | 1 | E1 | 1.12E-04 | 4.33 | 7.69E-02 | 0.26 | 4.58E-05 | 8.10 | 3.684E-05 | 12.67 | 47671 | 0.33 | 0.00E+00 | 3 | 0 |
| EMGN24opx-E2a | Sample | EMGN24 | Opx | 2 | 1 | E1 | 3.83E-03 | 1.22 | 8.05E-02 | 0.99 | 2.24E-05 | 20.27 | 2.114E-05 | 21.65 | 39040 | 1.13 | 3.72E-03 |  | 477 |
| EMGN24opx-E1a | Sample | EMGN24 | Opx | 1 | 1 | E1 | 4.79E-03 | 2.35 | 6.65E-02 | 0.28 | 2.35E-05 | 15.49 | 9.333E-06 | 19.64 | 51874 | 0.37 | 4.68E-03 |  | 599 |
| MRATG13opx-E1a | Sample | MR-ATG-13 | Opx | 1 | 1 | E1 | 6.35E-04 | 64.66 | 6.59E-02 | 8.34 | 1.10E-04 | 11.86 | 2.808E-05 | 33.18 | 47847 | 5.94 | 5.22E-04 |  | 67 |
| MRATG13opx-E1b | Sample | MR-ATG-13 | Opx | 1 | 2 | E1 | 8.14E-04 | 24.65 | 7.00E-02 | 14.05 | 1.13E-04 | 8.54 | 6.097E-05 | 10.06 | 46485 | 5.58 | 7.02E-04 |  | 90 |
| EMGN7opx-E1a | Sample | EMGN7 | Opx | 1 | 1 | E1 | 2.43E-03 | 0.89 | 6.50E-02 | 0.26 | 1.67E-05 | 15.01 | 1.516E-05 | 14.39 | 51847 | 0.34 | 2.31E-03 |  | 296 |
| EMGN7opx-E2a | Sample | EMGN7 | Opx | 2 | 1 | E1 | 1.98E-03 | 1.36 | 6.55E-02 | 0.30 | 2.39E-05 | 20.21 | 3.5E-05 | 16.51 | 48707 | 0.31 | 1.87E-03 |  | 239 |
| EMGN19opx-E1a | Sample | EMGN19 | Opx | 1 | 1 | E1 | 1.09E-03 | 1.50 | 6.67E-02 | 0.39 | 6.57E-05 | 9.63 | 1.79E-05 | 19.05 | 43879 | 0.39 | 9.91E-04 |  | 127 |
| EMGN14opx-E2a | Sample | EMGN14 | Opx | 2 | 1 | E1 | 2.78E-03 | 0.82 | 6.82E-02 | 0.30 | 1.21E-05 | 18.86 | 1.678E-05 | 18.98 | 48319 | 0.22 | 2.68E-03 |  | 343 |
| EMGN14opx-E1a | Sample | EMGN14 | Opx | 1 | 1 | E1 | 2.34E-03 | 8.94 | 6.60E-02 | 1.88 | 1.60E-05 | 17.38 | 3.837E-05 | 14.53 | 51656 | 0.60 | 2.23E-03 |  | 286 |
| EMGN14opx-E1b | Sample | EMGN14 | Opx | 1 | 2 | E1 | ~~5.11E-02~~ | ~~8.24~~ | ~~6.69E-02~~ | ~~0.41~~ | ~~1.60E-04~~ | ~~13.26~~ | ~~0.0001517~~ | ~~10.65~~ | ~~51595~~ | ~~0.24~~ | ~~5.10E-02~~ |  | ~~6531~~ |
| EMGN14opx-E1c | Sample | EMGN14 | Opx | 1 | 3 | E1 | 2.69E-03 | 0.65 | 6.59E-02 | 0.28 | 1.53E-05 | 15.03 | 5.698E-05 | 10.32 | 53936 | 0.31 | 2.59E-03 |  | 331 |
| SanCarlos-E1c | Blank | San Carlos | Olivine | 1 | 2 | E1 | 1.02E-04 | 3.59 | 7.78E-02 | 0.29 | 5.84E-05 | 9.11 | 4.704E-05 | 11.42 | 46465 | 0.18 | 0.00E+00 | 3 | 0 |
| PMR53-E1b | Secondary Standard | PMR-53 | Cpx | 1 | 1 | E1 | 2.01E-03 | 1.27 | 6.33E-02 | 1.23 | 4.91E-03 | 0.82 | 3.176E-05 | 13.10 | 52507 | 0.30 | 1.91E-03 |  | 245 |
| PMR53-E1c | Secondary Standard | PMR-53 | Cpx | 1 | 2 | E1 | 1.95E-03 | 0.78 | 6.18E-02 | 0.23 | 4.78E-03 | 1.19 | 2.367E-05 | 8.89 | 56373 | 0.39 | 1.84E-03 |  | 236 |
| JLM50-E1c | Calibrating Standard | JLM-50 | Opx | 1 | 1 | E1 | 4.16E-04 | 2.04 | 6.94E-02 | 0.19 | 4.59E-04 | 2.84 | 0.0001147 | 9.05 | 63261 | 0.33 | 3.15E-04 | 36 | 40 |
| GRR2334a-E1b | Calibrating Standard | GRR2334a | Opx | 1 | 1 | E1 | 6.61E-04 | 1.73 | 6.77E-02 | 0.59 | 3.05E-04 | 2.84 | 3.289E-05 | 7.48 | 66219 | 0.51 | 5.59E-04 | 74 | 72 |
| SanCarlos-E1d | Blank | San Carlos | Olivine | 1 | 3 | E1 | 1.19E-04 | 3.23 | 7.63E-02 | 0.37 | 5.48E-05 | 8.21 | 4.26E-05 | 9.11 | 62930 | 0.25 | 1.72E-05 | 3 | 2 |

Strikethrough text represents rejected analyses

Sample Mount F

| Sample ID | Analytical Role | Sample ID | Phase (Identified by probe) | Grain # | Analysis # on grain | Calibration curve | OH/Si | SE (%) | 18O/Si | SE (%) | 19F/Si | SE (%) | 35Cl/Si | SE (%) | 28Si counts | SE (%) | Background subtracted OH/Si | Standard H2O (ppm) | Calculated H2O Content |
|---|---|---|---|---|---|---|---|---|---|---|---|---|---|---|---|---|---|---|---|
| JLM77-F1a | Calibrating Standard | JLM-77 | Cpx | 1 | 1 | F1 | 1.75E-03 | 0.46 | 5.87E-02 | 0.20 | 1.51E-02 | 0.46 | 4.634E-05 | 8.68 | 128160 | 0.64 | 1.44E-03 | 217 | 218 |
| GRR2334a-F1a | Calibrating Standard | GRR2334a | Opx | 1 | 1 | F1 | 7.83E-04 | 1.08 | 6.05E-02 | 0.18 | 3.22E-04 | 1.98 | 2.059E-05 | 8.61 | 138036 | 0.58 | 4.73E-04 | 74 | 72 |
| Sancarlos-F2b | Blank | San Carlos | Olivine | 1 | 1 | F1 | 3.10E-04 | 3.46 | 7.88E-02 | 0.25 | 6.04E-05 | 4.80 | 5.579E-06 | 19.86 | 126931 | 0.46 | 0.00E+00 | 3 | 0 |
| N61-F1a | Sample | N61 | Cpx | 1 | 1 | F1 | 3.37E-03 | 0.60 | 5.68E-02 | 0.52 | 4.42E-04 | 1.94 | 5.125E-05 | 5.30 | 130068 | 0.61 | 3.07E-03 |  | 464 |
| N61-F2a | Sample | N61 | Mixed Cpx/Opx | 2 | 1 | F1 | ~~2.16E-03~~ | ~~0.52~~ | ~~5.92E-02~~ | ~~0.23~~ | ~~2.54E-04~~ | ~~2.97~~ | ~~3.844E-05~~ | ~~7.96~~ | ~~119382~~ | ~~0.65~~ | ~~1.85E-03~~ |  | ~~280~~ |
| N53cpx-F2a | Sample | N53 | Cpx | 2 | 1 | F1 | 2.34E-03 | 0.92 | 5.98E-02 | 0.51 | 1.41E-04 | 4.06 | 7.549E-05 | 5.00 | 108164 | 0.69 | 2.03E-03 |  | 308 |
| N53cpx-F2b | Sample | N53 | Cpx | 2 | 2 | F1 | 2.45E-03 | 0.85 | 6.13E-02 | 0.24 | 1.60E-04 | 3.77 | 6.274E-05 | 6.39 | 101409 | 0.63 | 2.14E-03 |  | 324 |
| N53cpx-F1a | Sample | N53 | Cpx | 1 | 1 | F1 | 2.43E-03 |  |  |  |  |  |  |  |  |  | 2.12E-03 |  | 321 |
| EMGn26-F1a | Sample | EMGN26 | Cpx | 1 | 1 | F1 | 4.27E-04 | 1.53 | 5.64E-02 | 0.15 | 2.49E-05 | 9.66 | 1.33E-05 | 13.72 | 119158 | 0.70 | 1.92E-04 |  | 29 |
| EMGn26-F1b | Sample | EMGN26 | Cpx | 1 | 2 | F1 | 4.47E-04 | 1.39 | 5.78E-02 | 0.30 | 2.25E-05 | 9.40 | 4.446E-05 | 7.03 | 117396 | 0.77 | 2.13E-04 |  | 32 |
| EMGN26-F1b-c | Sample | EMGN26 | Cpx | 1 | 3 | F1 | 6.33E-04 | 5.00 | 5.77E-02 | 0.54 | 1.65E-05 | 10.82 | 0.0003365 | 27.04 | 118979 | 0.93 | 3.98E-04 |  | 60 |
| EMGN26-F2a | Sample | EMGN26 | Cpx | 2 | 1 | F1 | 4.55E-04 | 1.36 | 5.60E-02 | 0.39 | 2.51E-05 | 8.29 | 3.412E-05 | 12.36 | 124858 | 0.72 | 2.21E-04 |  | 33 |
| Sancarlos-F2c | Blank | San Carlos | Olivine | 2 | 2 | F1 | 2.35E-04 | 3.06 | 7.00E-02 | 0.67 | 7.35E-05 | 5.58 | 1.904E-05 | 11.17 | 112875 | 0.84 | 0.00E+00 |  | 0 |
| EMGN26-F2b | Sample | EMGN26 | Cpx | 2 | 2 | F1 | 5.68E-04 | 1.45 | 5.78E-02 | 0.31 | 2.18E-05 | 9.27 | 1.412E-05 | 16.39 | 124053 | 0.68 | 3.34E-04 |  | 51 |
| EMGN29cpx-F1a | Sample | EMGN29 | Opx | 1 | 1 | F2 | 3.52E-03 | 3.66 | 5.83E-02 | 4.57 | 1.96E-05 | 8.39 | 3.499E-05 | 12.88 | 132627 | 1.09 | 3.28E-03 |  | 502 |
| EMGN29cpx-F1b | Sample | EMGN29 | Opx | 1 | 2 | F2 | 3.46E-03 | 0.62 | 6.26E-02 | 0.15 | 1.77E-05 | 8.71 | 3.435E-05 | 12.68 | 133421 | 0.54 | 3.23E-03 |  | 493 |
| JLM77-F1b | Calibrating Standard | JLM-77 | Cpx | 1 | 2 | F2 | 1.66E-03 | 0.78 | 5.77E-02 | 0.27 | 1.48E-02 | 0.30 | 4.688E-05 | 16.39 | 126599 | 0.74 | 1.42E-03 | 217 | 218 |
| PMR53-F3b | Secondary Standard | PMR-53 | Cpx | 3 | 1 | F2 | 2.43E-03 | 0.65 | 5.62E-02 | 0.16 | 5.37E-03 | 0.63 | 2.705E-05 | 5.80 | 165930 | 0.51 | 2.20E-03 |  | 336 |
| SanCarlos-F2d | Blank | San Carlos | Olivine | 2 | 3 | F2 | ~~6.90E-04~~ | ~~34.31~~ | ~~7.00E-02~~ | ~~2.16~~ | ~~6.55E-05~~ | ~~4.83~~ | ~~4.62E-05~~ | ~~12.91~~ | ~~115759~~ | ~~1.80~~ |  |  |  |
| SanCarlos-F2e | Blank | San Carlos | Olivine | 2 | 4 | F2 | 2.34E-04 | 4.89 | 7.18E-02 | 0.22 | 4.41E-05 | 5.28 | 2.677E-05 | 11.55 | 120222 | 0.65 | 0.00E+00 | 3 | 0 |
| GRR2334a-F1b | Calibrating Standard | GRR2334a | Opx | 1 | 2 | F2 | 7.05E-04 | 1.60 | 6.11E-02 | 0.21 | 2.88E-04 | 4.53 | 2.107E-05 | 14.78 | 82071 | 0.68 | 4.71E-04 | 74 | 72 |
| Sancarlos-F2f | Blank | San Carlos | Olivine | 2 | 5 | F3 | 2.01E-04 | 2.91 | 7.30E-02 | 0.23 | 6.98E-05 | 7.48 | 7.133E-06 | 28.64 | 69562 | 0.44 | 0.00E+00 | 3 | 0 |
| GRR2334a-F1c | Calibrating Standard | GRR2334a | Opx | 1 | 3 | F3 | 7.04E-04 | 1.40 | 6.25E-02 | 0.26 | 2.98E-04 | 3.85 | 1.378E-05 | 17.01 | 75289 | 0.45 | 5.03E-04 | 74 | 79 |
| JLM77-F1c | Calibrating Standard | JLM-77 | Cpx | 1 | 3 | F3 | 1.58E-03 | 0.87 | 6.01E-02 | 0.27 | 1.43E-02 | 0.41 | 2.743E-05 | 15.82 | 70831 | 0.52 | 1.38E-03 | 217 | 215 |
| PMR53-F3c | Secondary Standard | PMR-53 | Cpx | 3 | 3 | F3 | 2.11E-03 | 0.71 | 5.47E-02 | 0.20 | 4.88E-03 | 0.63 | 2.299E-05 | 10.40 | 118314 | 0.38 | 1.91E-03 |  | 299 |
| EMGN29cpx-F1a-duplicate | Sample | EMGN29 | Opx | 1 | 3 | F3 | 3.40E-03 | 0.62 | 6.24E-02 | 0.17 | 1.79E-05 | 8.92 | 4.222E-05 | 8.79 | 102530 | 0.38 | 3.20E-03 |  | 500 |
| EMGN29cpx-F1c | Sample | EMGN29 | Cpx | 1 | 4 | F3 | 3.42E-03 | 0.55 | 6.23E-02 | 0.22 | 1.56E-05 | 12.51 | 2.596E-05 | 11.19 | 104261 | 0.49 | 3.22E-03 |  | 503 |
| EMGN29cpx-F2a | Sample | EMGN29 | Cpx | 2 | 1 | F4 | 1.28E-02 | 0.45 | 5.53E-02 | 0.21 | 1.93E-05 | 10.23 | 1.849E-05 | 11.23 | 106157 | 0.53 | 1.26E-02 |  | 1986 |
| N17-F2a | Sample | N17 | Cpx | 2 | 1 | F4 | 1.74E-02 | 0.25 | 5.58E-02 | 0.19 | 7.23E-05 | 6.13 | 0.0048824 | 0.86 | 101875 | 0.45 | 1.72E-02 |  | 2711 |
| N17-F1a | Sample | N17 | Cpx | 1 | 1 | F4 | 1.42E-02 | 0.49 | 5.67E-02 | 0.35 | 5.68E-05 | 5.64 | 0.0041212 | 0.92 | 99677 | 0.57 | 1.40E-02 |  | 2203 |
| MRATG13-F3a-rerun | Sample | MR-ATG-13 | Cpx | 3 | 1 | F4 | 1.04E-03 | 0.83 | 5.31E-02 | 0.20 | 6.74E-04 | 2.14 | 6.32E-05 | 6.67 | 103951 | 0.65 | 8.02E-04 |  | 126 |
| MRATG13-F2a-rerun | Sample | MR-ATG-13 | Cpx | 2 | 1 | F4 | 1.03E-03 | 0.71 | 5.61E-02 | 0.21 | 6.43E-04 | 1.25 | 4.664E-05 | 7.91 | 104574 | 0.51 | 7.91E-04 |  | 125 |
| MRATG13-F1a-rerun | Sample | MR-ATG-13 | Cpx | 1 | 1 | F4 | 1.04E-03 | 0.89 | 5.55E-02 | 0.22 | 6.81E-04 | 1.37 | 5.65E-05 | 9.53 | 103880 | 0.40 | 7.95E-04 |  | 125 |
| N106opx-F2a | Sample | N106 | Opx | 2 | 1 | F4 | 2.86E-03 | 0.58 | 6.36E-02 | 0.21 | 2.38E-05 | 7.49 | 6.579E-05 | 8.90 | 99681 | 0.71 | 2.61E-03 |  | 412 |
| N106opx-F2b | Sample | N106 | Opx | 2 | 2 | F4 | 2.83E-03 | 0.93 | 6.26E-02 | 0.17 | 2.41E-05 | 11.37 | 7.423E-05 | 15.58 | 102516 | 0.53 | 2.59E-03 |  | 408 |
| N106opx-F2c | Sample | N106 | Opx | 2 | 3 | F4 | 3.02E-03 | 1.44 | 6.19E-02 | 0.28 | 2.28E-05 | 9.94 | 9.223E-05 | 11.04 | 99544 | 0.65 | 2.78E-03 |  | 438 |
| N106opx-F1a | Sample | N106 | Opx | 1 | 1 | F4 | 2.96E-03 | 0.90 | 6.21E-02 | 0.22 | 2.58E-05 | 6.61 | 0.0001182 | 7.92 | 101281 | 0.40 | 2.72E-03 |  | 429 |
| Sancarlos-F2g | Blank | San Carlos | Olivine | 2 | 6 | F4 | 2.41E-04 | 1.20 | 7.11E-02 | 0.21 | 6.14E-05 | 6.94 | 8.88E-05 | 10.04 | 82795 | 0.52 | 0.00E+00 | 3 | 0 |
| GRR2334a-F1d | Calibrating Standard | GRR2334a | Opx | 1 | 4 | F4 | 7.83E-04 | 1.41 | 6.18E-02 | 0.20 | 3.38E-04 | 1.40 | 7.249E-05 | 8.42 | 101011 | 0.46 | 5.42E-04 | 74 | 85 |
| JLM77-F1d | Calibrating Standard | JLM-77 | Cpx | 1 | 4 | F4 | 1.59E-03 | 0.53 | 5.80E-02 | 0.21 | 1.43E-02 | 0.41 | 2.845E-05 | 10.57 | 98376 | 0.42 | 1.35E-03 | 217 | 212 |
| PMR53-F3d | Secondary Standard | PMR-53 | Cpx | 3 | 4 | F4 | 2.24E-03 | 0.53 | 5.54E-02 | 0.19 | 5.14E-03 | 0.40 | 4.77E-05 | 7.85 | 121208 | 0.62 | 2.00E-03 |  | 316 |

Strikethrough text represents rejected analyses

Sample Mount G

| Sample ID | Analytical Role | Sample ID | Phase (Identified by probe) | Grain # | Analysis # on grain | Calibration curve | OH/Si | SE (%) | 18O/Si | SE (%) | 19F/Si | SE (%) | 35Cl/Si | SE (%) | 28Si counts | SE (%) | Background subtracted OH/Si | Standard H2O (ppm) | Calculated H2O Content |
|---|---|---|---|---|---|---|---|---|---|---|---|---|---|---|---|---|---|---|---|
| PMR-53-G3a | Secondary Standard | PMR-53 | Cpx | 1 | 1 | G1 | 2.23E-03 | 0.87 | 6.47E-02 | 0.23 | 5.09E-03 | 0.89 | 0 | 0.00 | 43922 | 0.48 | 2.07E-03 | | 314 |
| SanCarlos-G1a | Blank | San Carlos | Olivine | 1 | 1 | G1 | 1.62E-04 | 2.93 | 7.89E-02 | 0.42 | 3.35E-05 | 11.70 | 1.385E-07 | 161.58 | 40713 | 1.63 | 0.00E+00 | 3 | 0 |
| JLM77-G1a | Calibrating Standard | JLM-77 | Cpx | 1 | 1 | G1 | 1.59E-03 | 1.60 | 6.84E-02 | 0.19 | 1.47E-02 | 0.79 | 0 | 0.00 | 42455 | 0.38 | 1.43E-03 | 217 | 218 |
| GRR2334a-G1a | Calibrating Standard | GRR2334a | Opx | 1 | 1 | G1 | 6.35E-04 | 1.91 | 6.91E-02 | 0.27 | 2.82E-04 | 4.61 | 0 | 0.00 | 46034 | 0.22 | 4.73E-04 | 74 | 72 |
| N106opx-G1a | Sample | N106 | Opx | 1 | 1 | G1 | 7.90E-03 | 1.46 | 6.81E-02 | 0.20 | 5.79E-05 | 8.80 | 0.0003339 | 2.54 | 51142 | 0.21 | 7.73E-03 | | 1177 |
| N106opx-G1b | Sample | N106 | Opx | 1 | 2 | G1 | 3.17E-03 | 1.28 | 6.96E-02 | 0.39 | 1.67E-05 | 17.53 | 3.133E-05 | 18.14 | 51232 | 0.26 | 3.00E-03 | | 457 |
| N106opx-G1c | Sample | N106 | Opx | 1 | 3 | G1 | 3.64E-03 | 0.95 | 6.93E-02 | 0.05 | 1.74E-05 | 16.24 | 5.327E-05 | 11.98 | 50957 | 0.48 | 3.48E-03 | | 530 |
| N106opx-G1d | Sample | N106 | Opx | 1 | 4 | G1 | 3.07E-03 | 1.30 | 6.87E-02 | 0.27 | 1.80E-05 | 10.46 | 9.212E-05 | 8.63 | 52969 | 0.20 | 2.91E-03 | | 443 |
| N106opx-G1e | Sample | N106 | Opx | 1 | 5 | G1 | 1.78E-03 | 0.68 | 6.67E-02 | 0.35 | 1.41E-05 | 13.37 | 4.885E-05 | 31.04 | 57414 | 0.81 | 1.62E-03 | | 246 |
| N106opx-G2 | Sample | N106 | Opx | 2 | 1 | G1 | 2.48E-03 | 0.91 | 6.80E-02 | 0.27 | 8.35E-06 | 17.89 | 1.463E-05 | 20.14 | 53857 | 0.15 | 2.31E-03 | | 352 |
| EMGn29cpx-G2a | Sample | EMGN29 | Cpx | 2 | 1 | G1 | 2.39E-02 | 1.95 | 6.29E-02 | 0.24 | 1.84E-05 | 14.45 | 0.0010032 | 4.00 | 53571 | 0.10 | 2.38E-02 | | 3617 |
| EMGn29cpx-G1a | Sample | EMGN29 | Cpx | 1 | 1 | G1 | 2.17E-02 | | | | 1.92E-05 | | | | | | 2.15E-02 | | 3273 |
| EMGN14cpx-G1b | Sample | EMGN14 | Olivine | 1 | 2 | G1 | 2.14E-04 | 3.87 | 7.57E-02 | 0.30 | 1.95E-05 | 11.97 | 5.789E-06 | 30.84 | 47954 | 0.22 | 5.21E-05 | | 8 |
| EMGN14cpx-G1a | Sample | EMGN14 | Amphibole | 1 | 1 | G1 | ~~1.47E-01~~ | ~~0.19~~ | ~~6.85E-02~~ | ~~0.42~~ | ~~4.63E-04~~ | ~~2.41~~ | ~~0.0006373~~ | ~~2.82~~ | ~~44394~~ | ~~0.44~~ | ~~1.47E-01~~ | | ~~22304~~ |
| EMGN26-G1a | Sample | EMGN26 | Cpx | 1 | 1 | G1 | 3.50E-04 | 1.78 | 6.33E-02 | 0.28 | 8.57E-06 | 27.98 | 3.742E-05 | 10.70 | 49357 | 0.37 | 1.88E-04 | | 29 |
| EMGN26-G2a | Sample | EMGN26 | Cpx | 2 | 1 | G1 | 5.08E-04 | 2.57 | 6.37E-02 | 0.22 | 1.80E-05 | 15.89 | 1.145E-05 | 20.69 | 49030 | 0.21 | 3.46E-04 | | 53 |
| N17cpx-G2a | Sample | N17 | Cpx | 2 | 1 | G1 | 9.94E-03 | 9.19 | 6.63E-02 | 0.37 | 3.47E-05 | 19.84 | 0.00015 | 17.24 | 45237 | 0.56 | 9.78E-03 | | 1489 |
| N17cpx-G1a | Sample | N17 | Cpx | 1 | 1 | G2 | 7.95E-03 | 0.93 | 6.50E-02 | 0.24 | 3.11E-05 | 11.60 | 0.0002763 | 3.62 | 45675 | 0.28 | 7.82E-03 | | 1263 |
| EMGN21-G1a | Sample | EMGN21 | Cpx | 1 | 1 | G2 | 5.37E-03 | 0.74 | 6.45E-02 | 0.27 | 4.31E-04 | 3.71 | 0.0001072 | 8.96 | 46989 | 0.16 | 5.24E-03 | | 847 |
| EMGN21-G2a | Sample | EMGN21 | Cpx | 2 | 1 | G2 | 2.65E-03 | 2.01 | 6.35E-02 | 0.21 | 1.66E-04 | 6.50 | 4.141E-05 | 18.84 | 46776 | 0.32 | 2.53E-03 | | 409 |
| N106cpx-G3a-reruns | Sample | N106 | Mixed-cpx/opx | 3 | 1 | G2 | ~~7.90E-04~~ | ~~1.88~~ | ~~7.33E-02~~ | ~~1.04~~ | ~~3.53E-05~~ | ~~17.14~~ | ~~3.488E-05~~ | ~~16.05~~ | ~~38570~~ | ~~0.65~~ | ~~6.67E-04~~ | | ~~108~~ |
| N106cpx-G2a | Sample | N106 | Cpx | 2 | 1 | G2 | 1.16E-02 | 0.48 | 7.32E-02 | 0.34 | 1.24E-04 | 6.51 | 7.84E-05 | 6.99 | 39737 | 0.08 | 1.15E-02 | | 1851 |
| N106cpx-G1a | Sample | N106 | Cpx | 1 | 1 | G2 | 1.28E-02 | 0.43 | 7.34E-02 | 1.09 | 1.26E-04 | 7.93 | 0.000405 | 4.23 | 38788 | 0.20 | 1.27E-02 | | 2055 |
| N61-G1a | Sample | N61 | Cpx | 1 | 1 | G2 | 2.21E-03 | 0.95 | 6.88E-02 | 0.29 | 2.83E-04 | 4.58 | 3.957E-05 | 10.78 | 46178 | 0.27 | 2.09E-03 | | 337 |
| N61-G2a | Sample | N61 | Cpx | 2 | 1 | G2 | 2.46E-03 | 2.11 | 7.09E-02 | 0.27 | 4.11E-04 | 3.56 | 0.0001991 | 21.06 | 42531 | 0.17 | 2.34E-03 | | 377 |
| N53-G2a | Sample | N53 | see note | 2 | 1 | G2 | ~~2.66E-03~~ | ~~1.02~~ | ~~6.89E-02~~ | ~~0.24~~ | ~~3.69E-04~~ | ~~4.83~~ | ~~1.936E-05~~ | ~~15.34~~ | ~~41896~~ | ~~0.11~~ | ~~2.54E-03~~ | | ~~410~~ |
| N53-G1a | Sample | N53 | Cpx | 1 | 1 | G2 | 2.92E-03 | 0.92 | 7.18E-02 | 0.30 | 2.00E-04 | 5.92 | 2.583E-05 | 16.28 | 37382 | 0.30 | 2.79E-03 | | 451 |
| PMR-53-G3b | Secondary Standard | PMR-53 | Cpx | 1 | 2 | G2 | 2.07E-03 | 0.93 | 6.35E-02 | 0.33 | 4.97E-03 | 1.21 | 3.234E-05 | 11.67 | 54852 | 0.20 | 1.94E-03 | | 314 |
| San Carlos-G1b | Blank | San Carlos | Olivine | 1 | 2 | G2 | 1.23E-04 | 6.42 | 7.94E-02 | 3.32 | 4.38E-05 | 12.22 | 2.459E-05 | 22.51 | 46052 | 2.43 | 0.00E+00 | 3 | 0 |
| JLM77-G1b | Calibrating Standard | JLM-77 | Cpx | 1 | 2 | G2 | 1.46E-03 | 1.21 | 6.35E-02 | 0.25 | 1.41E-02 | 0.54 | 2.021E-05 | 21.48 | 51768 | 0.35 | 1.34E-03 | 217 | 216 |
| GRR2334a-G1b | Calibrating Standard | GRR2334a | Opx | 1 | 2 | G2 | 6.01E-04 | 1.98 | 6.97E-02 | 0.31 | 3.10E-04 | 4.85 | 3.79E-05 | 14.23 | 45453 | 0.24 | 4.78E-04 | 74 | 77 |
| PMR53-3c | Secondary Standard | PMR-53 | Cpx | 1 | 3 | G3 | 2.35E-03 | 10.94 | 6.12E-02 | 3.65 | 4.44E-03 | 2.52 | 4.711E-05 | 15.05 | 57136 | 2.19 | 2.24E-03 | | 389 |
| San Carlos-G1c | Blank | San Carlos | Olivine | 1 | 3 | G3 | 1.08E-04 | 4.74 | 7.23E-02 | 0.30 | 2.95E-05 | 10.82 | 2.609E-05 | 16.85 | 52569 | 0.28 | 0.00E+00 | 3 | 0 |
| JLM77-G1c | Calibrating Standard | JLM-77 | Cpx | 1 | 3 | G3 | 1.34E-03 | 1.54 | 6.22E-02 | 0.49 | 1.36E-02 | 0.86 | 3.419E-05 | 19.81 | 49845 | 0.31 | 1.23E-03 | 217 | 214 |
| GRR2334a-G1c | Calibrating Standard | GRR2334a | Opx | 1 | 3 | G3 | 5.77E-04 | 1.71 | 6.44E-02 | 0.28 | 2.59E-04 | 4.79 | 2.276E-05 | 18.36 | 49252 | 0.31 | 4.70E-04 | 74 | 82 |

Strikethrough text represents rejected analyses

Sample Mount H

| Sample ID | Analytical Role | Sample ID | Phase (Identified by probe) | Grain # | Analysis # on grain | Calibration curve | OH/Si | SE (%) | 18O/Si | SE (%) | 19F/Si | SE (%) | 35Cl/Si | SE (%) | 28Si counts | SE (%) | Background subtracted OH/Si | Standard H2O (ppm) | Calculated H2O Content |
|---|---|---|---|---|---|---|---|---|---|---|---|---|---|---|---|---|---|---|---|
| N61-H2a | Sample | N61 | Cpx | 2 | 1 | H2 | 1.83E-03 | 2.23 | 5.75E-02 | 0.35 | 2.35E-04 | 4.45 | 3.851E-05 | 8.72 | 74851 | 0.60 | 1.70E-03 |  | 286 |
| N61-H1a | Sample | N61 | Cpx | 1 | 1 | H2 | 1.91E-03 | 1.15 | 6.22E-02 | 0.80 | 2.96E-04 | 3.23 | 2.949E-05 | 11.98 | 81656 | 0.95 | 1.77E-03 |  | 299 |
| EMGN2cpx-H1a-rerun | Sample | EMGN2 | Cpx | 1 | 1 | H2 | 4.16E-03 | 0.58 | 6.16E-02 | 0.28 | 7.27E-05 | 5.97 | 2.527E-05 | 12.96 | 87564 | 0.37 | 4.02E-03 |  | 678 |
| EMGN2cpx-H1b-rerun | Sample | EMGN2 | Cpx | 1 | 2 | H2 | 3.97E-03 | 0.48 | 6.19E-02 | 0.23 | 6.88E-05 | 8.51 | 5.427E-05 | 8.93 | 86222 | 0.36 | 3.84E-03 |  | 647 |
| EMGN2cpx-H2b-rerun | Sample | EMGN2 | Cpx | 2 | 1 | H2 | 3.59E-03 | 0.64 | 6.13E-02 | 0.21 | 5.93E-05 | 6.21 | 8.592E-06 | 18.45 | 89393 | 0.31 | 3.45E-03 |  | 582 |
| EMGN21-H2a | Sample | EMGN21 | Cpx | 2 | 1 | H2 | 2.20E-03 | 0.54 | 5.90E-02 | 0.20 | 1.45E-04 | 4.87 | 1.532E-05 | 14.80 | 78024 | 0.26 | 2.07E-03 |  | 348 |
| EMGN21-H2b | Sample | EMGN21 | Cpx | 2 | 2 | H2 | 3.89E-03 | 4.55 | 5.81E-02 | 0.21 | 2.54E-04 | 3.23 | 7.27E-05 | 6.13 | 78785 | 0.41 | 3.75E-03 |  | 632 |
| N53-H1a | Sample | N53 | Cpx | 1 | 1 | H2 | 2.84E-03 | 0.51 | 6.08E-02 | 0.24 | 2.05E-04 | 2.63 | 2.874E-05 | 12.38 | 80385 | 0.36 | 2.71E-03 |  | 456 |
| N53-H2a | Sample | N53 | Cpx | 2 | 1 | H2 | 2.64E-03 | 0.73 | 6.29E-02 | 0.24 | 1.75E-04 | 3.32 | 2.428E-05 | 11.75 | 76545 | 0.23 | 2.51E-03 |  | 423 |
| Sancarlos-H1c | Blank | San Carlos | Olivine | 1 | 1 | H2 | 1.35E-04 | 3.23 | 7.37E-02 | 0.27 | 5.44E-05 | 4.60 | 4.928E-06 | 19.60 | 74470 | 0.33 | 0.00E+00 | 3 | 0 |
| GRR1650b-H1c | Calibrating Standard | GRR1650b | Opx | 1 | 1 | H2 | 7.36E-04 | 0.64 | 6.48E-02 | 0.28 | 2.37E-04 | 3.57 | 1.589E-05 | 15.19 | 76408 | 0.30 | 6.00E-04 | 119 | 101 |
| 62047-70B-H1b | Calibrating Standard | 62047-70B | Cpx | 1 | 1 | H2 | 9.17E-04 | 4.38 | 5.74E-02 | 0.21 | 1.94E-03 | 1.39 | 1.376E-05 | 14.64 | 73994 | 0.38 | 7.82E-04 | 122 | 132 |
| PMR53-H1b | Secondary Standard | PMR-53 | Cpx | 1 | 1 | H2 | 2.13E-03 | 0.82 | 5.85E-02 | 0.22 | 5.10E-03 | 0.80 | 1.724E-05 | 13.48 | 82191 | 0.39 | 1.99E-03 |  | 336 |
| CITI7210-H1b | Calibrating Standard | CIT17210 | Cpx | 1 | 1 | H2 | 3.81E-04 | 1.89 | 6.18E-02 | 0.26 | 3.90E-03 | 0.77 | 8.527E-05 | 10.13 | 68344 | 0.35 | 2.46E-04 | 29 | 41 |
| PMR53-H1c | Secondary Standard | PMR-53 | Cpx | 1 | 2 | H3 | 2.07E-03 | 0.51 | 5.90E-02 | 0.25 | 5.04E-03 | 0.56 | 5.574E-05 | 7.17 | 87406 | 0.33 | 1.92E-03 |  | 338 |
| GRR1650b-H1d | Calibrating Standard | GRR1650b | Opx | 1 | 2 | H3 | 7.57E-04 | 1.32 | 6.36E-02 | 0.20 | 2.62E-04 | 3.73 | 5.418E-05 | 9.30 | 83331 | 0.27 | 6.00E-04 | 119 | 106 |
| SanCarlos-H1d | Blank | San Carlos | Olivine | 1 | 2 | H3 | 1.56E-04 | 2.49 | 7.51E-02 | 0.20 | 6.01E-05 | 7.50 | 3.082E-05 | 12.02 | 66615 | 0.42 | 0.00E+00 | 3 | 0 |
| 62047-70B-H1c | Calibrating Standard | 62047-70B | Cpx | 1 | 2 | H3 | 8.97E-04 | 0.96 | 5.90E-02 | 0.21 | 2.01E-03 | 1.22 | 2.745E-05 | 10.78 | 71539 | 0.49 | 7.40E-04 | 122 | 131 |
| CITI7210-H1c | Calibrating Standard | CIT17210 | Cpx | 1 | 2 | H3 | 3.61E-04 | 1.73 | 6.11E-02 | 0.27 | 3.83E-03 | 0.80 | 5.711E-05 | 7.32 | 70276 | 0.36 | 2.05E-04 | 29 | 36 |

Sample Mount I

| Sample ID | Analytical Role | Sample ID | Phase (Identified by probe) | Grain # | Analysis # on grain | Calibration curve | OH/Si | SE (%) | 18O/Si | SE (%) | 19F/Si | SE (%) | 35Cl/Si | SE (%) | 28Si counts | SE (%) | Background subtracted OH/Si | Standard H2O (ppm) | Calculated H2O Content |
|---|---|---|---|---|---|---|---|---|---|---|---|---|---|---|---|---|---|---|---|
| PMR53-I1a | Secondary Standard | PMR-53 | Cpx | 1 | 1 | I1 | 2.53E-03 | 0.87 | 5.81E-02 | 0.28 | 5.26E-03 | 0.56 | 3.562E-05 | 11.43 | 130629 | 0.62 | 2.42E-03 |  | 305 |
| GRR1017-I1a | Blank | GRR1017 | Olivine | 1 | 1 | I1 | 1.12E-04 | 3.04 | 8.13E-02 | 0.20 | 2.81E-05 | 9.68 | 5.597E-05 | 9.97 | 75683 | 0.49 | 0.00E+00 | 0 | 0 |
| Sancarlos-I1a | Blank | San Carlos | Olivine | 1 | 1 | I1 | 1.15E-04 | 2.37 | 7.29E-02 | 0.18 | 4.56E-05 | 5.16 | 1.056E-05 | 17.47 | 102742 | 0.35 | 2.50E-06 | 3 | 0 |
| GRR2334a-I1a | Calibrating Standard | GRR2334a | Opx | 1 | 1 | I1 | 6.99E-04 | 1.07 | 6.28E-02 | 0.19 | 3.10E-04 | 2.19 | 1.22E-05 | 17.47 | 111979 | 0.33 | 5.87E-04 | 74 | 74 |
| CITI7210-I1a | Calibrating Standard | CIT17210 | Cpx | 1 | 1 | I1 | 3.42E-04 | 2.03 | 5.84E-02 | 0.13 | 3.71E-03 | 0.66 | 1.269E-05 | 14.12 | 112007 | 0.42 | 2.30E-04 | 29 | 29 |
| PMR53-I1b | Secondary Standard | PMR-53 | Cpx | 1 | 2 | I1 | 2.32E-03 | 0.60 | 5.64E-02 | 0.21 | 5.19E-03 | 0.52 | 1.514E-05 | 12.60 | 120386 | 0.35 | 2.21E-03 |  | 279 |
| N106opx-I2a | Sample | N106 | Opx | 2 | 1 | I1 | 2.62E-03 | 0.82 | 6.11E-02 | 0.17 | 2.33E-05 | 9.12 | 3.674E-05 | 8.23 | 109445 | 0.36 | 2.50E-03 |  | 316 |
| N106opx-I2b | Sample | N106 | Opx | 2 | 2 | I1 | 4.64E-03 | 2.05 | 6.40E-02 | 0.21 | 1.92E-05 | 8.00 | 5.414E-05 | 11.43 | 110771 | 0.29 | 4.53E-03 |  | 571 |
| N106opx-I1a | Sample | N106 | Opx | 1 | 1 | I1 | 3.89E-03 | 0.54 | 6.11E-02 | 0.23 | 3.30E-05 | 7.86 | 0.0002747 | 3.55 | 112041 | 0.52 | 3.78E-03 |  | 476 |
| EMGN29cpx-I1a-moresmears | Sample | EMGN29 | Cpx | 1 | 1 | I1 | 1.20E-02 | 0.97 | 5.80E-02 | 0.22 | 2.15E-05 | 10.21 | 5.641E-05 | 5.43 | 114734 | 0.40 | 1.19E-02 |  | 1503 |
| EMGN29cpx-I2a-moresmears | Sample | EMGN29 | Cpx | 2 | 1 | I1 | 1.21E-02 | 0.31 | 5.74E-02 | 0.28 | 1.71E-05 | 12.69 | 0.0005618 | 1.95 | 107793 | 0.46 | 1.19E-02 |  | 1506 |
| EMGN26-I2a | Sample | EMGN26 | Cpx | 2 | 1 | I2 | 4.02E-04 | 1.64 | 5.60E-02 | 0.30 | 1.88E-05 | 8.51 | 6.512E-06 | 17.09 | 114437 | 0.50 | 3.24E-04 |  | 40 |
| EMGN26-I1a | Sample | EMGN26 | Opx | 1 | 1 | I2 | 5.21E-04 | 2.43 | 6.12E-02 | 0.25 | 1.94E-04 | 5.93 | 1.484E-05 | 14.77 | 106582 | 0.42 | 4.44E-04 |  | 55 |
| N61-I1a | Sample | N61 | Cpx | 1 | 1 | I2 | 2.35E-03 | 0.48 | 5.60E-02 | 0.22 | 3.07E-04 | 3.39 | 3.318E-05 | 6.57 | 108156 | 0.63 | 2.27E-03 |  | 282 |
| N61-I2a | Sample | N61 | Cpx | 2 | 1 | I2 | 2.24E-03 | 0.76 | 5.66E-02 | 0.18 | 2.97E-04 | 2.50 | 0.0001573 | 6.90 | 106650 | 0.46 | 2.16E-03 |  | 269 |
| N53-I2a | Sample | N53 | Cpx | 2 | 1 | I2 | 2.11E-03 | 0.64 | 6.16E-02 | 0.27 | 3.03E-04 | 1.93 | 4.237E-05 | 7.91 | 95391 | 0.55 | 2.04E-03 |  | 253 |
| N53-I1a | Sample | N53 | Cpx | 1 | 1 | I2 | 2.87E-03 | 0.59 | 5.92E-02 | 0.26 | 2.76E-04 | 2.31 | 7.454E-06 | 13.03 | 89452 | 0.66 | 2.79E-03 |  | 348 |
| GRR1017-I1b | Blank | GRR1017 | Olivine | 1 | 2 | I2 | 7.76E-05 | 2.71 | 7.87E-02 | 0.29 | 2.49E-05 | 9.24 | 5.034E-06 | 24.88 | 74963 | 0.33 | 0.00E+00 | 0 | 0 |
| Sancarlos-I1b | Blank | San Carlos | Olivine | 1 | 2 | I2 | 9.23E-05 | 2.43 | 6.81E-02 | 0.11 | 4.36E-05 | 6.84 | 6.382E-06 | 18.38 | 99715 | 0.38 | 1.47E-05 | 3 | 2 |
| GRR2334a-I1b | Calibrating Standard | GRR2334a | Opx | 1 | 2 | I2 | 6.62E-04 | 1.14 | 5.95E-02 | 0.20 | 2.92E-04 | 2.39 | 8.655E-05 | 7.60 | 105462 | 0.54 | 5.84E-04 | 74 | 73 |
| CITI7210-I1b | Calibrating Standard | CIT17210 | Cpx | 1 | 2 | I2 | 3.36E-04 | 1.40 | 5.58E-02 | 0.22 | 3.84E-03 | 0.55 | 8.592E-05 | 7.26 | 102882 | 0.53 | 2.58E-04 | 29 | 32 |
| PMR53-I1c | Secondary Standard | PMR-53 | Cpx | 1 | 3 | I2 | 2.15E-03 | 0.39 | 5.51E-02 | 0.27 | 5.11E-03 | 0.74 | 7.506E-05 | 8.16 | 121925 | 0.43 | 2.07E-03 |  | 257 |
| GRR1017-I1c | Blank | GRR1017 | Olivine | 1 | 3 | I3 | 1.16E-04 | 4.05 | 7.74E-02 | 0.21 | 3.42E-05 | 7.01 | 0.0001454 | 11.08 | 71714 | 0.52 | 4.03E-05 |  | 5 |
| SanCarlos-I1c | Blank | San Carlos | Olivine | 1 | 3 | I3 | 1.56E-04 | 3.74 | 7.12E-02 | 0.19 | 5.87E-05 | 5.22 | 0.0001212 | 10.11 | 95927 | 0.52 | 8.02E-05 |  | 10 |
| GRR1017-I1d | Blank | GRR1017 | Olivine | 1 | 4 | I3 | 7.61E-05 | 1.84 | 7.86E-02 | 0.21 | 2.46E-05 | 11.58 | 5.592E-06 | 19.60 | 72624 | 0.32 | 0.00E+00 | 0 | 0 |
| GRR2334a-I1c | Calibrating Standard | GRR2334a | Opx | 1 | 3 | I3 | 6.47E-04 | 1.40 | 6.02E-02 | 0.17 | 3.01E-04 | 2.30 | 6.684E-05 | 6.46 | 107567 | 0.57 | 5.71E-04 | 74 | 72 |
| CITI7210-I1c | Calibrating Standard | CIT17210 | Cpx | 1 | 3 | I3 | 3.39E-04 | 1.97 | 5.67E-02 | 0.26 | 3.85E-03 | 0.61 | 0.0001082 | 8.03 | 104264 | 0.60 | 2.63E-04 | 29 | 33 |
| PMR53-I1d | Secondary Standard | PMR-53 | Cpx | 1 | 4 | I3 | 2.08E-03 | 0.87 | 5.40E-02 | 0.43 | 5.01E-03 | 0.84 | 9.776E-05 | 16.07 | 124914 | 1.21 | 2.01E-03 |  | 253 |
| Sancarlos-I1d | Blank | San Carlos | Olivine | 1 | 4 | I3 | 9.14E-05 | 2.63 | 6.73E-02 | 0.18 | 4.06E-05 | 9.78 | 4.124E-06 | 28.49 | 99304 | 0.49 | 1.53E-05 | 3 | 2 |

# References

Aines, R.D., and Rossman, G.R., 1984, Water content of mantle garnets: Geology, , no. December, p. 720–723.

Alibert, C., 1994, Peridotite xenoliths from western Grand Canyon and The Thumb: A probe into the subcontinental mantle: Journal of Geological Research, v. 99, no. 11, p. 21605–21620.

Alt, J.C., and Bach, W., 2006, Oxygen isotope composition of a section of lower oceanic crust, ODP Hole 735B: Geochemistry, Geophysics, Geosystems, v. 7, no. 12.

Anderson, J.L., and Cullers, R.L., 1999, Paleo- and Mesoproterozoic granite plutonism of Colorado and Wyoming: Rocky Mountain Geology, v. 34, no. 2, p. 149–164.

Anderson, J.L., and Morrison, J., 2005, Ilmenite, magnetite, and peraluminous Mesoproterozoic anorogenic granites of Laurentia and Baltica: Lithos, v. 80, p. 45–60.

Aubaud, C., Withers, A.C., Hirschmann, M.M., Guan, Y., Leshin, L. a., Mackwell, S.J., and Bell, D.R., 2007, Intercalibration of FTIR and SIMS for hydrogen measurements in glasses and nominally anhydrous minerals: American Mineralogist , v. 92, no. 5–6, p. 811–828.

Bai, Q., and Kohlstedt, D.L., 1992, Substantial hydrogen solubility in olivine and implications for water storage in the mantle: Nature, v. 357, no. 6380, p. 672–674.

Behr, W.M., and Smith, D., 2016, Deformation in the mantle wedge associated with Laramide flat-slab subduction: Geochemistry Geophysics Geosystems, v. 17, p. 2825–2834.

Bell, D.R., Ihinger, P.D., and Rossman, G.R., 1995, Quantitative analysis of trace OH in garnet and pyroxenes: American Mineralogist, v. 80, p. 465–474.

Bennett, V., and DePaolo, D., 1987, Proterozoic crustal history of the western United States as determined by neodymium isotopic mapping: Geological Society of America, v. 99, p. 674–685.

Birck, J.L., Barman, M.R., and Capmas, F., 1997, Re-Os Isotopic Measurements at the Femtomole Level in Natural Samples: Geostandards Newsletter, v. 20, p. 19–27.

Bird, P., 1988, Formation of the Rocky Mountains, western United States: a continuum computer model: Science, v. 239, no. 4847, p. 1501–1507.

Boettcher, A., and O'Neil, J., 1980, Isotope, chemical, and petrographic studies of high-pressure amphiboles and micas: evidence for metasomatism in the mantle source regions of alkali basalts: American Journal of Science, v. 280, p. 594–621.

Bybee, G.M., Ashwal, L.D., Shirey, S.B., Horan, M., Mock, T., and Andersen, T.B., 2014, Pyroxene megacrysts in Proterozoic anorthosites: Implications for tectonic setting, magma source and magmatic processes at the Moho: Earth and Planetary Science Letters, v. 389, p. 74–85.

Byerly, B.L., and Lassiter, J.C., 2015, Trace element partitioning and Lu–Hf isotope systematics in spinel peridotites from the Rio Grande Rift and Colorado Plateau: Towards improved age assessment of clinopyroxene Lu/Hf–176Hf/177Hf in SCLM peridotite: Chemical Geology, v. 413, p. 146–158.

Byerly, B.L., and Lassiter, J.C., 2012, Evidence from mantle xenoliths for lithosphere removal beneath the central Rio Grande Rift: Earth and Planetary Science Letters, v. 355–356, p. 82–93.

Chakraborty, S., 1997, Rates and mechanisms of Fe-Mg interdiffusion in olivine at 980° to 1300°C: Journal of Geophysical Research, v. 102, no. B6, p. 12317–12331.

Chatterjee, R., and Lassiter, J.C., 2015, High precision Os isotopic measurement using N-TIMS: Quantification of various sources of error in 186Os/188Os measurements: Chemical Geology, v. 396, p. 112–123.

Chazot, G., Lowry, D., Menzies, M., and Mattey, D., 1997, Oxygen isotopic composition of hydrous and anhydrous mantle peridotites: Geochimica et Cosmochimica Acta, v. 61, no. 1, p. 161–169.

Cherniak, D.J., and Dimanov, A., 2010, Diffusion in Pyroxene, Mica and Amphibole: Reviews in Mineralogy and Geochemistry, v. 72, no. 1, p. 641–690.

Condie, K.C., Latysh, N., Van Schmus, W.R., Kozuch, M., and Selverstone, J., 1999, Geochemistry, Nd and Sr isotopes, and U/Pb Zircon ages of Granitoid and Metasedimentary Xenoliths from the Navajo Volcanic Field, Four Corners area, Southwestern United States: Chemical Geology, v. 156, p. 95–133.

Condie, K.C., 1992, Proterozoic Terranes and Continental Accretion in Southwestern North America: Developments in Precambrian Geology, v. 10, no. C, p. 447–480.

Connelly, J.N., Ulfbeck, D.G., Thrane, K., Bizzarro, M., and Housh, T., 2006, A method for purifying Lu and Hf for analyses by MC-ICP-MS using TODGA resin: Chemical Geology, v. 233, no. 1–2, p. 126–136.

Corrigan, D., and Hanmer, S., 1997, Anorthosites and related granitoids in the Grenville orogen : A product of convective thinning of the lithosphere ? Geology, v. 25, no. 1, p. 61–64.

Crowley, J.L., Schmitz, M.D., Bowring, S.A., Williams, M.L., and Karlstrom, K.E., 2006, U-Pb and Hf isotopic analysis of zircon in lower crustal xenoliths from the Navajo volcanic field: 1.4 Ga mafic magmatism and metamorphism beneath the Colorado Plateau: Contributions to Mineralogy and Petrology, v. 151, no. 3, p. 313–330.

Daniel, C.G., Pfeifer, L.S., Jones, J. V., and McFarlane, C.M., 2013, Detrital zircon evidence for non-laurentian provenance, mesoproterozoic (ca. 1490-1450 ma) deposition and orogenesis in a reconstructed orogenic belt, northern new mexico, USA: Defining the picuris orogeny: Bulletin of the Geological Society of America, v. 125, no. 9–10, p. 1423–1441.

Demouchy, S., and Bolfan-Casanova, N., 2016, Distribution and transport of hydrogen in the lithospheric mantle: A review: Lithos, v. 240–243, p. 402–425.

Demouchy, S., Ishikawa, A., Tommasi, A., Alard, O., and Keshav, S., 2015, Characterization of hydration in the mantle lithosphere : Peridotite xenoliths from the Ontong Java Plateau as an example: Lithos, v. 212–215, p. 189–201.

Demouchy, S., Jacobsen, S.D., Gaillard, F., and Stern, C.R., 2006, Rapid magma ascent recorded by water diffusion profiles in mantle olivine: Geology, v. 34, no. 6, p. 429.

Demouchy, S., and Mackwell, S.J., 2006, Mechanisms of hydrogen incorporation and diffusion in iron-bearing olivine: Physics and Chemistry of Minerals, v. 33, no. 5, p. 347–355.

Denis, C.M.M., Alard, O., Demouchy, S., Central, M., Denis, C.M.M., Alard, O., and Demouchy, S., 2015, Water content and hydrogen behaviour during metasomatism in the uppermost mantle beneath Ray Pic volcano (Massif Central, France): Lithos, v. 236–237, p. 256–274.

Dixon, J.E., Dixon, T.., Bell, D.., and Malservisi, R., 2004, Lateral variation in upper mantle viscosity: role of water: Earth and Planetary Science Letters, v. 222, no. 2, p. 451–467.

Doucet, L.S., Peslier, A.H., Ionov, D. a., Brandon, A.D., Golovin, A. V., Goncharov, A.G., and Ashchepkov, I. V., 2014, High water contents in the Siberian cratonic mantle linked to metasomatism: An FTIR study of Udachnaya peridotite xenoliths: Geochimica et Cosmochimica Acta, v. 137, p. 159–187.

Eiler, J.M., Crawford, A., Elliott, T.I.M., Farley, K.A., Valley, J.W., and Stolper, E.M., 2000, Oxygen Isotope Geochemistry of Oceanic-Arc Lavas: Journal of Petrology, v. 41, no. 2, p. 229–256.

Eiler, J.M., Carr, M.J., Reagan, M., and Stolper, E., 2005, Oxygen isotope constraints on the sources of Central American arc lavas: Geochemistry, Geophysics, Geosystems, v. 6, no. 7.

Elliott, T., Plank, T., Zindler, A., White, W., and Bourdon, B., 1997, Element transport from slab to volcanic front at the Mariana arc: Journal of Geophysical Research, v. 102, no. B7, p. 14991–15019.

English, J.M., Johnston, S.T., and Wang, K., 2003, Thermal modelling of the Laramide orogeny: Testing the flat-slab subduction hypothesis: Earth and Planetary Science Letters, v. 214, no. 3–4, p. 619–632.

Evans, B.W., 2010, Lizardite versus antigorite serpentinite: Magnetite, hydrogen, and life(?): Geology, v. 38, no. 10, p. 879–882.

Evans, D.A.D., and Mitchell, R.N., 2011, Assembly and breakup of the core of Paleoproterozoic-Mesoproterozoic supercontinent Nuna: Geology, v. 39, no. 5, p. 443–446.

Frost, D.J., 2006, The Stability of Hydrous Mantle Phases: Reviews in Mineralogy and Geochemistry, v. 62, no. 1, p. 243–271.

Gavrilenko, P., 2008, Water solubility in diopside: Univeristy of Bayreuth, 139 p.

Goodge, J.W., and Vervoort, J.D., 2006, Origin of Mesoproterozoic A-type granites in Laurentia: Hf isotope evidence: Earth and Planetary Science Letters, v. 243, no. 3–4, p. 711–731.

Grant, K., Ingrin, J., Lorand, J.P., and Dumas, P., 2007, Water partitioning between mantle minerals from peridotite xenoliths: Contributions to Mineralogy and Petrology, v. 154, no. 1, p. 15–34.

Gregory, R.T., and Taylor, H.P., 1981, An oxygen isotope profile in a section of Cretaceous oceanic crust, Samail Ophiolite, Oman: Evidence for δ18O buffering of the oceans by deep (>5 km) seawater-hydrothermal circulation at mid-ocean ridges: Journal of Geophysical Research: Solid Earth, v. 86, no. B4, p. 2737–2755.

Hacker, B.R., 2008, H2O subduction beyond arcs: Geochemistry, Geophysics, Geosystems, v. 9, no. 3, p. 1–24.

Handler, M.R., Bennett, V.C., and Esat, T.M., 1997, The persistence of off-cratonic lithospheric mantle: Os isotopic systematics of variably metasomatised southeast Australian xenoliths: Earth and Planetary Science Letters, v. 151, no. 1–2, p. 61–75.

Hao, Y., Xia, Q., Li, Q., Chen, H., and Feng, M., 2014, Partial melting control of water contents in the Cenozoic lithospheric mantle of the Cathaysia block of South China: Chemical Geology, v. 380, p. 7–19.

Hauri, E.H., Gaetani, G.A., and Green, T.H., 2006, Partitioning of water during melting of the Earth's upper mantle at H2O-undersaturated conditions: Earth and Planetary Science Letters, v. 248, no. 3–4, p. 715–734.

Hickson, C.J., and Juras, S.J., 1986, Sample contamination by grinding.: Canadian Mineralogist, v. 24, no. 3, p. 585–589.

Hirth, G., and Kohlstedt, D., 1996, Water in the oceanic upper mantle: Implications for rheology, melt extraction and the evolution of the lithosphere: Earth and Planetary Science Letters, v. 144, p. 93–108.

Humphreys, E., 1995, Post-Laramide removal of the Farallon slab, western United States: Geology, v. 23, no. 11, p. 987–990.

Humphreys, E., 2009, Relation of flat subduction to magmatism and deformation in the western United States, *in* Geological Society of America Memior, p. 85–98.

Humphreys, E., Hessler, E., Dueker, K., Farmer, G.L., Erslev, E., and Atwater, T., 2003, How Laramide-Age Hydration of North American Lithosphere by the Farallon Slab Controlled Subsequent Activity in the Western United States: International Geology Review, v. 45, no. 7, p. 575–595.

Jarosewich, E., Gooley, R., and Husler, J., 1987, Chromium Augite- a new microprobe reference sample: Geostandards Newsletter, v. 11, no. 2, p. 197–198.

Johnson, D.M., Hooper, P.R., and Conrey, R.M., 1999, XRF Analysis of Rocks and Minerals for Major and Trace Elements on a Single Low Dilution Li-tetraborate Fused Bead: Advances in X-Ray Analysis, v. 41, p. 843–867.

Jones, J. V., Siddoway, C.S., and Connelly, J.N., 2010, Characteristics and implications of ca. 1.4 Ga deformation across a Proterozoic mid-crustal section, Wet Mountains, Colorado, USA: Lithosphere, v. 2, no. 2, p. 119–135.

Karlstrom, K.E., and Bowring, S.A., 1988, Early Proterozoic Assembly of Tectonostratigraphic Terranes in Southwestern North America: Geology, v. 96, no. 5, p. 561–576.

Kempton, P.D., Harmon, R.S., Stosch, H.G., Hoefs, J., and Hawkesworth, C.J., 1988, Open-system O-isotope behaviour and trace element enrichment in the sub-Eifel mantle: Earth and Planetary Science Letters, v. 89, p. 273–287.

Koga, K., Hauri, E., Hirschmann, M., and Bell, D., 2003, Hydrogen concentration analyses using SIMS and FTIR: Comparison and calibration for nominally anhydrous minerals: Geochemistry, Geophysics, Geosystems, v. 4, no. 2, p. n/a-n/a.

Kovacs, I., Demeny, A., Czuppon, G., Lecuyer, C., Fourel, F., Xia, Q.K., Liu, J., Pinter, Z., Kiraly, E., Torok, K., Szabo, A., Deloule, E., Falus, G., Fancsik, T., et al., 2016, Water concentrations and hydrogen isotope compositions of alkaline basalt-hosted clinopyroxene megacrysts and amphibole clinopyroxenites: the role of structural hydroxyl groups and molecular water: Contributions to Mineralogy and Petrology, v. 171, no. 5, p. 1–18.

Kuroda, Y., Suzuoki, T., Matsuo, S., and Aoki, K.-I., 1975, D/H ratios of the coexisting phlogopite and richterite from mica nodules and a peridotite in South African kimberlites: Contributions to Mineralogy and Petrology, v. 52, no. 4, p. 315–318.

Kyser, T., and O’Neil, J., 1984, Hydrogen isotope systematics of submarine basalts: Geochimica et Cosmochimica Acta, v. 48, p. 2123–2133.

Lamb, W., and Popp, R.K., 2009, Amphibole equilibria in mantle rocks: Determining values of mantle aH2O and implications for mantle H2O contents: American Mineralogist, v. 94, p. 41–52.

Lee, C.T., Yin, Q., Rudnick, R.L., and Jacobsen, S.B., 2001, Preservation of ancient and fertile lithospheric mantle beneath the southwestern United States.: Nature, v. 411, no. 6833, p. 69–73.

Lee, C.-T. a., Luffi, P., and Chin, E.J., 2011, Building and Destroying Continental Mantle: Annual Review of Earth and Planetary Sciences, v. 39, no. 1, p. 59–90.

Lee, C.A., 2005, Trace Element Evidence for Hydrous Metasomatism at the Base of the North American Lithosphere and Possible Association with Laramide Low-Angle Subduction: The Journal of Geology, v. 113, no. Bird 1988, p. 673–685.

Leeman, W.P., Carr, M.J., and Morris, J.D., 1994, Boron geochemistry of the Central American Volcanic Arc : Constraints on the genesis of subduction-related magmas: Geochimica et Cosmochimica Acta, v. 58, p. 149–168.

Levander, A., Schmandt, B., Miller, M., Liu, K., Karlstrom, K.E., Crow, R.S., Lee, C.-T.A., and Humphreys, E.D., 2011, Continuing Colorado plateau uplift by delamination-style convective lithospheric downwelling: Nature, v. 472, no. 7344, p. 461–5.

Li, Z.-X.A., Lee, C.-T. a., Peslier, A.H., Lenardic, A., and Mackwell, S.J., 2008, Water contents in mantle xenoliths from the Colorado Plateau and vicinity: Implications for the mantle rheology and hydration-induced thinning of continental lithosphere: Journal of Geophysical Research, v. 113, no. B9, p. B09210.

Lowry, D., Mattey, D.P., and Harris, J.W., 1999, Oxygen isotope composition of syngenetic inclusions in diamond from the Finsch Mine, RSA: Geochimica et Cosmochimica Acta, v. 63, no. 11–12, p. 1825–1836.

Mako, C. a., Williams, M.L., Karlstrom, K.E., Doe, M.F., Powicki, D., Holland, M.E., Gehrels, G., and Pecha, M., 2015, Polyphase Proterozoic deformation in the Four Peaks area, central Arizona, and relevance for the Mazatzal orogeny: Geosphere, v. 11, no. 6, p. 1975–1995.

Marshall, E.W., Barnes, J.D., and Lassiter, J.C., 2017, The role of serpentinite-derived fluids in metasomatism of the Colorado Plateau ( USA ) lithospheric mantle: Geology, v. 45, no. 12, p. 1–4.

Marshall, E.W., Lassiter, J.C., Barnes, J.D., Luguet, A., and Lissner, M., 2017, Mantle melt production during the 1.4 Ga Laurentian magmatic event: Isotopic constraints from Colorado Plateau mantle xenoliths: Geology, v. 45, no. 6, p. 519–522.

Mattey, D., Lowry, D., and Macpherson, C., 1994, Oxygen isotope composition of mantle peridotite: Earth and Planetary Science Letters, v. 128, no. 3–4, p. 231–241.

McDonough, W., and Sun, S., 1995, The composition of the Earth: Chemical geology, , no. 120, p. 223–253.

McGetchin, T.R., and Silver, L.T., 1970, Compositional relations in minerals from kimberlite and related rocks in the Moses Rock dike, San Juan County, Utah: American Mineralogist, v. 55, no. 1618, p. 1738–1771.

McGetchin, T.R., and Silver, L.T., 1972, A crustal-upper-mantle model for the Colorado Plateau based on observations of crystalline rock fragments in the Moses Rock Dike: Journal of Geophysical Research, v. 77, no. 35, p. 7022–7037.

McKenzie, D., and O'Nions, R.K., 1983, Mantle reservoirs and ocean island basalts: Nature, v. 301, p. 229–231.

Michael, P., 1995, Regionally distinctive sources of depleted MORB: Evidence from trace elements and H2O: Earth and Planetary Science Letters, v. 131, no. 3–4, p. 301–320.

Mosenfelder, J.L., and Rossman, G.R., 2013, Analysis of hydrogen and fluorine in pyroxenes: II. Orthopyroxene: American Mineralogist, v. 98, no. 5–6, p. 1026–1041.

Mosenfelder, J.L., and Rossman, G.R., 2013, Analysis of hydrogen and fluorine in pyroxenes: II. Clinopyroxene: American Mineralogist, v. 98, no. 5–6, p. 1042–1054.

Nyman, M.W., Karlstrom, K.E., Kirby, E., and Graubard, C.M., 1994, Mesoproterozoic contractional orogeny in western North America : Evidence from ca. 1.4 Ga plutons: Geology, v. 22, p. 901–904.

Nyman, M.W., and Karlstrom, K.E., 1997, Pluton emplacement processes and tectonic setting of the 1.42 Ga Signal batholith, SW USA: important role of crustal anisotropy during regional shortening: Precambrian Research, v. 82, p. 237–263.

O'Leary, J.A., Gaetani, G.A., and Hauri, E.H., 2010, The effect of tetrahedral Al 3 + on the partitioning of water between clinopyroxene and silicate melt: Earth and Planetary Science Letters, v. 297, p. 111–120.

Perkins, G.B., Sharp, Z.D., and Selverstone, J., 2006, Oxygen isotope evidence for subduction and rift-related mantle metasomatism beneath the Colorado Plateau–Rio Grande rift transition: Contributions to Mineralogy and Petrology, v. 151, no. 6, p. 633–650.

Peslier, a, and Luhr, J., 2006, Hydrogen loss from olivines in mantle xenoliths from Simcoe (USA) and Mexico: Mafic alkalic magma ascent rates and water budget of the sub-continental lithosphere: Earth and Planetary Science Letters, v. 242, no. 3–4, p. 302–319.

Peslier, A.H., Woodland, A.B., Bell, D.R., Lazarov, M., and Lapen, T.J., 2012, Metasomatic control of water contents in the Kaapvaal cratonic mantle: Geochimica et Cosmochimica Acta, v. 97, p. 213–246.

Peslier, A.H., 2010, A review of water contents of nominally anhydrous natural minerals in the mantles of Earth, Mars and the Moon: Journal of Volcanology and Geothermal Research, v. 197, no. 1–4, p. 239–258.

Peslier, A.H., Woodland, A.B., and Wolff, J. a., 2008, Fast kimberlite ascent rates estimated from hydrogen diffusion profiles in xenolithic mantle olivines from southern Africa: Geochimica et Cosmochimica Acta, v. 72, no. 11, p. 2711–2722.

Raczek, I., Jochum, K.P., and Hofmann, A.W., 2001, Neodymium and Strontium Isotope Data for USGS Reference GSP-1 , GSP-2 and Eight MPI-DING Reference Glasses: Geostandards Newsletterthe Journal of Geostandards and Geoanalysis, v. 27, no. 2, p. 173–179.

Reisberg, L., and Lorand, J.-P., 1995, Longevity of sub-continental mantle lithosphere from osmium isotope systematics in orogenic peridotite massifs: Nature, v. 376, no. 6536, p. 159–162.

Riter, J.A., 1999, Geochemical and Tectonic Evolution of the Colorado Plateau Mantle Lithosphere: Evidence from Grand Canyon Mantle Xenoliths: University of Texas at Austin, 356 p.

Roden, M., 1981, Origin of coexisting minette and ultramafic breccia, Navajo volcanic field: Contributions to Mineralogy and Petrology, p. 195–206.

Roden, M., and Shimizu, N., 1993, Ion microprobe analyses bearing on the composition of the upper mantle beneath the Basin and Range and Colorado Plateau provinces: Journal of Geological Research, v. 98, no. 93, p. 14091–14108.

Roden, M., Smith, D., and Murthy, V., 1990, Chemical constraints on lithosphere composition and evolution beneath the Colorado Plateau: Journal of Geophysical Research, v. 95, no. 89, p. 2811–2831.

Rogers, J.J.W., and Santosh, M., 2002, Configuration of Columbia, a Mesoproterozoic Supercontinent: Gondwana Research, v. 5, no. 1, p. 5–22.

Rossman, G.R., 1996, Studies of OH in nominally anhydrous minerals: Physics and Chemistry of Minerals, v. 23, no. 4–5, p. 299–304.

Rudnick, R.L., and Walker, R.J., 2009, Interpreting ages from Re-Os isotopes in peridotites: Lithos, v. 112, p. 1083–1095.

Saccocia, P.J., Seewald, J.S., and Shanks, W.C., 2009, Oxygen and hydrogen isotope fractionation in serpentine-water and talc-water systems from 250 to 450C, 50 MPa: Geochimica et Cosmochimica Acta, v. 73, no. 22, p. 6789–6804.

Scher, H.D., and Delaney, M.L., 2010, Breaking the glass ceiling for high resolution Nd isotope records in early Cenozoic paleoceanography: Chemical Geology, v. 269, no. 3–4, p. 329–338.

Schmidt, M.W., and Poli, S., 1998, Experimentally based water budgets for dehydrating slabs and consequences for arc magma generation: Earth and Planetary Science Letters, v. 163, no. 1–4, p. 361–379.

Selverstone, J., Pun, A., and Condie, K.C., 1999, Xenolithic evidence for Proterozoic crustal evolution beneath the Colorado Plateau: Geological Society of America Bulletin, v. 111, no. 4, p. 590–606.

Sharp, Z.D., Atudorei, V., and Durakiewicz, T., 2001, A rapid method for determination of hydrogen and oxygen isotope ratios from water and hydrous minerals: Chemical Geology, v. 178, p. 197–210.

Sharp, Z., 1990, A laser-based microanalytical method for the in situ determination of oxygen isotope ratios of silicates and oxides: Geochimica et Cosmochimica Acta, v. 54, p. 1353–1357.

Shaw, A.M., Hauri, E.H., Fischer, T.P., Hilton, D.R., and Kelley, K.A., 2008, Hydrogen isotopes in Mariana arc melt inclusions: Implications for subduction dehydration and the deep-Earth water cycle: Earth and Planetary Science Letters, v. 275, no. 1–2, p. 138–145.

Silver, L.T., and McGetchin, T.R., 1994, Observations on the nature of the Pre- cambrian crust under the southern Colorado Plateau: Geological Society of America Abstracts with Programs, v. 26, no. 6, p. 63.

Skogby, H., Bell, D.R., and Rossman, G.R., 1990, Hydroxide in pyroxene; variations in the natural environment: American Mineralogist, v. 75, no. 7–8, p. 764–774.

Smith, D., 1979, Hydrous minerals and carbonates in peridotite inclusions from the green knobs and bull park kimberlitic diatremes on the Colorado Plateau: The Mantle Sample: Inclusion in Kimberlites and Other Volcanics, v. 16, p. 345–356.

Smith, D., and Levy, S., 1976, Petrology of the Green Knobs diatreme and implications for the upper mantle below the Colorado Plateau: Earth and Planetary Science Letters, v. 29, p. 107–125.

Smith, D., Riter, J.A., and Mertzman, S., 1999, Water–rock interactions, orthopyroxene growth, and Si-enrichment in the mantle: evidence in xenoliths from the Colorado Plateau, southwestern United States: Earth and Planetary Science Letters, v. 167, p. 347–356.

Smith, D., 2010, Antigorite Peridotite, Metaserpentinite, and other Inclusions within Diatremes on the Colorado Plateau, SW USA: Implications for the Mantle Wedge during Low-angle Subduction: Journal of Petrology, v. 51, no. 6, p. 1355–1379.

Smith, D., 1977, The Origin and Interpretation of Spinel-Pyroxene Clusters in Peridotite: The Journal of Geology, v. 85, no. 4, p. 476–482.

Smith, D., 2013, Olivine thermometry and source constraints for mantle fragments in the Navajo Volcanic Field, Colorado Plateau, southwest United States: Implications for the mantle wedge: Geochemistry, Geophysics, Geosystems, v. 14, no. 3, p. 693–711.

Smith, D., and Griffin, W.L., 2005, Garnetite Xenoliths and Mantle-Water Interactions Below the Colorado Plateau, Southwestern United States: Journal of Petrology, v. 46, no. 9, p. 1901–1924.

Smith, D., and Riter, J., 1997, Genesis and evolution of low-Al orthopyroxene in spinel peridotite xenoliths, Grand Canyon field, Arizona, USA: Contributions to Mineralogy and Petrology, v. 127, p. 391–404.

Strnad, L., Mihaljevic, M., and Sebek, O., 2005, Laser Ablation and Solution ICP-MS Determination of Rare Earth Elements in USGS BIR-1G , BHVO-2G and BCR-2G Glass Reference Materials: Geostandards and Geoanalytical Research, v. 29, no. 3, p. 303–314.

Sundvall, R., and Stalder, R., 2011, Water in upper mantle pyroxene megacrysts and xenocrysts: A survey study: American Mineralogist, v. 96, no. 8–9, p. 1215–1227.

Tenner, T.J., Hirschmann, M.M., Withers, A.C., and Hervig, R.L., 2009, Hydrogen partitioning between nominally anhydrous upper mantle minerals and melt between 3 and 5 GPa and applications to hydrous peridotite partial melting: Chemical Geology, v. 262, no. 1, p. 42–56.

Valley, J.W., Kitchen, N., Kohn, M.J., Niendorf, C.R., and Spicuzza, M.J., 1995, UWG-2, a garnet standard for oxygen isotope ratios: Strategies for high precision and accuracy with laser heating: Geochimica et Cosmochimica Acta, v. 59, no. 24, p. 5223–5231.

Warren, J.M., 2016, Global variations in abyssal peridotite compositions: Lithos, v. 248–251, p. 193–219.

Warren, J., and Hauri, E., 2014, Pyroxenes as tracers of mantle water variations: Journal of Geophysical Research: Solid …, , no. August, p. 1851–1881.

Wenner, D.B., and Taylor, H.P., 1973, Oxygen and hydrogen isotope studies of the serpentinization of ultramafic rocks in oceanic environments and continental ophiolite complexes: American Journal of Science, v. 273, no. 3, p. 207–239.

West, M., Ni, J., Baldridge, W.S., Wilson, D., Aster, R., and Gao, W., 2004, Crust and upper mantle shear wave structure of the southwest United States : Implications for rifting and support for high elevation: Journal of Geophysical Research, v. 109, p. 1–16.

Whalen, J.B., Currie, K.L., and Chappell, B.W., 1987, A-type granites: geochemical characteristics, discrimination and petrogenesis: Contributions to Mineralogy and Petrology, v. 95, no. 4, p. 407–419.

Whitmeyer, S.J., and Karlstrom, K.E., 2007, Tectonic model for the Proterozoic growth of North America: Geosphere, v. 3, no. 4, p. 220–259.

Workman, R.K., and Hart, S.R., 2005, Major and trace element composition of the depleted MORB mantle (DMM): Earth and Planetary Science Letters, v. 231, no. 1–2, p. 53–72.

Xia, Q.K., Hao, Y., Li, P., Deloule, E., Coltorti, M., Dallai, L., Yang, X., and Feng, M., 2010, Low water content of the Cenozoic lithospheric mantle beneath the eastern part of the North China Craton: Journal of Geophysical Research, v. 115, p. 1–22.

Yang, X., Xia, Q., Deloule, E., Dallai, L., Fan, Q., and Feng, M., 2008, Water in minerals of the continental lithospheric mantle and overlying lower crust : A comparative study of peridotite and granulite xenoliths from the North China Craton: Chemical Geology, v. 256, p. 33–45.

# Vita

Edward Wayne Marshall IV was born in Philadelphia, Pennsylvania in 1989 to Joanna M. Bassert and Edward W. Marshall III. At one year old he began attending daycare at Germantown Friends School. Seventeen years later he left GFS and enrolled at Earlham College in Richmond, Indiana to continue his Quakerly education. He received a B.A. in Geology with college and departmental honors and subsequently entered the Ph.D. program at the University of Texas at Austin.

Permanent address: edmarshall4@gmail.com

This dissertation was typed by the author.